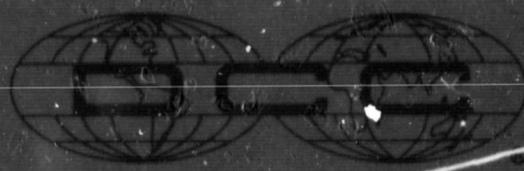


N O T I C E

THIS DOCUMENT HAS BEEN REPRODUCED FROM
MICROFICHE. ALTHOUGH IT IS RECOGNIZED THAT
CERTAIN PORTIONS ARE ILLEGIBLE, IT IS BEING RELEASED
IN THE INTEREST OF MAKING AVAILABLE AS MUCH
INFORMATION AS POSSIBLE

NASA CR-1600



g.o. moran by 10/21/84

Digital Communications Corporation

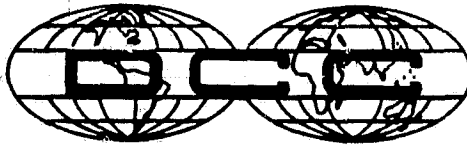
(NASA-CR-160042) FEASIBILITY STUDY OF AN
INTEGRATED OPTIC SWITCHING CENTER Final
Report (Digital Communications Corp.,
Gaithersburg, Md.) 148 p HC Av/MF A01

N81-12863

CSCL 20F G3/74

Unclassified
39955

Excellence in Telecommunications Engineering



DCC-823-279-FR-00-357

FEASIBILITY STUDY OF AN INTEGRATED
OPTIC SWITCHING CENTER
FINAL REPORT

MAY 1979

Prepared for NASA
Goddard Space Flight Center
Greenbelt, Maryland 20771

Contract # NAS5-24449

DIGITAL COMMUNICATIONS CORPORATION
19 FIRSTFIELD ROAD
GAIITHERSBURG, MARYLAND 20760

TELEPHONE: (301) 948-0850
TWX: 710-828-0541
DIGICOM GARG

TABLE OF CONTENTS

<u>Section</u>	<u>Title</u>	<u>Page</u>
1.0	STATEMENT OF PROBLEM	1-1
2.0	SUMMARY	2-1
3.0	INTEGRATED OPTICS SWITCHING CONCEPT	3-1
3.1	Electro-Optic Bragg Diffraction Switch	3-1
3.1.1	Analysis of Electro-Optic, Thin-Film, Bragg Diffraction Switch	3-10
3.1.2	Linear Electro-Optic Effect in Unaxial Crystal	3-21
4.0	INTEGRATED OPTICS SWITCHING MATRIX USING ELECTRO-OPTIC, THIN-FILM, BRAGG DIFFRACTION SWITCHES	4-1
5.0	END-FIRE COUPLING USING CYLINDRICAL MICRO-LENSES	5-1
5.1	Single Transverse Mode in Planar Optical Waveguide (Y-Direction)	5-3
5.2	Beam Shape in the X-Z Plane	5-5
5.3	Beam Transformation	5-8
5.4	Cylindrical Microlenses	5-8
5.5	Transformation in Meridian Plane Parallel to Y-Direction	5-12
5.6	Transformation in Meridian Plane Parallel to X-Z Plane	5-16
5.7	End-Fire Coupling Between Sections of the Switching Matrix on Separate Substrates	5-19
6.0	CROSS TALK REDUCTION	6-1
7.0	P-N JUNCTION LASER	7-1
7.1	Introduction	7-1
7.2	Double Heterostructure Laser	7-1
7.2.1	Structure	7-1

TABLE OF CONTENTS (Cont.)

<u>Section</u>	<u>Title</u>	<u>Page</u>
7.2.2	Operation Wavelength	7-4
7.2.3	Stable Transverse Mode Relation With Up to 10 Microns Junction Width	7-4
7.2.4	High Bit Rate PCM Modulation of DH-AlGaAs Lasers	7-11
8.0	FABRICATION OF ELECTRO-OPTIC BRAGG DIFFRACTION SWITCH	8-1
8.1	Fabrication of Active Optical Waveguides	8-3
8.1.1	Ferroelectric Crystals	8-3
8.1.2	Planar Active Optical Waveguides	8-5
8.1.2.1	Out-Diffusion	8-5
8.1.2.2	In-Diffusion	8-9
8.1.2.2.1	Ti-Diffusion Into LiNbO_3	8-9
8.1.2.2.2	Nb Diffusion Into LiTaO_3	8-12
8.2	Fabrication of Periodic Metal Electrodes	8-13
9.0	SINGLE-MODE FIBER SPLICING	9-1
10.0	DATA FLOW, ACCESS TECHNIQUE, ARCHITECTURE AND PROTOCOL	10-1
11.0	RESOURCES	11-1
12.0	CONCLUSIONS AND DEVELOPMENT PROGRAM	12-1
12.1	Conclusions	12-1
12.2	Development Program	12-2
APPENDIX A		A-1
APPENDIX B		B-1

LIST OF ILLUSTRATIONS

<u>Figure</u>	<u>Title</u>	<u>Page</u>
3-1	Integrated Optics Switching Center with 4X4 Matrix (Using Wider Switches)	3-4
3-2	Integrated Optics Switching Center with 4X4 Matrix (Using Wider Switches) In Operation	3-5
3-3	Electro-Optic Bragg Diffraction Switch in LiTiNbO_3 Waveguide	3-6
3-4	Electro-Optic Bragg Diffraction Switch in LiNbTaO_3 Waveguide	3-7
3-5	Cross-section of Ti-Diffused LiNbO_3 Waveguide With SiO_2 Buffer Layer and Electrodes	3-11
3-6	Two-Dimensional Interaction Between Light and a Phase Grating	3-13
3-7a	Bragg Angle Condition	3-15
3-7b	Traveling Wave Interaction	3-16
3-8	Deflection by Phase Grating and Light Beams of Finite Width	3-18
3-9	Scattering with Phase Grating and Light Beams of Finite Width	3-20
3-10	The Construction for Finding the Indices of Refraction and the Allowed Polarization Directions for a Given Direction of Propagations	3-23
3-11	Coordinate Transformations	3-27
4-1	Integrated Optics Switching 4 X 4 Matrix (Using Wider Switches)	4-2
4-2	Integrated Optics Switching 4 X 4 Matrix (Using Wider Switches) Cross Section Through Optical Waveguide	4-4
4-3	Integrated Optics Switching 4 X 4 Matrix (Using Narrow Switches)	4-7
4-4	Integrated Optics Switching 4 X 4 Matrix (Using Narrow Switches) Cross Section Through Optical Waveguide	4-8

LIST OF ILLUSTRATIONS (Cont.)

<u>Figure</u>	<u>Title</u>	<u>Page</u>
5-1	AlGaAs Array	5-2
5-2	Relative Nb and Ta Concentration as a Function of Depth Below the Surface	5-4
5-3	Index Change $\Delta n = n_s - n_b$ Versus Diffusion Depth $Y_0 = D/\lambda$ in Units of Free-Space Wavelength, Showing the Number of Waveguide Modes.	5-6
5-4	Transverse Electromagnetic Field Distribution in A Planar Diffused Waveguide as a Function of the Normalized Depth y/D	5-7
5-5	Beam Transformation From Optical Fiber to Planar Optical Waveguide	5-9
5-6	Beam Transformation From Optical Fibers to Switching Matrix	5-10
5-7	Angle Transformation by Optical Fiber Core for Different Spacings $s-R$ between Object and Vertex	5-13
5-7a	Deviation from Spherical Wavefront (In Fractions of an Optical Wavelength)	5-15
5-8	Angle Transformation by Optical Fiber Core for Different Spacings	5-17
5-9	Optical Connection Between Sections of Switching Network	5-20
6-1	Cross Talk Reduction	6-2
7-1	Structure of DH Diode Laser With P-Type Active Layer (n-p-p) DH structure	7-3
7-2	Radiative Indirect Transition	7-5
7-3	Mole Fraction AlAs	7-6
7-4	Schematic of Real Refractive-Index Profile	7-9
7-4	Schematic of Spatial Gain Profile	
7-5	Schematic Cross Section of the Channeled-Substrate Planar (CSP) laser	7-10

LIST OF ILLUSTRATIONS (Cont.)

<u>Figure</u>	<u>Title</u>	<u>Page</u>
8-1	Interferograms: (a) Ordinary Wave, (b) Extraordinary Wave; (c) Extraordinary Wave, (d) Extraordinary Wave	8-6
8-2	Experimental Index Profiles in LiNbO_3 and LiTaO_3 for Diffusion Normal to z .	8-7
8-3	Schematic of Fabrication of Metal Electrodes	8-15
8-4	Schematic Diagram of a Simple Vacuum Frame for Obtaining Intimate Contact Between a Substrate and a Conformable Photomask	8-17
8-5	Scanning Electron Micrograph of the Cross Section	8-18
8-6	Scanning Electron Micrograph of the Cross Section of a Grating Pattern Exposed in AZ1350H photo-resist.	8-18
8-7	Scanning Electron Micrograph of the Cross Section of the Edge of a Pattern Exposed in AZ1350 Photo-resist, 5000 Å thick	8-19
9-1	Fiber Fusion Splicing Set	9-2
10-1	Conceptual Design of Optical Switching System	10-2
10-2	Conceptual Design of Optical Switching System (in operation)	10-3
10-3	Access Technique in Common Control Space-Division Switching System	10-4

LIST OF TABLES

<u>Table</u>	<u>Title</u>	<u>Page</u>
1-1	Data Handling System Assumptions	1-2
3-1	Switching Options	3-2
3-2	Comparison of Various Technology Options	3-3
8-1	Properties of Single Domain Crystals	8-4
12-1 & 12-2	Phasing Charts	12-3 12-4

SECTION 1 STATEMENT OF PROBLEM

The problem to be addressed is the design of a high data rate switching center for a satellite tracking station. A specific characteristic of this station is the comparatively long distances for the transmission of information to the switching network. Consequently, high data rate optical fibers are considered for the inter-connect links. The feasibility study considers the implementation of an optical switching center using an integrated optics switching matrix. The study includes a comparison with opto-electronic and electronic switching networks. Also, the study identifies and details a program for developing and implementing an integrated optics switching center.

Specific requirements for the switching center are:

- ° Data rate throughput up to 300 Mb/s, with 8 input lines and 16 output lines.
- ° The switching network should have the capability of connecting each input to each output.
- ° The input and output lines of up to 200 ft. length should be optical fibers.
- ° The integrated optical switching center should be operational by 1982.
- ° Table 1-1 is a summary of the assumed design specifications for the switching network.

Table 1-1. Data Handling System Assumptions

System Parameter	Assumed Requirement
1) Longest path length	100 to 200 feet
2) Data rate of each path	Up to 300 Mb/s
3) Number of switching input ports	Up to 8
4) Number of switching output ports	Up to 16
5) Power limitation	Essentially none, but objective of less than 250 watts
6) Switching speed	Greater than 100 Hz, but preferred at up to 1 MHz
7) Signal-to-noise ratio	Greater than 20 dB
8) Channel crosstalk	Better than 25 dB with objective of 50 dB
9) Maximum insertion loss from input	50 dB
10) Carrier wavelength	Desire operation in the $\lambda = 1.0$ to $1.2 \mu\text{m}$ range; will accept operation in the $\lambda = 0.8$ to $0.9 \mu\text{m}$ range
11) Signal distortion due to switching network	Less than 1% PID (peak individual distortion)
12) Electromagnetic interference	Unaffected by EMI
13) Cost of system hardware and software	Reasonably low (\$100 K to \$250 K)

SECTION 2 SUMMARY

A detailed feasibility study of the described switching network using an integrated switching matrix has been found to be the optimal solution to meet the requirements outlined in Section 1. This conclusion results from capability of an integrated optic switch plus the switch's ability to provide the desired connectivity while requiring a minimum of electronic hardware. The preferred integrated optical switching scheme has been found to be an electro-optic Bragg diffraction switch.

To ascertain the advantages of the integrated optics switching center, its properties were compared to those of opto-electronic and to electronics switching networks. These techniques were found to have the following characteristics:

- ° The opto-electronic switching network combines optical distribution from the input to the output terminals with electronic switching, to form the appropriate connections. For an $n \times m$ switching network an opto-electronic network requires n light sources, but $n \times m$ photodetectors and preamplifiers. This requirement leads to a high cost and lower reliability.
- ° The electronic switching network can also meet the requirements outlined in Section 1. This configuration can be built of multiplexers using "100 Series Emitter Coupled Logic" produced by Fairchild. The multiplexers are designed with 50 ohm transmission lines. However, for every two multiplexers a buffer circuit is required adding considerably to the complexity and power consumption of the switching network.

In a briefing meeting at NASA-Goddard Space Flight Center on July 17, 1978, a comparison of the three techniques (integrated optics, hybrid and electronic) were presented. The customer approved the completion of the integrated optics conceptual design. This approval was given, since the integrated optical switching concept has been found to be the optimal solution because of its high efficiency, high reliability, minimal power consumption, wide bandwidth, simple distribution and the ability to connect the optical fibers to an optical switching matrix.

2.1 ELECTRO-OPTIC BRAGG DIFFRACTION SWITCH

The electro-optic Bragg diffraction switches that make up the integrated switching matrix option are double pole-double throw structures formed in planar waveguide. In the switch "on" position, a voltage is applied to the interdigital electrodes, which induces a phase grating in the optical waveguide. The incident light from the input terminal is deflected by the phase grating to the output terminal. When the voltage is removed for the "off" position, the incident beam passes through the switch without leakage or scattering.

2.2 SWITCHING MATRIX WITH ELECTRO OPTIC BRAGG DIFFRACTION SWITCHES

In the switching matrix the switches connect each input port to any output port. A key factor is that for each connection only one switch needs to be energized. Moreover, one input port is connected to two, three, or to all output ports. In the switching matrix the incident laser beams in the planar waveguides are terminated by absorbing film sections after passing through all the switches. Terminations are required for the switched "on" position since not all the laser radiation is deflected by the induced phase grating.

The electro-optic substrate of the switching matrix optical waveguide is a ferro-electric single crystal of either LiNbO_3 or LiTaO_3 . The waveguide is formed by diffusion of Ti into LiNbO_3 or by diffusion of Nb into LiTaO_3 . The substrate orientation of the switching matrix has been evaluated, using the theory for the linear-optical effect in optically uniaxial crystals. Further, the polarization of the incident laser beam, and the orientation of the interdigital electrodes has been derived to obtain the largest change in refractive index with the electric field.

2.3 ENDFIRE COUPLING BETWEEN OPTICAL FIBERS AND WAVEGUIDE SWITCHING MATRIX

Because of the size limitations of single crystal LiNbO_3 the optical connections between input fibers and the switching matrix must be implemented by endfire-couplers. Endfire coupling between the input or output optical fibers and the switching matrix requires three cylindrical microlenses. The microlenses are formed from the core of optical fibers. One fiber core can function simultaneously as a microlens for all input or output fibers, transforming the radiation from all input or output fibers into the planar waveguide.

The beam transformation properties of the cylindrical microlenses have been computed. The results indicate that their spherical aberrations are quite small over a large angular range of the incident radiation.

2.4 CROSSTALK REDUCTION

A novel method of crosstalk reduction based on diffraction theory has been developed. This technique uses an iris in the focal plane of the output coupler lens to reject all waves except the coherent wave from the output beam.

2.5 INJECTION LASER

The characteristics of AlGaAs injection lasers for the optical transmitters have been described with special emphasis on single transverse mode, double heterostructure AlGaAs lasers. This single mode structure is needed because the operation of the electro-optic Bragg diffraction switch requires single transverse mode radiation for operation. For efficient coupling and ease of modulation a separate laser is required for each input terminal of the switching matrix.

2.6 MODULATION

An analysis of high bit rate direct modulation of the AlGaAs DH laser has been developed. It has been found that distortions from time delay, prepumping and damped oscillation can be greatly reduced using a dc bias with an ac overdrive signal and an output bandpass filter.

2.7 FABRICATION OF THE PLANAR OPTICAL WAVEGUIDES AND INTERDIGITAL ELECTRODES FOR THE ELECTRO-OPTIC BRAGG DIFFRACTION SWITCH

2.7.1 Titanium Diffusion

To form a waveguide of LiTiNbO_3 on a LiNbO_3 substrate, diffusion of Ti at a temperature of approximately 980°C in an Argon atmosphere must be performed. For the Ti-diffused waveguide to maintain single mode operation the diffusion constant must be held between 1 and 1.7 wavelength (in air).

2.7.2 Buffer Layer

A buffer layer of approximately 1000\AA must be coated on the Ti-diffused waveguide. This layer preserves the mode characteristics of waves passing through the electrode region of the switch.

2.7.3 Photolithography and Lift-Off Technique

The interdigital electrodes are formed by photolithography together with lift-off techniques. Combining these two techniques a precision of better than 1 micron should be obtainable.

2.8 CONCLUSION AND CONTINUATION OF PROGRAM UNTIL COMPLETION

The feasibility study shows that a high data rate switching center can be implemented using an integrated optics switching matrix with electro-optic Bragg diffraction switches. This approach can meet the requirements outlined in the Statement of Work and can be operative by 1982. The different phases of the program until the completion are given in the form of phasing charts.

2.9 ADDITIONAL STUDIES[®]

To ascertain the optimized design for the integrated optics switching matrix, the "Cobra" switch and the acousto-optic Bragg diffraction switch were investigated and compared to the chosen design. Other coupling schemes were evaluated including prism and grating couplers.

SECTION 3

INTEGRATED OPTICS SWITCHING CONCEPT

The integrated optical switching concept has been compared to other switching methods. Their key parameters are given in Table 3-1 and 3-2. The integrated optical switching concept has been found to be the optimal solution because of its high efficiency, high reliability, minimal power consumption, wide bandwidth, simple distribution and the ability to connect the optical fibers to an optical switching matrix.

The schematic of the switching system using an integrated optical switching matrix is shown in Figure 3-1. The key factor of this design is that for each connection only a single switch needs to be energized as shown on Figure 3-2. This is of special importance because the remaining switches in the "off" position do not affect adversely the propagating optical waves.

The switches of the switching matrix are electro-optic Bragg diffraction switches in planar waveguide. The switching system is designed for high data rate (up to 300 Mb/s). Because of the high data rate and because of the considerable distances for transmission of the information, optical fibers are used from the optical transmitter to the switching matrix. The digital data stream of each channel is modulated on an AlGaAs injection laser. The properties of the integrated optics switching network require that the laser be a single transverse mode laser and that the input connections are made by single mode optical fibers. The optical fibers are coupled by an endfire method to the switching matrix. The coupling technique uses microlenses, formed by the core of optical fibers, to form the required laser beam with large aspect ratio.

3.1 ELECTRO-OPTIC BRAGG DIFFRACTION SWITCH

The electro-optic Bragg diffraction switch is a double-pole-double-throw switch. A typical thin-film electro-optic Bragg diffraction switch is shown in Figures 3-3 and 3-4. The switch is based on the linear

Table 3-1. Switching Options

<u>METHOD</u>	<u>RESULTS</u>
INTEGRATED OPTICS	MOST EFFICIENT IN SWITCH HIGHEST RELIABILITY MINIMAL POWER CONSUMPTION GOOD TO A FEW GB/S REQUIRES DEVELOPMENT
HYBRID (OPTO ELECTRONIC)	REQUIRES INTEGRATED ANALOG DEVICES INERS EFFECTING RELIABILITY AND FLEXIBILITY MODEST POWER CONSUMPTION GOOD TO 500MB/S REQUIRES DEVELOPMENT
ELECTRONIC	HIGH POWER CONSUMPTION GOOD TO 300 MB/S LOWER RELIABILITY REQUIRES LITTLE DEVELOPMENT

Table 3-2. COMPARISON OF VARIOUS TECHNOLOGY OPTIONS
(In Matrix Form)

SWITCHING TECHNIQUE	EFFICIENCY		POWER CONSUMPTION		BANDWIDTH		DEVELOPMENT EFFORT	
	High	Medium	Low	Medium*	Up to a few Gb/s	Up to 500 Mb/s	Up to 300 Mb/s	Requires Development
Integrated Optics	High	Medium	Medium	Medium*	Up to a few Gb/s	Up to 500 Mb/s	Up to 300 Mb/s	Requires Development
Hybrid (Opto-Electronics)	Medium	Medium	Medium	Medium	Up to a few Gb/s	Up to 500 Mb/s	Up to 300 Mb/s	Requires Development
Electronic	Low	Medium	High	High	Up to a few Gb/s	Up to 500 Mb/s	Up to 300 Mb/s	Requires Little Development

*Requires n X m analog receivers effecting reliability and complexity

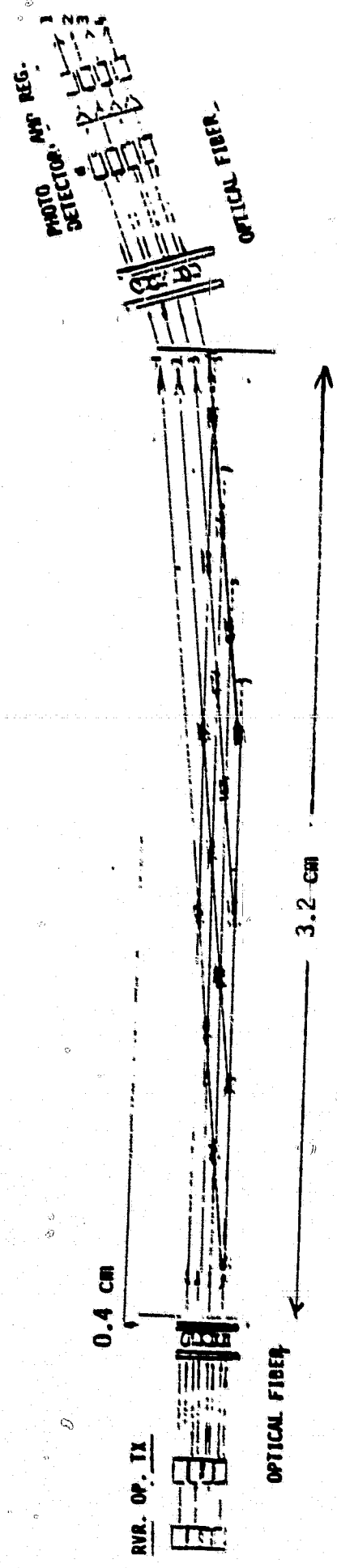


Figure 3-1. Integrated Optics Switching Center with 4x4 Matrix (Using Wider Switches)

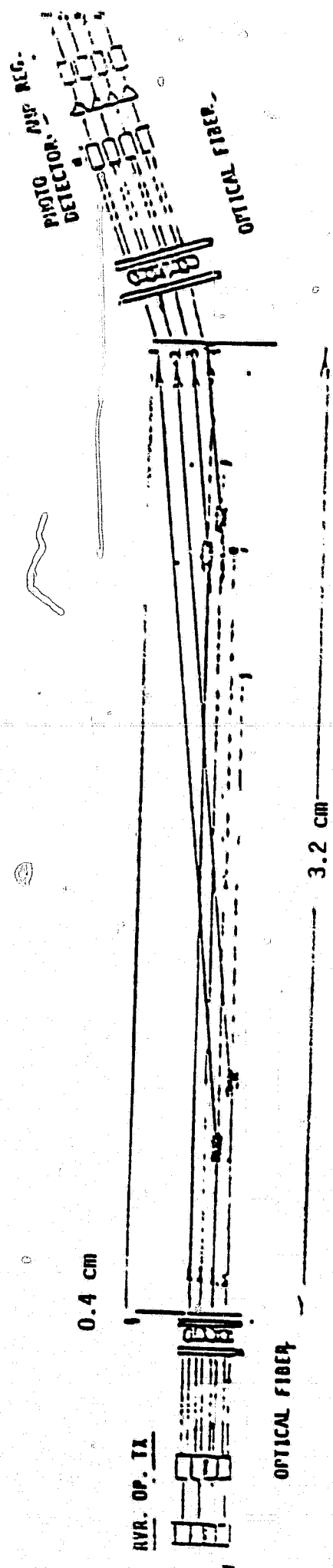


Figure 3-2. Integrated Optics Switching Center with 4x4 Matrix (using Wider Switches) In Operation

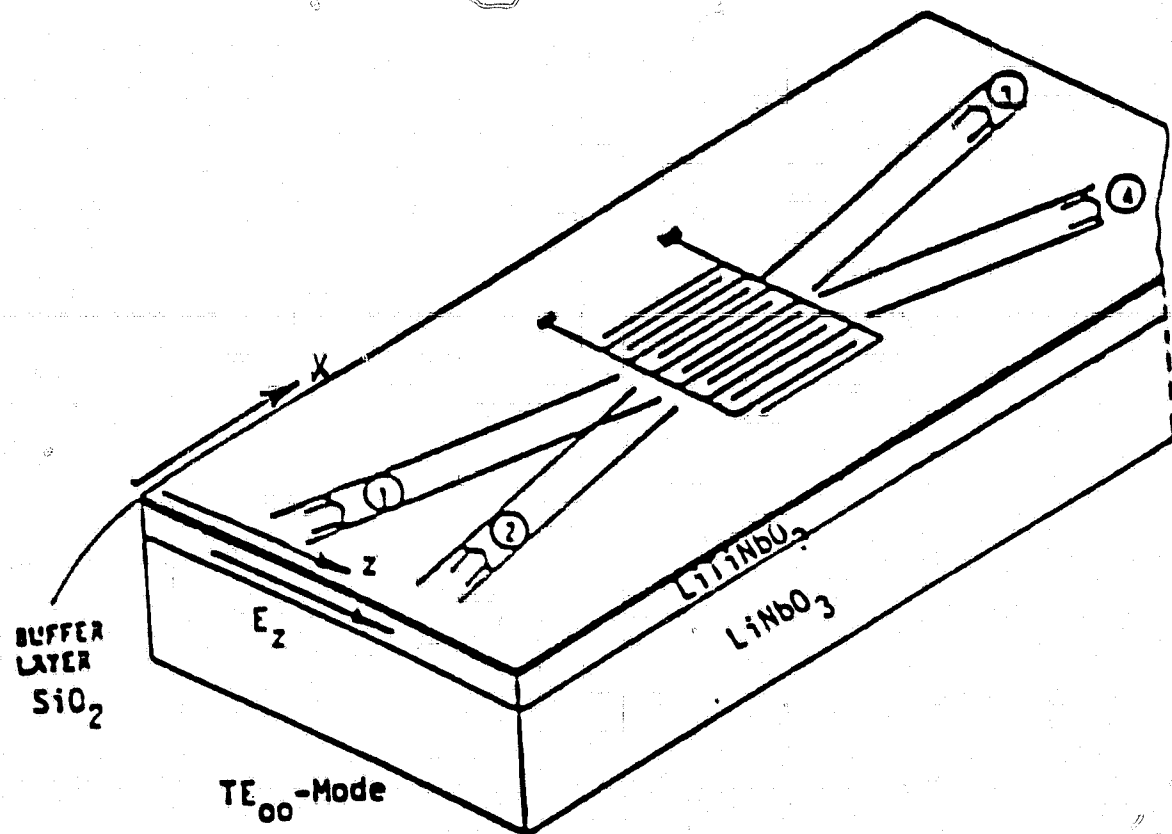


Figure 3-3. Electro-Optic Bragg Diffraction Switch in LiTiNbO_3 Waveguide

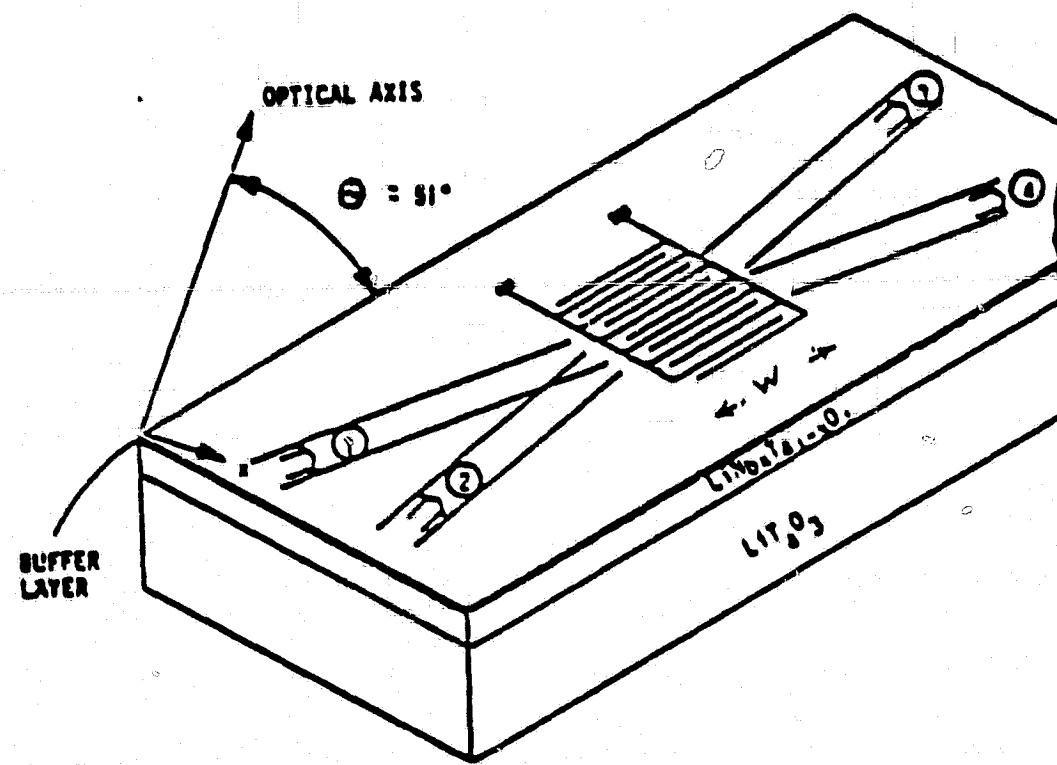


Figure 3-4. Electro-Optic Bragg Diffraction Switch in LiNbTaO_3 Waveguide.

electro-optic effect, where an external electric field can change the refractive index of a ferroelectric material as LiNbO_3 or LiTaO_3 . The optical switch is built into a planar waveguide which is formed by in-diffusion of metal into the ferroelectric substrate. An inter-digital electrode structure is formed on top of the optical waveguide. A thin buffer layer between the metal electrodes and the optical waveguide minimizes the effect of the metal electrodes on the optical waveguide mode.

In the thin-film Bragg diffraction switch the optical waves are guided by the planar optical waveguide in the y-direction. In the x-z plane the laser radiation is collimated by external optics.

In the "on" position of the switch a voltage is applied to the interdigital electrodes. The spatially periodic electric field is parallel to the waveguide plane and close to perpendicular to the direction of the propagation of the incident light beams. The intensity of the electric field falls off with distance from the electrodes. The spatially periodic electric field gives rise to spatially periodic refractive index variations, forming an induced Bragg diffraction grating in the optical waveguide. The grating deflects, in a travelling wave mode, the incident laser radiation from terminal 1 to terminal 3 and from terminal 2 to terminal 4. But only approximately 80 percent of the incident energy is deflected.

In the "off" position the voltage is removed from the electrodes, and the refractive index of the optical waveguide again is uniform. The incident laser radiation propagates from terminal 1 to 4, and from terminal 2 to 3. In fact, in the "off" position, the switch does not affect the propagating waves at all. It is this property of the Bragg diffraction switch in planar waveguide in Figures 3-3 and 3-4, which is of major importance for its use in the integrated switching matrix. The incident waves can propagate through many switches which are in the "off" position without experiencing scattering or crosstalk.

The electro-optic Bragg diffraction switch in Figure 3-3 is fabricated from a x-z cut LiNbO_3 substrate, where the thin film waveguide

is formed by titanium diffusion. The direction of propagation of the laser beam is along the x axis. The electric field vector of the incident wave is parallel to the z-axis, thus setting up the TE-mode in the optical waveguide. The orientation in Figure 3-3 was chosen because the electro-optic effect in the LiNbO_3 crystal is largest when the voltage is applied along the optical axis and the light propagates perpendicular to the optical axis.

The Ti-diffusion into a LiNbO_3 single crystal to form an optical waveguide, produces a composition gradient where the titanium mole fraction decreases towards the interior of the crystal. The refractive index decreases from the value at the surface, n_s , to the refractive index of the substrate n_b . For the extraordinary refractive index $n_s - n_b = \Delta n_e = 0.04$.

In an alternate design, shown in Figure 3-4, the electro-optic Bragg diffraction switch is fabricated from a x-z plane LiTaO_3 substrate, cut under an angle of 51° to the optical axis. The thin-film waveguide is formed by Niobium diffusion to form $\text{LiNbTa}_{1-x}\text{O}_3$. The incident light beams form angles of close to 50° with the optical axis of the LiTaO_3 crystal. The optical waves are in the TE_0 -mode with the electric field vector parallel to the waveguide plane. The angle of close to 50° between the incident optical beams and the optical axis of the crystal yields close confinement of the waveguide mode, since the difference in refractive index of LiNbTaO_3 and LiTaO_3 , for this orientation, is comparatively large. Also, the electro-optic coefficient under this angle is comparatively large; specifically, $n_s - n_b = \Delta n = 0.058$ and $r' = 34.4 \times 10^{-12} \text{ m/V}$.

For the electro-optic Bragg diffraction switch the Ti-diffused LiNbO_3 waveguide can have certain advantages over the $\text{LiNb}_{x}\text{Ta}_{1-x}\text{O}_3$ waveguide. The switch with the Ti-diffused LiNbO_3 waveguide can be cut along the crystal axes while the switch with the $\text{LiNb}_{x}\text{Ta}_{1-x}\text{O}_3$ waveguide must be cut under an angle of 51° to the optical axis. For this reason it should be possible to obtain for the substrate of the switching matrix larger single LiNbO_3 crystals than LiTaO_3 crystals. Also, the temperature for diffusing titanium is below the Curie temperature of LiNbO_3 . However, the temperature for diffusing Nb into LiTaO_3 exceeds the Curie temperature of LiTaO_3 and requires repoling after the diffusion. However, consideration

must be given that laser damage has been observed in LiNbO_3 crystals under intense laser radiation.

The periodic metal electrodes of the Bragg diffraction switch in Figures 3-3 and 3-4 are not deposited directly on the thin-film optical waveguide. The field distribution in the optical waveguide is such that the evanescent field extends into the substrate and into the superstrate, as shown schematically in Figure 3-5. For the coordinate system in Figures 3-3 and 3-4, the evanescent field in the superstrate for the TE-mode is

$$E \approx \exp\left(-\frac{y}{n_2}\right) \quad 3-(1)$$

where the decay factor $\frac{1}{n_2}$ becomes larger when the superstrate is metal rather than air or dielectric.

When the electrodes are deposited directly onto the thin-film waveguide, the mode characteristics of the waveguide in portions where the electrode strips are present will be different from those where the electrode gaps are. Consequently, even in the absence of any applied electric field, the periodic electrodes would act as a weak grating and cause the light beam to be deflected. Its deflection angle will be twice the deflection angle due to the applied electric field. To alleviate the effect of the metal electrodes, a buffer layer in form of 1000\AA SiO_2 thin-film should be coated on the Ti-diffused LiNbO_3 , as shown in Figure 3-3 and Figure 3-5, and on the Nb-diffused LiTaO_3 in Figure 3-4.

3.1.1 Analysis of Electro-Optic, Thin Film, Bragg Diffraction Switch

The most significant characteristic of the Bragg effect is that a phase grating with a periodicity large compared to an optical wavelength, can deflect an incoming laser beam into a single, first order, diffraction beam (rather than in a multitude of grating lobes). This characteristic is related to the finite width of the grating. The Bragg effect occurs only when the width of the phase grating w exceeds a certain value, which is defined through the Q factor; it is

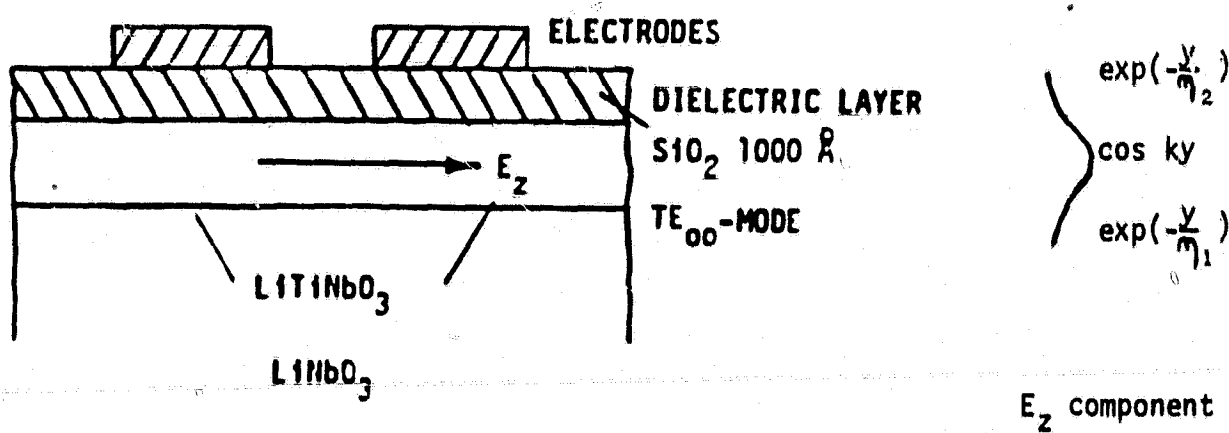


Figure 3-5. Cross-section of Ti-diffused LiNbO_3 waveguide with SiO_2 buffer layer and electrodes.

$$Q = \frac{2\pi\lambda_0}{n\Lambda} w \quad (3-2)$$

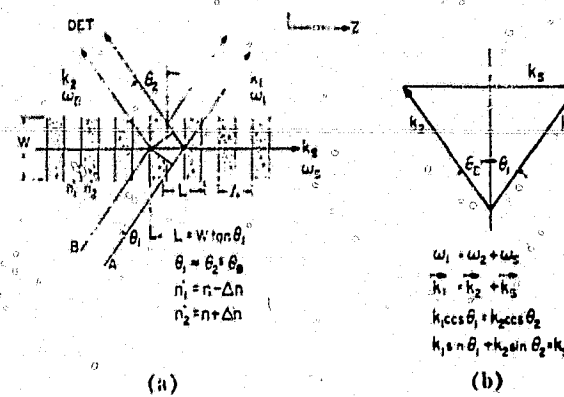
where $\lambda = \frac{\lambda_0}{n}$ is the optical wavelength in the optical waveguide with the refractive index n and Λ is the periodicity of the phase grating. The Bragg condition requires that $Q > 10$.

The electro-optic Bragg diffraction switch in Figures 3-3 and 3-4 is a double-pole-double-throw switch. The switching function takes advantage of the linear-optics effect, where an external electric field can change the refractive index of a ferro-electric material like LiNbO_3 or LiTaO_3 . The thin-film Bragg diffraction switch is built into a planar (one-dimensional)optical waveguide. To form a phase grating in the optical waveguide, a periodic electric field is set up by the interdigital electrodes, which are placed on top of the optical waveguide. The periodic electric field changes periodically the refractive index in the optical waveguide and thus, generates the phase grating.

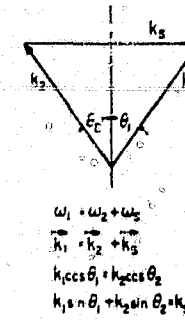
The periodic change in refractive index from $n_2 = n + \Delta n$ to $n_1 = n - \Delta n$ set up by the periodic electric field, is schematically shown in Figure 3-6. (Though the fundamental spatial electric field component follows a cosine function, the phase grating is shown discontinuous in the illustration). However, the change of the refractive index introduced by the electro-optic effect is extremely small. Efficient Bragg diffraction requires appreciable phase modulation and must rely on traveling wave interaction. The phase grating couples the diffracted wave to the incident wave. As the incident wave travels across the phase grating the multiple periodic reflections will add in phase, when $\theta_i = \theta_d = \sin^{-1}(\lambda_0/2n\Lambda)$ (3-3) where θ_i and θ_d are the angles of the incident and the diffracted waves inside the dielectric, as shown in Figure 3-7a. Thus, the incident laser beam forms an angle of

$$\theta_i + \theta_d = \sin^{-1}(\lambda_0/n\Lambda)$$

with the deflected laser beam.



(a)



(b)

Figure 3-6. Two-Dimensional Interaction Between Light and a Phase Grating

(P. Quate, C. D. W. Wilkinson and D. K. Winslow, Proceeding IEEE, Vol. 53, No. 10, Oct. 1965).

For the implementation of the electro-optic Bragg diffraction switch it is important to realize, that the symmetry of the incident and deflected beam, in reference to the stratifications of the phase grating, that is $\theta_i = \theta_d$, yields the highest deflection efficiency. However, the angle between incident and deflected beams of $\theta_i + \theta_d$ still remains the same, even when $\theta_i \neq \theta_d$. But for $\theta_i \neq \theta_d$ the deflection efficiency becomes smaller.

The travelling wave interaction introduced by the phase grating results in an exponential decay of the incident wave and an exponential build up of the diffracted wave. Since the changes in amplitudes of the incident and diffracted waves are introduced by the reflections at each of the stratifications, their amplitudes vary only in the direction perpendicular to the stratification. The variation in amplitudes of the incident and the diffracted waves for the crystal orientation in Figure 3-7b is given by

$$E_1(z) \propto e^{-\Gamma_d z} \quad \text{and} \quad E_2(z) \propto e^{\Gamma_d z} \quad (3-5)$$

where z extends from $z = 0$ to $z = w \tan \theta_i$, which is the projection of the propagation path across the phase grating, on the z -direction, as shown in Figure 3-7b.

From the limitation of the travelling wave interaction length to $z = w \tan \theta_i$ follows that the efficiency of converting the incident light to the diffracted light is proportional to the width of the phase grating. The ratio of the diffracted light intensity I_d to the incident light intensity I_i is

$$I_d/I_i = \sin^2(\Delta\phi/2) \quad (3-6)$$

where

$$\Delta\phi = kw\Delta n \quad (3-7)$$

$$k = \frac{2\pi}{\lambda_0}$$

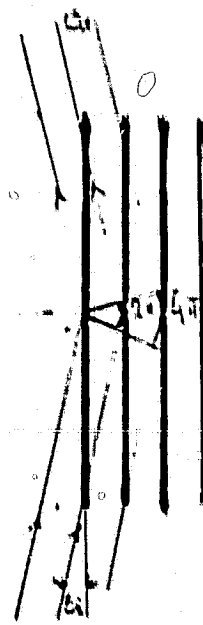


Figure 3-7a. Bragg Angle Condition

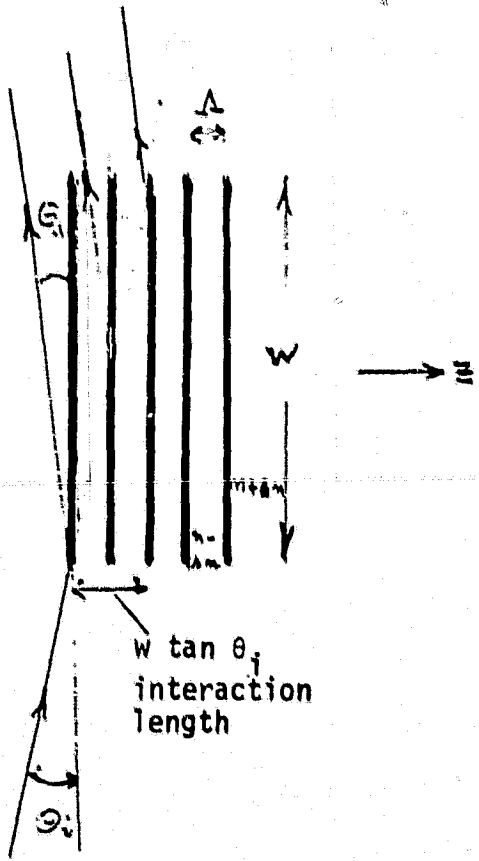


Figure 3-7b. Traveling Wave Interaction

λ_0 is the optical wavelength in air, and Δn is the change in refractive index of the electro-optic waveguide, introduced by the external electric field. In general form

$$\Delta\phi = -\pi \frac{w}{\lambda_0} (n')^3 r' E_e. \quad (3-8)$$

For the electro-optic Bragg diffraction switch configuration in Figure 3-3 from Eq. 3-14

$$n' = n_e$$

$$r' = r_{33}$$

$$E_e = E_{z,e},$$

where n_e is the refractive index of the extraordinary ray of the uniaxial LiNbO_3 crystal, r_{33} is one of the electro-optic tensor components of LiNbO_3 , and $E_{z,e}$ is the in-plane component of the external electric field, set up by the interdigital electrodes. For the electro-optic Bragg diffraction switch configuration in Figure 3-4, n' , r' and E_e are given by Eqs. 3-20, 3-21 and 3-16.

From Eq. 3-6 it follows that to diffract all the incident light, $\Delta\phi$ must become π . The phase change $\Delta\phi$ in Eq. 3-8 contains the product of the width of the phase grating times the electric field. A wider phase grating would require a lower electric field.

However, consideration must be given that the width of the phase grating also affects the ratio of the beamwidth of the diffracted light beam to the beamwidth of the incident light beam. This is because the number of stratifications which contribute to the diffracted light beam is not necessarily the same as the number of stratifications which are illuminated by the incident beam as shown in Figure 3-8b. The width of the diffracted beam which results from multiple reflections at the stratifications of the phase grating is only the same as the beamwidth of the incident beam when the width w of the phase grating is narrow.

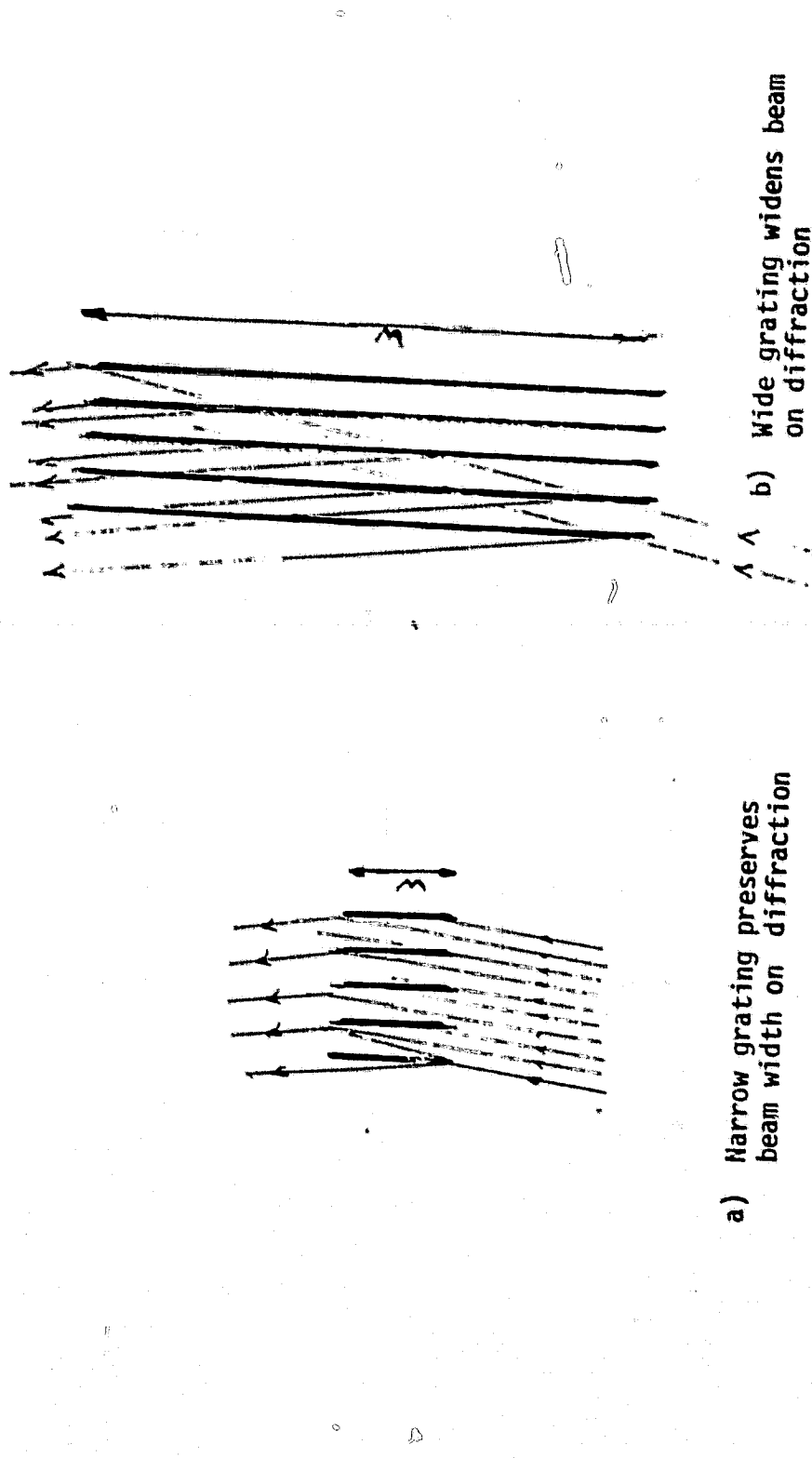


Figure 3-8. Deflection by Phase Grating and Light Beams of Finite Width

(Figure 3-8a). When the width of the phase grating exceeds that of the incident laser beam, the width of the diffracted beam will approximate the width of the phase grating. (Figure 3-8b).

This is also illustrated in the momentum diagram in Figure 3-9. In Figure 3-9 the diffraction spread of the optical beam, $\delta\phi$, is related to the diffraction spread $\delta\theta$. The diffraction spread of the optical beam is

$$\delta\phi = \frac{\lambda}{N_i\Lambda}$$

where N_i is the number of stratifications illuminated by the incident laser beam. The diffraction spread $\delta\theta$ is inversely proportional to the width of the phase grating, it is

$$\delta\theta = \frac{\Lambda}{W}$$

When $\delta\theta \gg \delta\phi$ (Figure 3-9a) the width of the diffracted light beam is the same as the width of the incident light beam. This is also illustrated in Figure 3-8a, where a wider laser beam of the width $N_i\Lambda$ is diffracted by a narrow phase grating of the width w , and the width of the diffracted beam remains the same as the width of the incident beam. When $\delta\phi \gg \delta\theta$ (Figure 3-9b) the diffracted beam becomes considerably wider, in fact it approximates the width of the phase grating. The same relation is illustrated in Figure 3-8b.

For the switching matrix using electro-optic Bragg diffraction switches the width of the incident as well as of the diffracted laser beam is restricted by the requirement for low cross talk. The expansion of the laser beams, along the optical propagation paths on the switching matrix is typical for the expansion in the near-field. The expansion of the Gaussian half-width of the diffracted laser beam with distance from the phase grating, is given by

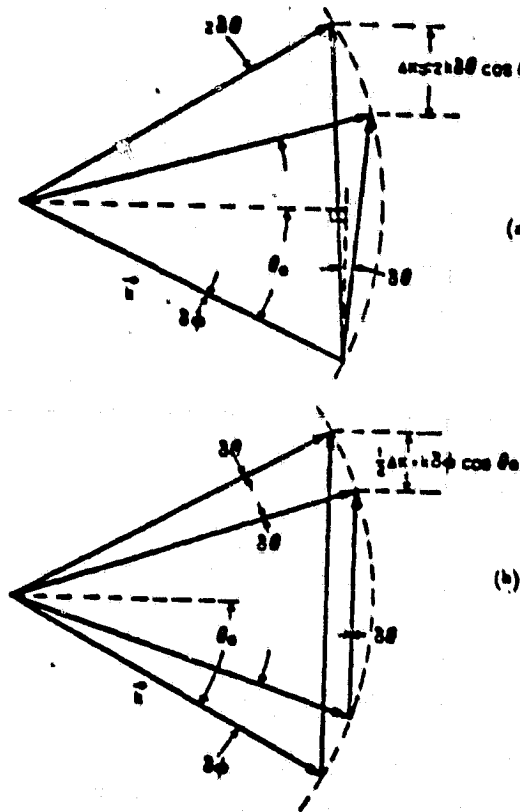


Figure 3-9. Scattering with Phase Grating and Light Beams of Finite Width. The Diffraction Angle of the Light is $\delta\phi$ and that of the Phase Grating is $\delta\theta$. There are Two Possible Configurations:

(a) $\delta\theta > \delta\phi$ or (b) $\delta\phi > \delta\theta$

For (a) the Scattered Light Beam has a Diffraction Angle $\delta\phi$, for (b) the Diffraction Angle is $\delta\theta$.

$$w^2(x) = \frac{w_0^2}{1 + \left(\frac{\lambda_0 x}{n\pi w_0^2}\right)^2} \quad (3-9)$$

where w_0 is the Gaussian half-width of the diffracted laser beam at the phase grating.

Though a wider diffracted laser beam would expand slower than a narrower beam, the suppression of crosstalk would still be less effective. It follows that the requirement for low crosstalk limits the width of the diffracted laser beam not to exceed by far the width of the incident laser beam. This requires that $\delta\theta \gg \delta\phi$ and restricts the width of the phase grating.

3.1.2 Linear Electro-Optic Effect in Uniaxial Crystal

In an efficient thin-film electro-optic Bragg diffraction switch the optical waveguide as well as the substrate are of electro-optic material. In the switch configurations in Figures 3-3 and 3-4, the optical waveguide is formed by in-diffusion of metal into the substrate. The substrate itself, must be formed by a single crystal because the operation of the switch depends on the mono-crystalline structure of the electro-optic material.

The change of the refractive index (Δn in Eq. 3-7) of the Bragg diffraction switch, with an external electric field, is based on the linear electro-optic effect. The electric field applied to the periodic electrodes of the switch alters the dielectric tensor of the electro-optic material.

The electro-optic substrate is a ferro-electric single crystal, of either LiNbO_3 or LiTaO_3 ; it is optically uniaxial, that is, the highest degree of rotational symmetry applies only to a single axis, (the optical axis). It is an anisotropic crystal where the physical properties vary with direction. For an electro-magnetic wave propagating through the anisotropic crystal the electric displacement vector D and the electric

field vector \vec{E} are not necessarily parallel. Their relation can be described by the dielectric tensor ϵ_{kl} defined by

$$D_k = \sum_l \epsilon_{kl} E_l \quad (3-10)$$

To determine the velocities of propagation in the anisotropic crystal the ellipsoid of wavenormals has been defined from the electric energy density, using an axis transformation to the principal dielectric axis of the crystal. It is given by

$$\frac{x^2}{n_x^2} + \frac{y^2}{n_y^2} + \frac{z^2}{n_z^2} = 1$$

The major axes coincide in directions with the principal dielectric axes, the length of the semiaxes are equal to the principal refractive indices. The ellipsoid of an uniaxial crystal with z being the optical axis, is given by

$$\frac{x^2}{n_o^2} + \frac{y^2}{n_o^2} + \frac{z^2}{n_e^2} = 1$$

The refractive indices n_o and n_e are those of the ordinary and extraordinary ray. The ellipsoid for an uniaxial crystal is shown in Figure 3-10. When a light beam propagates through the crystal at the direction \vec{s} in Figure 3-10, the intersection plane through the origin of the ellipsoid, normal to \vec{s} , is an ellipse. The refractive index $n_e(\theta)$ of the extraordinary ray is equal to the length of the semimajor axis OA. The electric displacement vector $\vec{D}_e(\theta)$ is in the $s - z$ plane, it is along OA. The index of refraction of the ordinary ray is independent of θ . The electric displacement vector \vec{D}_o is normal to the $s - z$ plane. In Figure 3-10 where the projection of \vec{s} on the $x - y$ plane coincides with the y - axis, the electric displacement \vec{D}_o is along the x - axis, that is along OB.

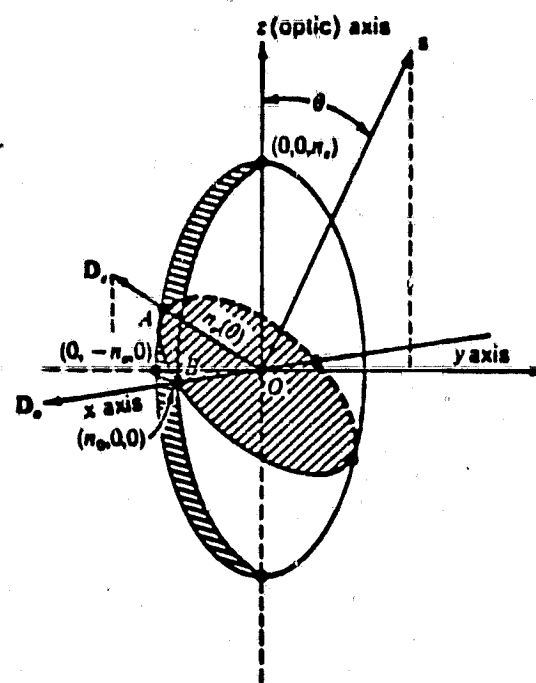


Figure 3-10. The Construction for Finding the Indices of Refraction and the Allowed Polarization Directions for a Given Direction of Propagation. The Figure Shown is for a Uniaxial Crystal with $n_x = n_y = n_0$, z Being the Optic Axis
 (A. Yariv, "Quantum Electronics," Chapter 18.3)

In describing switching of guided waves, it is convenient to use coordinates appropriate to the geometry of the waveguide, which may not correspond to the principal coordinates of the bulk crystal. In a general coordinate system which is non-principal, the index ellipsoid is given by

$$\left(\frac{x^2}{n^2}\right)_1 + \left(\frac{y^2}{n^2}\right)_2 + \left(\frac{z^2}{n^2}\right)_3 + 2 \left(\frac{yz}{n^2}\right)_4 + 2 \left(\frac{xz}{n^2}\right)_5 + \left(\frac{xy}{n^2}\right)_6 = 1 \quad (3-11)$$

where $4 + 2$, $3, 5 + 1, 3$, and $6 + 1, 2$.

In an electro-optical crystal an external electrical field changes the refractive index. Specifically, the linear electro-optic effect, used in the switch, is characterized by a linear change of the

$\left(\frac{1}{n^2}\right)_i$ coefficients with electric fields. It is described by the electro-optic tensor r_{ij} through the relation

$$\nabla \left(\frac{1}{n^2}\right)_i = r_{ij} E_j \quad (3-12)$$

The electro-optic tensor r_{ij} is given in general form by

$$r_{ij} = \begin{bmatrix} r_{xxx} & r_{xxy} & r_{xxz} \\ r_{yyx} & r_{yyy} & r_{yyz} \\ r_{zzx} & r_{zzy} & r_{zzz} \\ r_{yzx} & r_{yzy} & r_{yzz} \\ r_{xzx} & r_{xzy} & r_{xzz} \\ r_{xyx} & r_{xyy} & r_{xyz} \end{bmatrix}$$

For LiNbO_3 the tensor is given by

$$r_{ij} = \begin{bmatrix} 0 & -r_{22} & r_{13} \\ 0 & r_{22} & r_{13} \\ 0 & 0 & r_{33} \\ 0 & r_{51} & 0 \\ r_{51} & 0 & 0 \\ -r_{22} & 0 & 0 \end{bmatrix}$$

where $r_{22} = -r_{12} = r_{61}$, $r_{51} = r_{42}$, and $r_{13} = r_{23}$.

The equation for the index ellipsoid from equations 3-11 and 3-12 is

$$(n_0^{-2} - r_{22}E_2 + r_{13}E_3)x^2 + (n_0^{-2} + r_{22}E_2 + r_{13}E_3)y^2 + (n_e^{-2} + r_{33}E_3)z^2$$

$$+ 2(r_{51}E_2)yz + 2(r_{51}E_1)xz + 2(-r_{22}E_1)xy = 1 \quad (3-13)$$

where E_1 , E_2 , E_3 , are external electric field components in the x, y and z directions.

The relations for LiTaO_3 are similar to those of LiNbO_3 .

In the electro-optic Bragg diffraction switch in Figure 3-3 the substrate is an x-z plane, single LiNbO_3 crystal. The optical waveguide is formed by diffusing titanium in the substrate to form LiTiNbO_3 . The direction of propagation of the laser beam is along the x axis. The electric field vector of the incident wave is parallel to the z-axis, thus setting up the TE-mode in the optical waveguide. The orientation in Figure 3-3 was chosen because the electro-optic effect in the LiNbO_3 crystal is largest when the voltage is applied along the optical axis and the light propagates perpendicular to the optical axis. Equation 3-13 for the index ellipsoid, specifies the linear electro-optic effect of LiNbO_3 . Because the Bragg angle which the incoming laser beam forms with the diffraction grating (set up by the periodic external electric field) is very small, the assumption

can be made, that only the $E_{z,e}$ component of the external electrical field needs to be considered. Then $E_{x,e} = E_{y,e} = 0$. Since the wave-normal is along x , in the equation for the index ellipsoid (Equation 3-13), $x = 0$. For the wave polarized along the optical axis z , the effect of the electrical field $E_{z,e}$ is to change the refractive index, so that the new index ($n_e + \Delta n_{e,E}$) is given by

$$\frac{1}{(n_e + \Delta n_{e,E})} = \frac{1}{n_e^2} + r_{33} \frac{E_{z,e}}{2}$$

Since Δn_e is small compared to n_e , to a good accuracy

$$\Delta n_{e,E} = -n_e^3 r_{33} \frac{E_{z,e}}{2} \quad (3-14)$$

From Table 8-1 for the LiNbO_3 crystal we obtain that $n_e = 2.175$ at 0.8 microns and $r_{33} = 30 \times 10^{-10}$ cm/V.

For the Ti-diffused LiNbO_3 optical waveguide, the largest increase of the extraordinary refractive index due to the Ti-diffusion is $\Delta n_e = 0.04$, (Section 3.1), so that n_e in Equation 3-14 is $n_e = 2.215$.

In the electro-optic Bragg diffraction switch in Figure 3-4 the substrate is an x - z plane, single LiTaO_3 crystal. The waveguide is made by diffusing metallic niobium into the substrate to form $\text{LiNb}_x\text{Ta}_{1-x}\text{O}_3$. The direction of propagation of the laser beam \vec{s} is under the angle θ in reference to the optical axis z . To evaluate the effective refractive index and the electro-optic coefficient the coordinate system x, y, z in Equation 3-13 must be transformed to the coordinate system x', y', z' , as shown in Figure 3-11.

$$\begin{aligned} x &= z' \sin \theta + x' \cos \theta \\ x &= y' \\ z &= z' \cos \theta - x' \sin \theta. \end{aligned} \quad (3-15)$$

The external electric field set up by the periodic electrodes in Figure 3-4 which is predominantly in the plane of the waveguide,

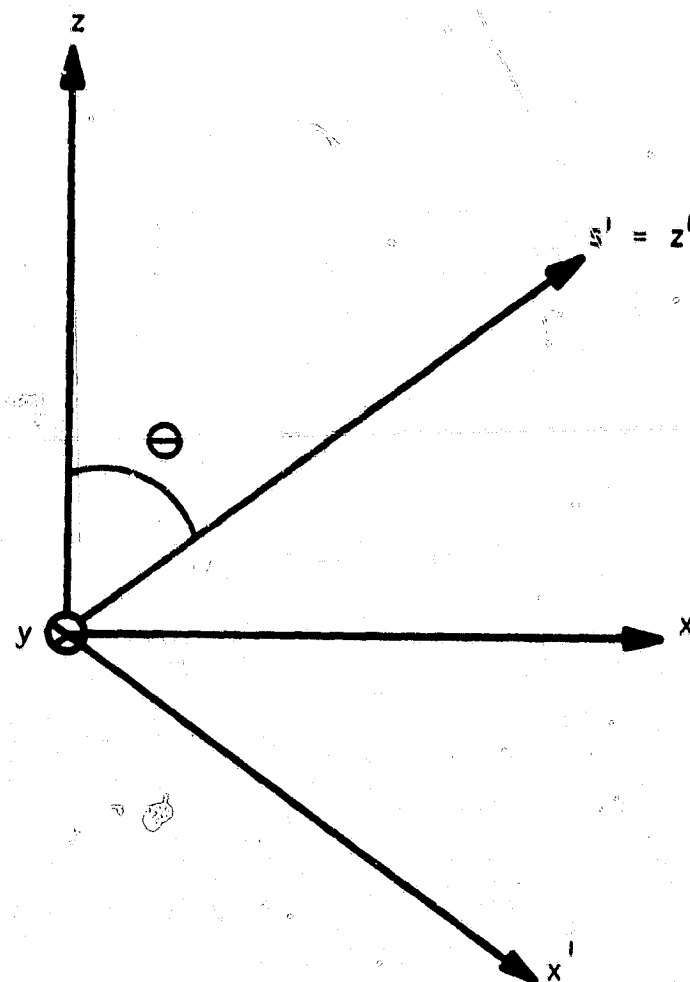


Figure 3-11. Coordinate Transformations

must also be transformed to the coordinates x' , y' , z' . It is

$$\begin{aligned} E_1 &= E_3' \sin \theta + E_1' \cos \theta \\ E_2 &= 0 \\ E_3 &= E_3' \cos \theta - E_1' \sin \theta. \end{aligned} \quad (3-16)$$

Because the Bragg angle which the incoming laser beam forms with the grating (set up by the periodic field) is very small, the assumption can be made, that only the E_1' component of the external electric field needs to be considered. To find the effective refractive index and the electro-optic coefficient for propagation in the \vec{s} direction, the equation of the ellipse, formed by the intersection of a plane normal to \vec{s} with the index ellipsoid in Equation 3-13 must be derived. From Equations 3-11, 3-12, 3-15 and 3-16 for $E_2' = 0$, $E_3' = 0$ and $z' = 0$, we obtain

$$\begin{aligned} & (n_0^{-2} \cos^2 \theta - r_{13} E_1' \sin \theta \cos^2 \theta + n_e^{-2} \sin^2 \theta - r_{33} E_1' \sin^3 \theta) \\ & - 2r_{51} E_1' \sin \theta \cos^2 \theta x'^2 + (n_0^{-2} - r_{13} E_1' \sin \theta) y'^2 - 2r_{22} E_1' \cos^2 \theta x' y' = 1. \end{aligned} \quad (3-17)$$

The effective refractive index n_{eff} is

$$n_{\text{eff}} = \left(\frac{1}{(n')^2} + r_1 E_1 \right)^{-\frac{1}{2}} \quad (3-18)$$

For the TE-mode the wave is polarized along the x' coordinate.

$$\text{For } n_{\text{eff}} = n' + \Delta n \approx n' - n^3 r' \frac{E_1}{2} \quad (3-19)$$

the refractive index n' and the electro-optic coefficient r' , from Equations 3-17, 3-18 and 3-19, for the TE-mode are

$$n' = \frac{n_0 n_e}{\sqrt{n_e^2 \cos^2 \theta + n_0^2 \sin^2 \theta}} \quad (3-20)$$

$$r' = r_{13} \sin \theta \cos^2 \theta + r_{33} \sin^3 \theta + 2 r_{51} \sin \theta \cos^2 \theta \quad (3-21)$$

For the TM-mode which is polarized along the y' coordinate

$$\begin{aligned} n' &= n_0 \\ r' &= r_{13} \sin \theta \end{aligned} \quad (3-22)$$

The effective electro-optic coefficient in Equation 3-21 is a linear combination of the coefficients r_{ij} and varies with the angle θ . To maximize the effective electro-optic coefficient an optimum value of θ had to be evaluated. For the TE-mode it is given by

$$\theta_{\text{opt}} = \pm \text{arc tan} \sqrt{\frac{r_{13} + 2r_{51}}{2(r_{13} - 2r_{51}) - 3r_{33}}} \quad (3-23)$$

The refraction index of $\text{LiNb}_x\text{Ta}_{1-x}\text{O}_3$ is between that of LiNbO_3 and LiTaO_3 , so that the differences in refractive indices between the waveguide layer and the substrate, should be proportional to the difference of n between LiNbO_3 and LiTaO_3 . From Equations 3-20 and 3-21, we observe that $\theta = 0$ the TE-mode is polarized in direction of the ordinary ray, where the index difference between niobate and tantalate is largest ($\Delta n_0 = 0.113$). But the electro-optic coefficient is zero. For $\theta = 90^\circ$ the TE-mode is polarized in direction of the extra-ordinary ray where the index difference between niobate and tantalate is smallest ($\Delta n_e = 0.021$) but the electro-optic coefficient from Equation 3-21 is $r_{33} = 30 \times 10^{-12} \text{ m/V}$. When the wave propagation is under an angle θ as shown in Figure 3-4, the index differential $\Delta n'$ is such that $\Delta n_e < \Delta n' < \Delta n_0$. Then from Equation 3-21 the angle can be computed which yields the largest electro-optic coefficient r' ; for $\theta_{\text{opt}} = 51^\circ$, $r' = 34 \times 10^{-12} \text{ m/V}$.

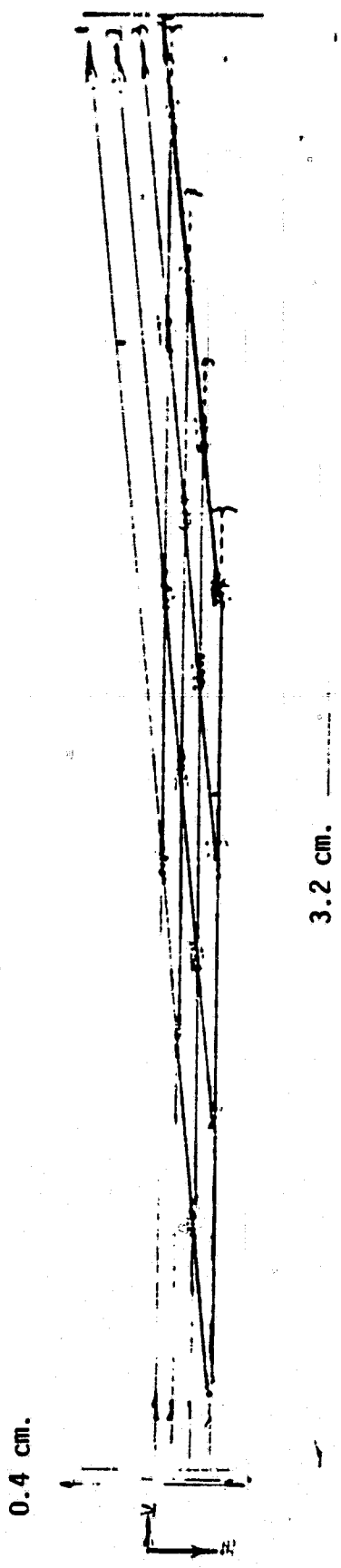
SECTION 4 .
INTEGRATED OPTICS SWITCHING MATRIX USING
ELECTRO-OPTIC, THIN-FILM, BRAGG DIFFRACTION SWITCHES

The requirement for the switching matrix is to connect each of n input ports to each of m output ports. Of primary importance is low cross talk and low distortions.

In principle two different approaches can be taken; the transmission of light between the switches can either be along channel waveguides (2-dimensional wave confinement) or along planar waveguides (1-dimensional confinement). At optical wavelengths 2-d confinement does not necessarily yield the lowest crosstalk, since crosstalk can be set up by leakage inside the switches and by scattering at channel guide junctions. Transmission of light between switches in planar waveguide can introduce crosstalk by coupling between parallel light beams. An optimized switching network must minimize all sources of crosstalk and distortions.

The result of the study on different switching matrix configurations indicates that the switching matrix in Figure 4-1 should yield low crosstalk and small distortions. The switches are electro-optic, Bragg diffraction switches in planar optical waveguide. The entire switching matrix is built on a ferroelectric single crystal substrate, the planar optical waveguide is formed by metal in-diffusion. The SiO_2 buffer layer is coated on the optical waveguide. The interdigital electrodes of the switches are formed by photolithography and lift-off technique. The elongated shape of the single crystal substrate of the switchings matrix in Figure 4-1 can be fabricated from a large single crystal made by the Czochraski pulling technique.

The optical waves along the switching matrix are guided by the planar optical waveguide in the y-direction. In the x-z plane



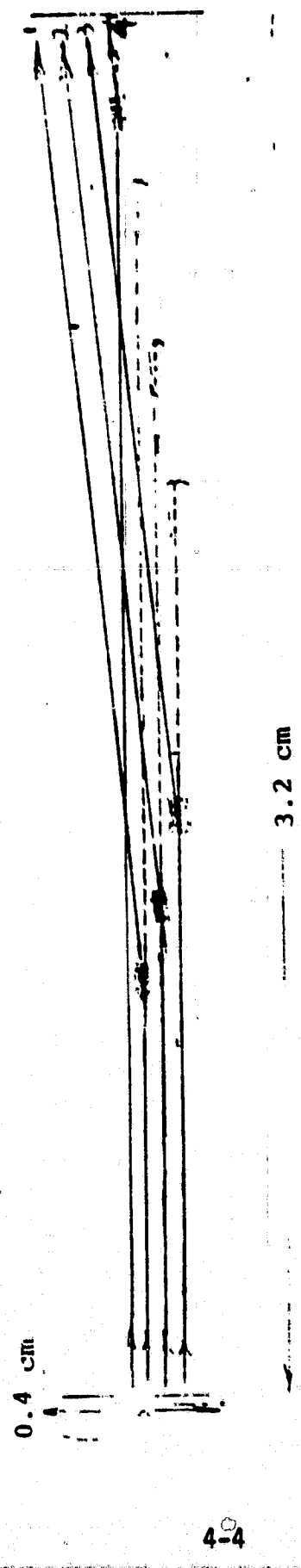
ORIGINAL PAGE IS
OF POOR QUALITY

**Figure 4-1. Integrated Optics Switching 4x4 Matrix
(Using Wider Switches)**

the incident laser beams are collimated by external optics.

A key factor of the switching matrix is that for each connection only one switch needs to be energized. This is shown in Figure 4-2, which gives a cross section through the optical waveguide of the switching matrix. In the "on" position of the electro-optic Bragg diffraction switches, the light entering the voltage induced grating at the Bragg angle θ_B is diffracted through an angle $2\theta_B$ in the plane of the waveguide. In the "off" position when the voltage is removed, the radiation can pass through the switch without leakage or scattering. This is of great importance because of the fact that in the switching matrix for each connection only one switch needs to be energized. Thus, in the 4 X 4 matrix, four switches are energized and 12 switches are in "off" position, as shown in Figure 4-2. The waves can propagate through these 12 switches without experiencing scattering or distortions. An important feature of the switching matrix in Figures 4-1 and 4-2 is that the incident laser beams, after passing through all the switches in each row, are terminated by absorbing films. These terminations are required since in the "on" position, the electro-optic Bragg diffraction switches only deflect about 80 percent of the incident radiation towards the output terminals. The reason for this limitation had been related to the fall-off of the electric field with the distance from the plane of the electrodes. In the switching matrix in Figure 4-1 and 4-2 the part of the incident energy, which in the "on" position, is not diffracted through the angle $2\theta_B$, will continue to propagate in the direction of the incident wave and will be absorbed by the matched termination.

An additional feature of the switching matrix in Figure 4-1 and 4-2 is that it can connect one input port to four output ports. To do so, advantage can be taken that the fraction of the incident light which in the "on" position, is diffracted by the induced phase grating, can be controlled by the voltage across the electrodes. To accomplish equal intensity division among the four output ports, the voltages across the electrodes of the four switches must be staggered, with the lowest voltage at the switch closest to the input port.



4-4

Figure 4-2. Integrated Optics Switching 4x4 Matrix (Using wider switches) Cross Section Through Optical Waveguide

The switching matrix in Figures 4-1 and 4-2 of an $n \times m$ array, is shown for $n=m=4$. The matrix can be extended to an array of 8×16 . One limitation to the size of the array is imposed by the size of the single crystal LiTaO_3 and LiNbO_3 substrate. Taken this as a limitation, the number n and m is restricted by the requirement to minimize coupling between adjacent light beams in the planar waveguide. To evaluate the coupling between adjacent light beams in the optical waveguide, formed by diffusion, the assumption will be made that the field distribution of the coherent light beams, (perpendicular to the plane of the waveguide, (z-direction), is Gaussian, which is given by

$$E \propto E_0 e^{-\frac{z^2}{w_0^2}}$$

$$I \propto I_0 e^{-\frac{2z^2}{w_0^2}}$$

and w_0 is the half-width of the light beam where the field had decayed to e^{-1} . For $z=2w_0$, $E=0.018E_0$ and $I=0.0003I_0$. At a distance of $2w_0$ from the beam center the coherent radiation has decayed by 35 db.

Also the beam expansion has to be evaluated to avoid that the beam widens as it travels from one side of the switching matrix to the other. The Gaussian light beam expands as it propagates over the distance x from a beam width of $2w_0$ to the beam width of $2w$, which are related by

$$w = w_0 \left[1 + \left(\frac{\lambda_0 x}{n\pi w_0^2} \right)^2 \right]^{1/2}$$

For the x- dimension in Figures 4-1 and 4-2, which is $x=3.2 \text{ cm}$, $n = 2.2$ and $\lambda_0 = 0.83 \times 10^{-4}$, the term $\left(\frac{\lambda_0 x}{n\pi w_0^2} \right)^2 \ll 1$ for values of w_0 not

smaller than 0.1 mm. In fact $\left(\frac{\lambda_0 x}{n \pi w_0^2}\right)^2 = 0.147$ for $w_0 = 0.1$ mm.

It follows that a light beam of a Gaussian width of $2w_0 = 0.2$ mm will not expand noticeably as it propagates over a distance of 3.2 cm. When the centers of the light beams are spaced $4w_0 = 0.4$ mm apart, the coupling between them should be no more than 70 db.

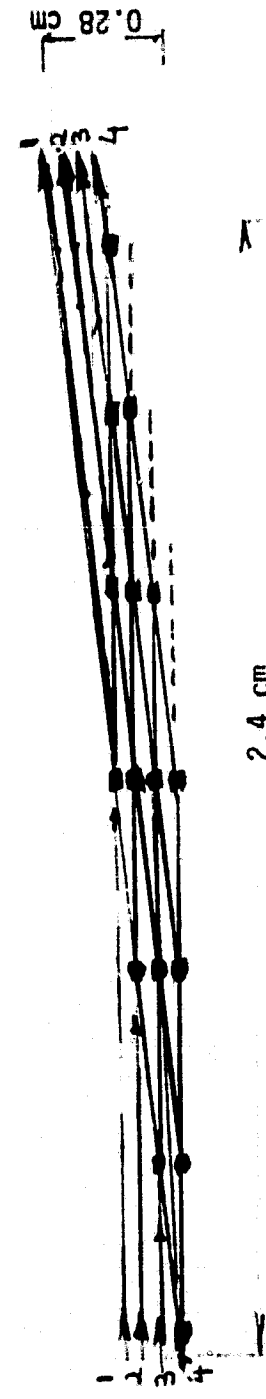
The matrix design in Figures 4-1 and 4-2 use a spacing between the centers of the incoming laser beams of 0.4 mm and a Bragg angle $\theta_B = 2.7^\circ$. The Bragg angle was derived from Eq 3-3 for a periodicity the phase grating of $\Lambda = 4$ microns.

The placement of the Bragg diffraction switches in Figure 4-1 and 4-2 are such that they allow a larger spacing for the deflected beams than for the incident beams.

From Section 3.1.1 it follows that the width of the phase grating can be approximately equal to the width of the incident laser beam if a slight widening of the deflected beam is tolerable. For a grating width of i.e., $w = 0.3$ mm, $Q = 14\pi$ and meets the Bragg effect requirement, that $Q > 10$.

In Figure 4-3 and 4-4, the placement of the switches is such that the spacings among deflected beams is closely the same as that of the incident beams. This design would further limit the width of the phase grating but would reduce the length of the matrix from 3.2 cm to 2.4 cm.

**Figure 4-3. Integrated Optics Switching 4 X 4 Matrix
(Using Narrow Switches)**



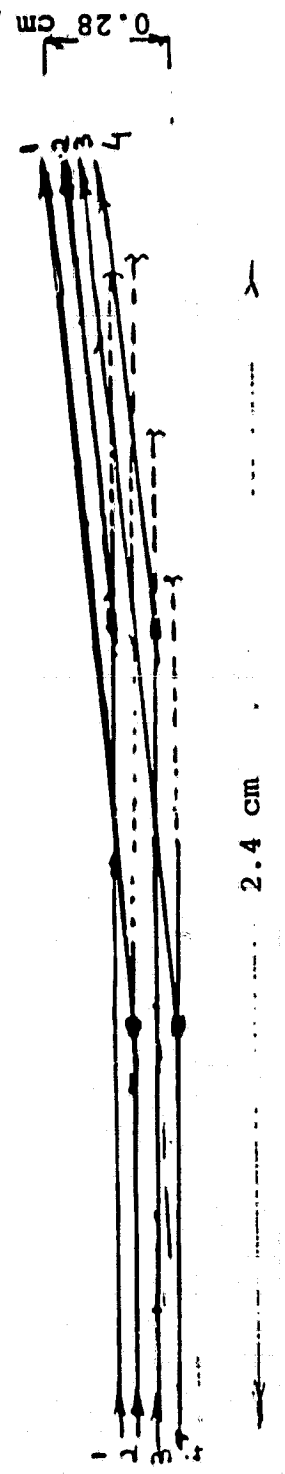


Figure 4-4. Integrated optics switching 4x4 matrix (using narrow switches) Cross section through optical waveguide

SECTION 5

END-FIRE COUPLING USING CYLINDRICAL MICROLENSES

The inputs to the switching matrix are single mode optical fibers which connect the optical transmitters, that is the single transverse mode AlGaAs lasers, to the switching matrix (outlined in Section 3).

The monolithic AlGaAs laser array for use with the optical fibers and the integrated switching matrix is shown schematically in Figure 5-1. The array can be formed by subdividing the p-n junction either by in-diffusion of an isolating material or by mechanical separation. The radiation of the double heterostructure AlGaAs lasers is in general completely polarized, with the optical electric field vector parallel with the plane of the heterolayers. That is, the modes which dominate lasing in the DH structure lasers are TE modes. This polarization is compatible with the polarization of the electro-optic Bragg diffraction switches in the switching matrix, where the TE-mode with the optical electric field vector perpendicular to the y-direction, yields the largest effective electro-optic coefficient r .

The core diameter of the single mode fiber is close to 6 microns. The field distribution across the fiber core can be approximated by a cosine function. For this distribution, the half-power, full-beam width of the radiation from the fiber core is $\theta = 1.1 \frac{\lambda_0}{\text{core diameter}}$ = 8.7° and the full beamwidth to the first nulls in the diffraction pattern, is $1.70 \approx 15^\circ$.

The function of the optical couplers is to transform the radiation from each of the single mode fibers to each of the input terminals of the switching matrix. It is of great importance to couple most of the laser radiation to its respective input. This is not only necessary for power transfer efficiency but also to minimize leakage among input terminals.

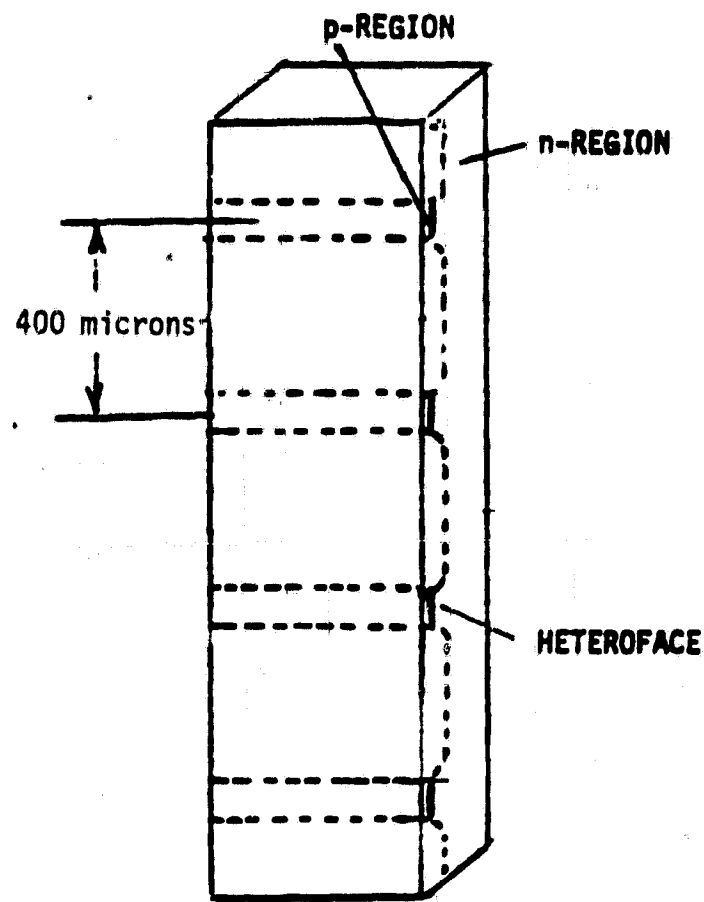


Figure 5.1 AlGaAs Array

The techniques for coupling laser radiation to integrated circuits require either a prism coupler, a grating coupler (Section A-1) or an endfire coupler. Both, the prism coupler and a grating coupler transfer only collimated laser beams efficiently to the integrated circuits and would require a lens to collimate the radiation from the optical fiber. Also, they would take up a sizeable area on the substrate. Butt-edge coupling would not yield the required collimated beam in the x-z plane of the integrated switching matrix. Butt-edge coupling with an integrated cylindrical lens on the substrate seems to be feasible as soon as the quality of integrated lenses will be improved.

At the present time endfire-coupling using three cylindrical microlenses seems to be the most promising approach, especially since previous experiments on the beam transformation of the wide angle radiation from an AlGaAs laser by crossed cylindrical lenses have resulted in a diffraction limited transformed laser beam. Endfire coupling using three microlenses from each optical fiber to each input terminal of the switching matrix would yield the large aspect ratio of the laser beam required for efficient coupling to the switching matrix. This type of endfire coupling would not require any space on the substrate.

5.1 SINGLE TRANSVERSE MODE IN PLANAR OPTICAL WAVEGUIDE (Y-DIRECTION)

In the planar optical waveguide of the switching matrix the laser radiation is guided only in one dimension (y-direction in Figure 3-3 and 3-4.). The metal diffusion into a ferroelectric crystal like LiNbO_3 or LiTaO_3 , to form planar optical waveguide, produce a composition gradient, where the metal mole fraction decreases towards the interior of the crystal. The refractive index decreases from the value at the surface, n_s , to the refractive index of the substrate, n_b . The index profile can be written as $n(y) = n_b + \Delta n f(y/D)$, for $y > 0$. The function $f(y/D)$, called the diffusion shape, describes the variation in the refractive index due to diffusion and takes on values from 0 to 1. This is shown in Figure 5-2 for the LiNbTaO_3

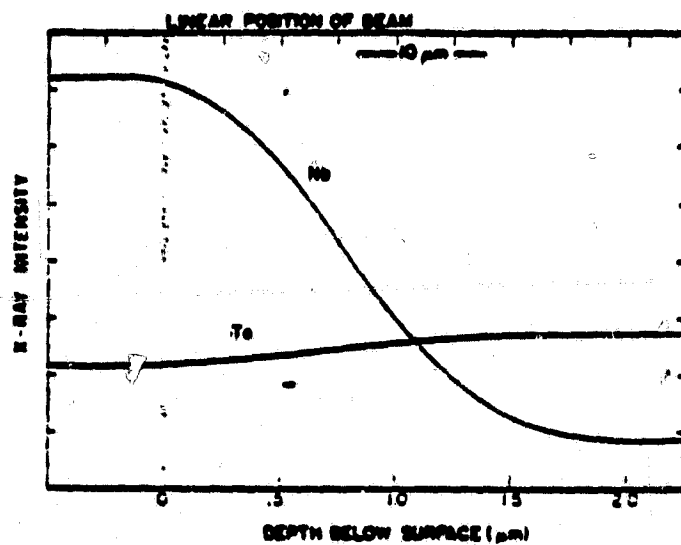


Figure 5.2 Relative Nb and Ta Concentration as a Function of Depth Below the Surface.

(J.M. Hammer and W. Phillips, Appl. Phys. Letters, Vol 24, No. 11, 1 June, 1974)

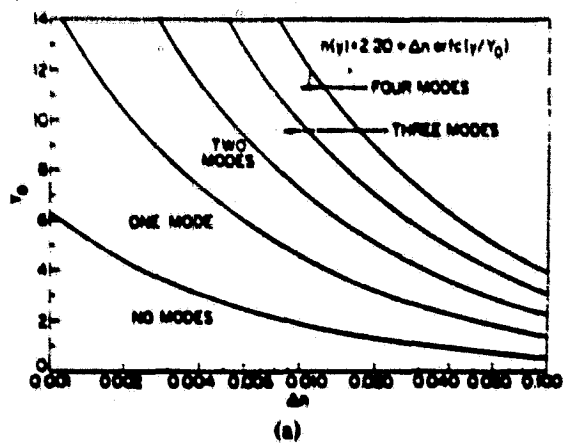
optical waveguide. The diffusion depth D , in general, is normalized over the freespace wavelength λ_0 , $Y_0 = \frac{D}{\lambda_0}$. The diffusion shape follows a complementary error function for short diffusion times, where the metal is not completely diffused into the ferroelectric crystal. For long diffusion times where all the metal is diffused into the crystal, the diffusion shape follows a Gaussian function. (Section 8.1.2.2)

The optical waveguide is asymmetric since $n_b \neq n_0$, where n_b is the refractive index of any layer on top of the waveguide. Thus for propagation of a single mode an upper and lower cut-off can be computed. The results of these computations are given in Figure 5-3. Figure 5-3 shows the single mode cut-off as a function of the difference in refractive index $n_s - n_b$ and the normalized diffusion depth Y_0 . The computation was performed for the diffusion shape being represented by a complementary error function and by a Gaussian function. From Figure 5-3 we conclude that the metal-diffused optical waveguide in a ferroelectric crystal can support the fundamental mode when the normalized diffusion constant is between 1 and 2.2 for the complementary error function, and between 0.5 and 1.7 for the Gaussian function.

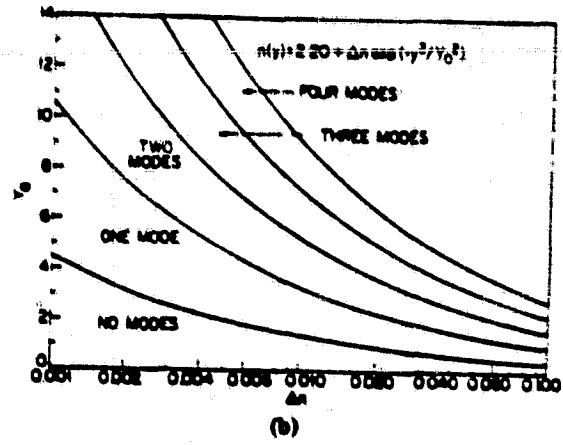
In Figure 5-4, the approximation of the Gaussian field distribution of the single transverse mode for a planar diffused waveguide is shown as a function of the normalized depth $\frac{y}{D}$. For a diffusion depth of approximately 1.3 microns, the Gaussian width of the fundamental mode, $2w_y$, will be approximately 1.8 microns.

5.2 BEAM SHAPE IN THE X-Z PLANE

In the x-z plane of the switching matrix, the laser beams must be parallel beams. To form the parallel laser beams the radiation from the optical single mode fibers must be collimated by the endfire couplers. From Section 4 it follows that the Gaussian width of the laser beams should be $2w_0 = 200$ microns and their center to center spacings 400 microns. The laser beams should not expand noticeably over the length of the switching matrix.



(a)



(b)

Figure 5.3

Index change $\Delta n = n_s - n_b$ versus diffusion depth $Y_0 = D/\lambda$ in units of free-space wavelength, showing the number of waveguide modes. $n_b = 2.20$, and the index profile is as follows. (a) A complementary error function. (b) A Gaussian.

(G.B. Hocker and W.K. Burns, IEEE J Quantum Electronics, Vol. QE-11, No. 6, June 1975.)

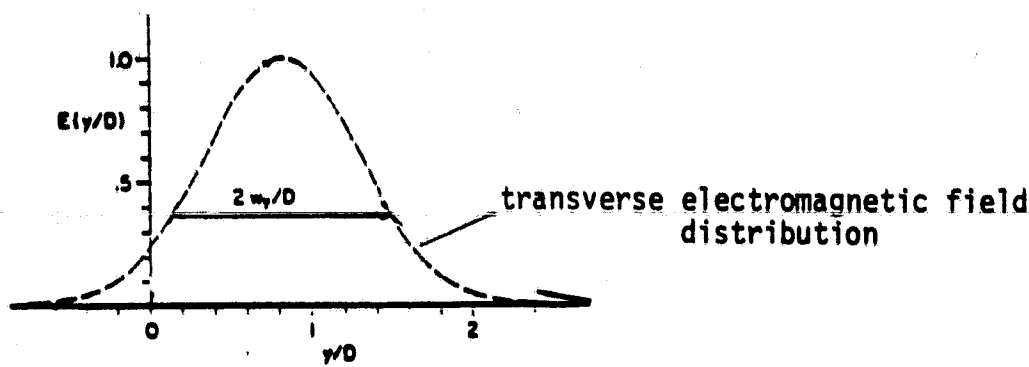


Figure 5.4 Transverse electromagnetic field distribution in a planar diffused waveguide as a function of the normalized depth y/D
 (W.K. Burns and G.B. Hocker, Appl. Optics, Vol. 16, No. 8, August 1977.)

5.3 BEAM TRANSFORMATION

The transformation of the round beam of the single mode fiber to the beam cross-section in the planar optical waveguide of the switching matrix, with a large aspect ratio, requires three cylindrical lenses which are shown in Figure 5-5. In the meridian plane, parallel to the y-direction, the first lens transforms the wide angle optical fiber radiation to a parallel beam, and the second lens transforms the parallel beam to the field of the optical waveguide mode (Figure 5-5a). In the meridian plane parallel to the x-z plane a single lens transforms the radiation from the optical fiber to a parallel beam of 200 microns diameter (Figure 5-5b). The required numerical apertures of the lenses in Figure 5.5a are $\sin \theta_{y1} = 0.13$ for the first lens and $\sin \theta_{y2} = 0.34$ for the second lens. The numerical aperture of the lens in Figure 5.5b is $\sin \theta_{x-z} = 0.13$.

5.4 CYLINDERAL MICROLENSERS

Because of the small dimensions of the switching matrix, the cylindrical lenses must be microlenses. The microlenses can be implemented by the core of optical fibers. When a single fiber core is placed parallel to the mirror faces of the n single mode optical fibers in an array, it can convert the radiations from the optical fibers into n beams, collimated in the y direction. The inverse function can be performed by a second single fiber core when placed parallel to the switching matrix. Silicon technology had been developed previously for precisely positioning the fibers relative to the optical fiber array and to the switching matrix. The collimation of the radiations from the optical fibers in the array in the x-z plane can also be performed by the cores of optical fibers. However, the core diameter of the optical fibers must be larger, also a separate fiber is required for each input terminal of the switching matrix, as shown in Figure 5-6.

In general a lens with a numerical aperture of 0.34 requires at least 3 lens elements to correct for spherical aberrations. However,

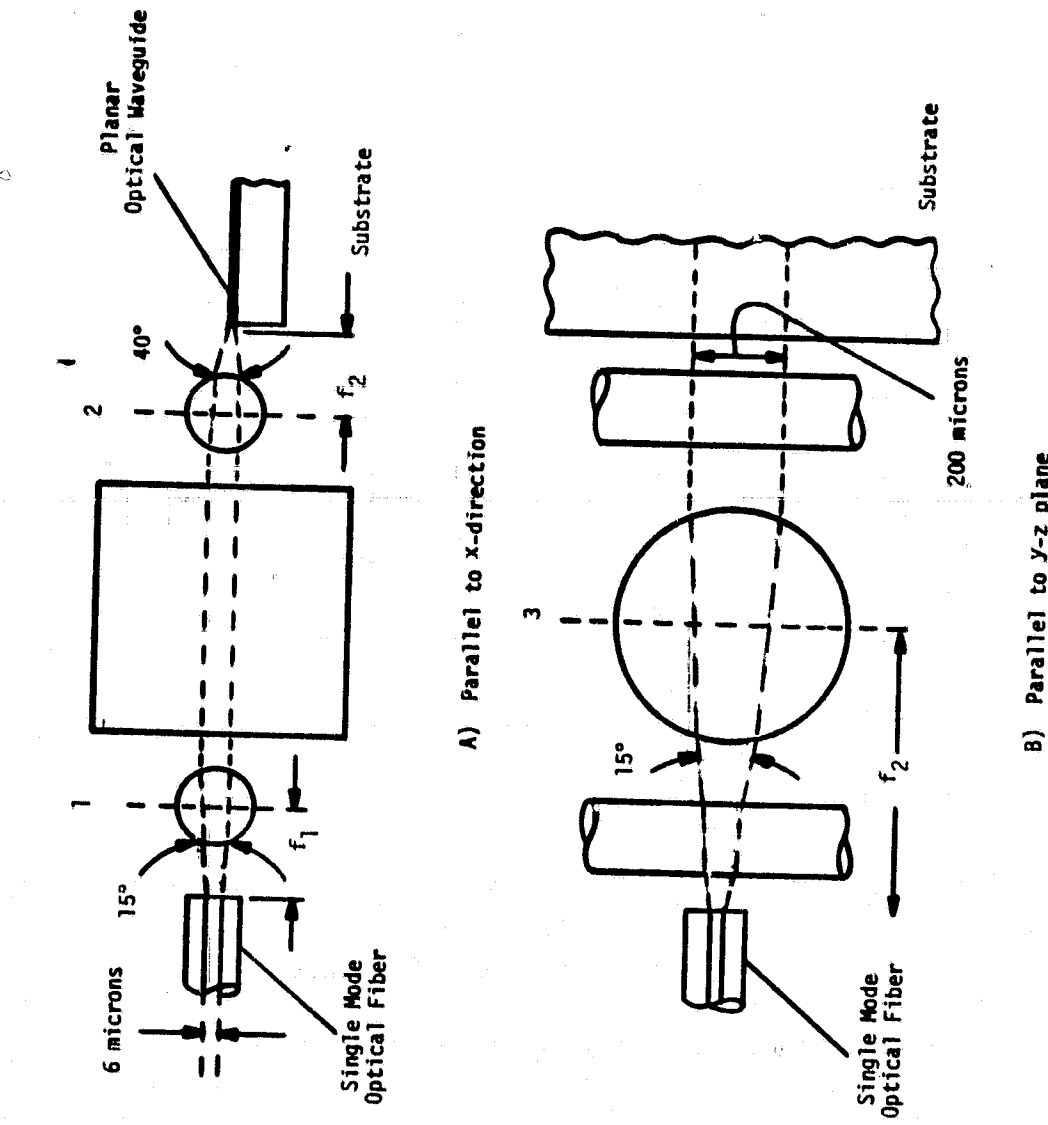


Figure 5-1. Beam Transformation from Optical Fiber to Planar Optical Waveguide

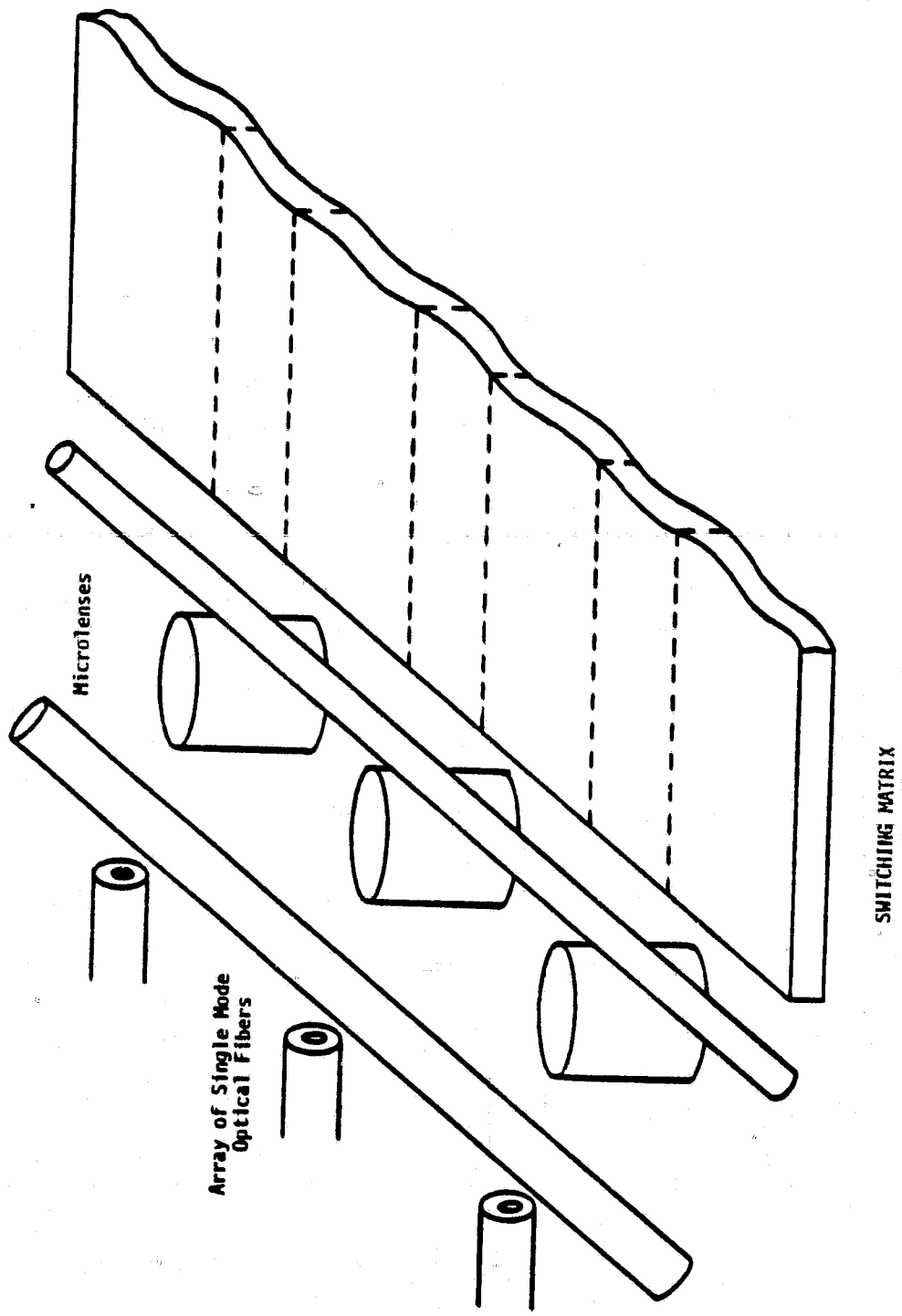


Figure 5-6. Beam transformation from optical fibers to switching matrix

the core of an optical fiber represents a single cylindrical lens so that aberrations will be introduced by the microlenses. To determine whether these aberrations are tolerable the beam transformation through a microlens was evaluated.

The core of an optical fiber is a typical cylindrical microlens. To derive its optical properties it must be treated as a thick lens. In the meridian plane of the lens curvature the focal length f of the core of an optical fiber with constant refractive index n and a circular cross section with the radius R , is given by

$$f = \frac{nR}{2(n-1)} \quad 5-1$$

The two principal planes of the thick lens coalesce at the lens center; the focal planes are at a distance $f-R$ from the vertices of the lens.

In the meridian plane perpendicular to the lens curvature the optical fiber can be considered a dielectric slab. Ray tracing through the dielectric slab shows that the dielectric slab has the effect of forming an "image" of the object with the magnification of one. The image is on the same side of the slab as the object, but the image distance is shorter than the object distance. The displacement of the image from the object (for diverging rays) towards the fiber, is given by

$$\Delta = s + R - \frac{(s-R)\tan \alpha_i + 2R \tan \alpha_t}{\tan \alpha_i} \quad 5-2$$

where s is the object distance, α_i is the angle of the incident ray, and $\sin \alpha_t = \frac{1}{n} \sin \alpha_i$. For small angles of α_i , where $\sin \alpha_i \approx \alpha_i$

$$\Delta = 2R \left(1 - \frac{1}{n}\right) \quad 5-3$$

The first microlens in Figure 5-5a collimates the radiation from the optical fiber (in the y-direction). The second microlens focuses the collimated radiation to couple it to the single-transverse-mode optical waveguide. The optical transformation using two cylindrical lenses, has the advantage that the transformation becomes largely independent of the spacing between the optical fiber and the switching matrix. Also, smaller diameter optical fiber cores can be used than those required for the image formation by a single microlens with object and image spacings close to twice the focal length. This is very important because with increasing fiber core diameter the spherical aberrations become larger.

5.5 TRANSFORMATION IN MERIDIAN PLANE PARALLEL TO Y-DIRECTION

To transform the radiation from the optical fiber array to become parallel, the fiber must be placed close to the focal plane of the first microlens in Figure 5-5a. The transformation properties of a single optical fiber core have been evaluated. Specifically, we have computed the relation between input-output angles, and also the spherical aberrations introduced by the cylindrical microlens, for different angles of incidence and different object distances. The spherical aberrations are expressed as the deviation from a spherical wavefront with a radius approaching infinity. The computation was performed for a fiber core of 180 microns diameter, a refractive index of $n=1.62$ (typical for fused silica) and a focal length of $f=117.5$ microns (from Eq.5-1).

The result is shown in Figure 5-7. As long as the distance between the object and the vertex of the microlens does not exceed 15 microns (corresponding to an object distance of $s = 105$ microns) the microlens forms a virtual image up to a half angle of the incident radiation of 30° . The beam is diverging but the largest half-angle never exceeds 1.5° . As the object moves towards the focal plane ($s=R=27.5$ microns) the divergence of the transformed radiation should approach zero. However, the optical fiber core can not

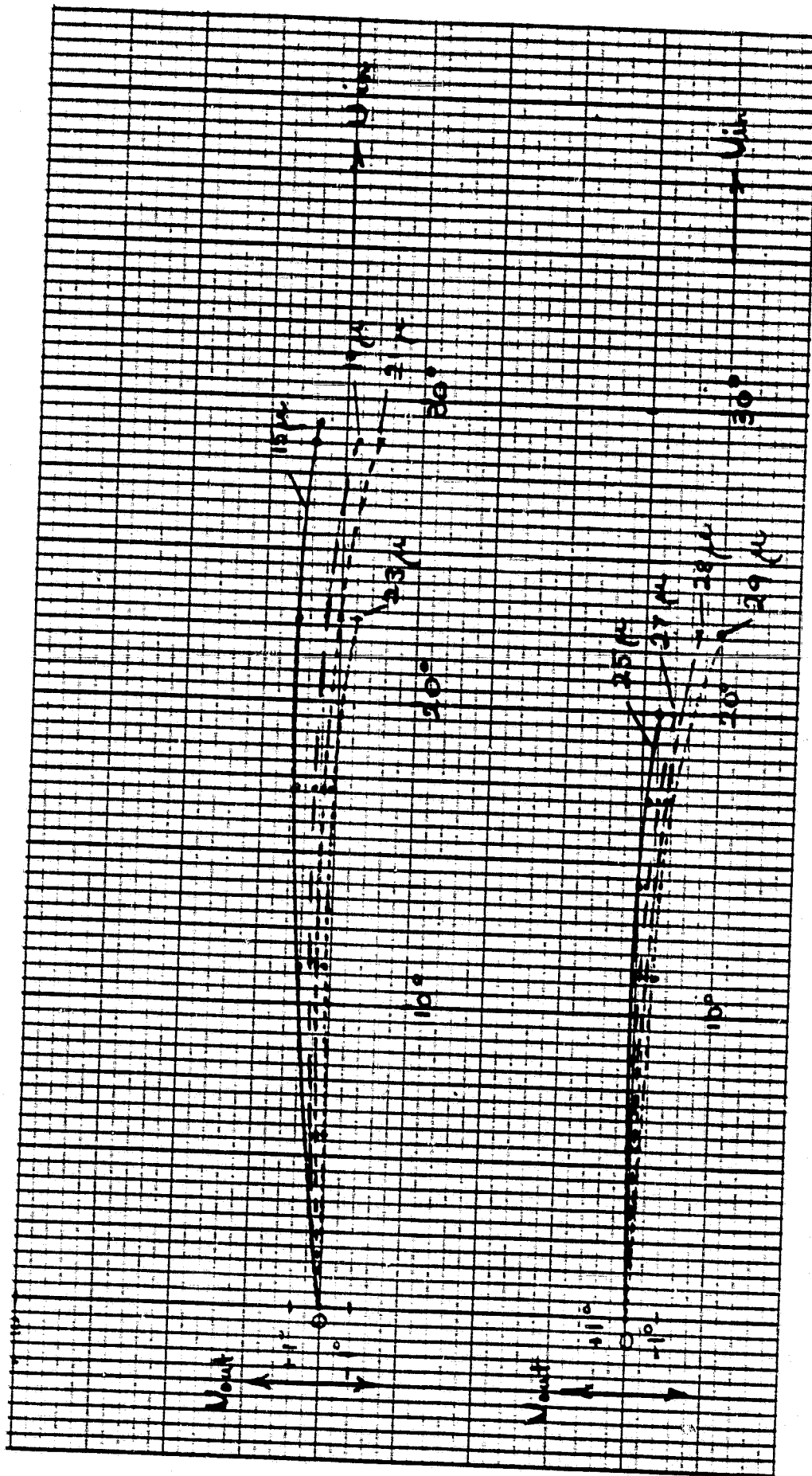


Figure 5-7. Angle transformation by optical fiber core for different spacings $s-R$ between object and vertex of fiber core.

ORIGINAL PAGE IS
PRIOR QUALITY

transform the laser radiation to become parallel (in terms of geometric optics) over the entire half-angle range of 30° . Instead, as the input angle increases the output angle first also increases; then it becomes zero and for even larger angles of incidence the output angle becomes negative. The negative output angles correspond to a real image formation with converging radiation. The change from virtual image to real image formation moves to smaller angles of incidence as the spacing between the optical fiber and the principal plane of the microlens approaches the focal length. For the distances $s-R$ between 25 microns and 27 microns, the output angle is smaller than 0.5° with a half-angle of incidence of 15° and remains 1° at half-angle of incidence of 20° .

The spherical aberrations introduced by the optical fiber core as a function of the half-angle of incidence, is shown in Figure 5-7a, for different spacing $s-R$. In the region of the virtual image formation, where $s-R=15$ microns, the deviation of the actual wavefront from a spherical wavefront is no more than a fourth-wavelength up to half-angle of incidence of 30° . (A deviation of a fourth wavelength can be tolerated). In the region of the real image formation, where $s-R=28$ microns the deviation of the actual wavefront from the spherical wavefront is no more than a fourth wavelength up to a half-angle of incidence of 20° . In the region where virtual and real images are formed ($s-R=23$ microns to 27 microns), the deviation from the spherical wavefront also remains small for half-angles of incidence up to 20° .

For the transformation of the radiation from the optical fiber, in the y-direction, to the optical waveguide mode of the switching matrix, we conclude from Figures 5-7 and 5-7a that the optimum object distance for lens 1 is 113 microns ($s-R=23$ microns). For an object distance of 113 microns the microlens 1 transforms the radiation such that the collimated radiation is practically parallel over the half-angle range of the incident radiation of 7.5° . Also over this angle range the deviation from a spherical wavefront remains way below a quarter wavelength.

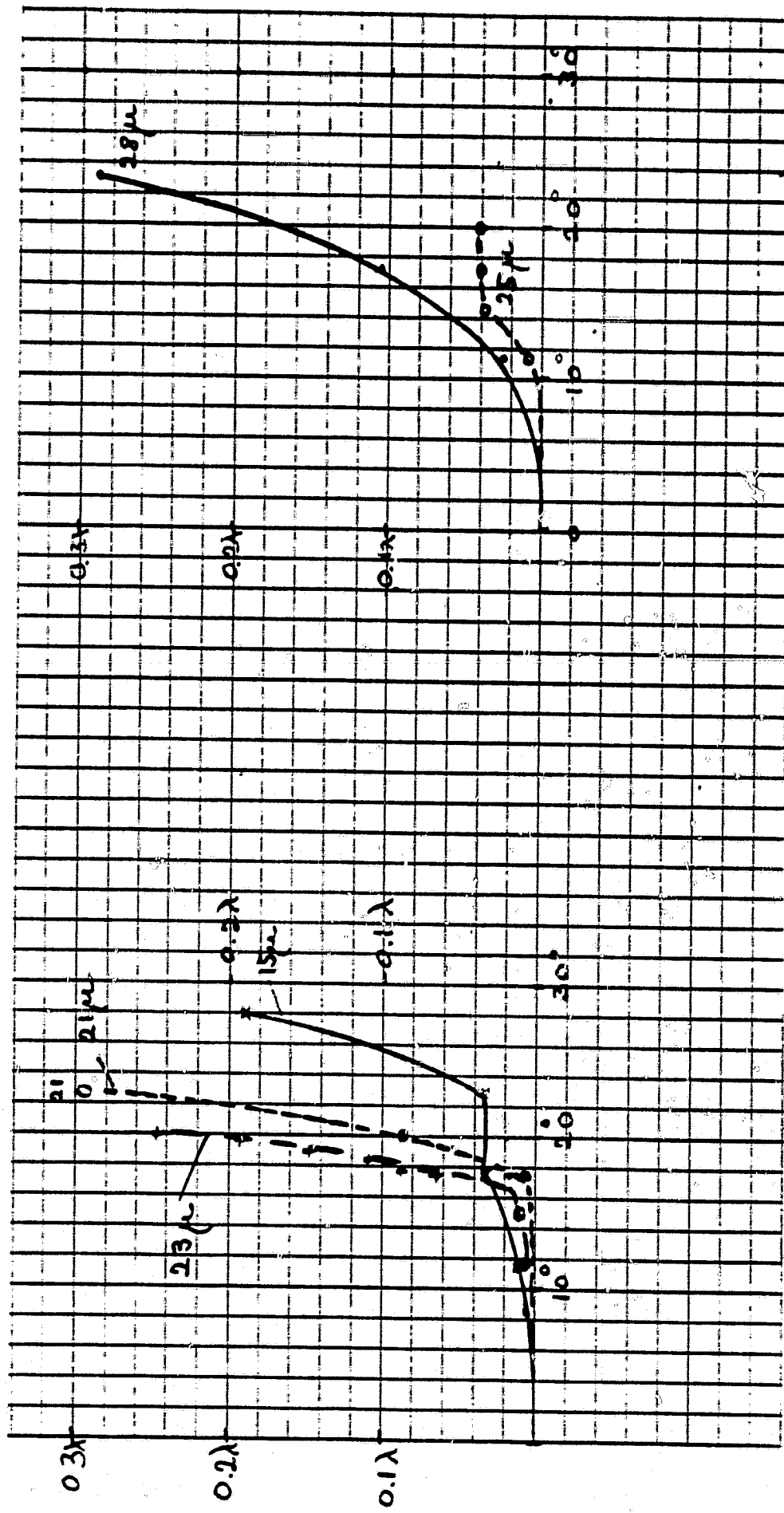


Figure 5-7a. Deviation from spherical wavefront (In fractions of an optical wavelength), for different spacings s-R between object and vertex of optical fiber core.

The micro-lens 2 in Figure 5-5a focuses the collimated radiation to couple it into the optical waveguide of the switching matrix with a Gaussian width of 1.8 microns. The intensity distribution in the focal plane of the microlens is determined by wave diffraction. The Gaussian width $2w_g$ of the laser spot in the focal plane of a lens is

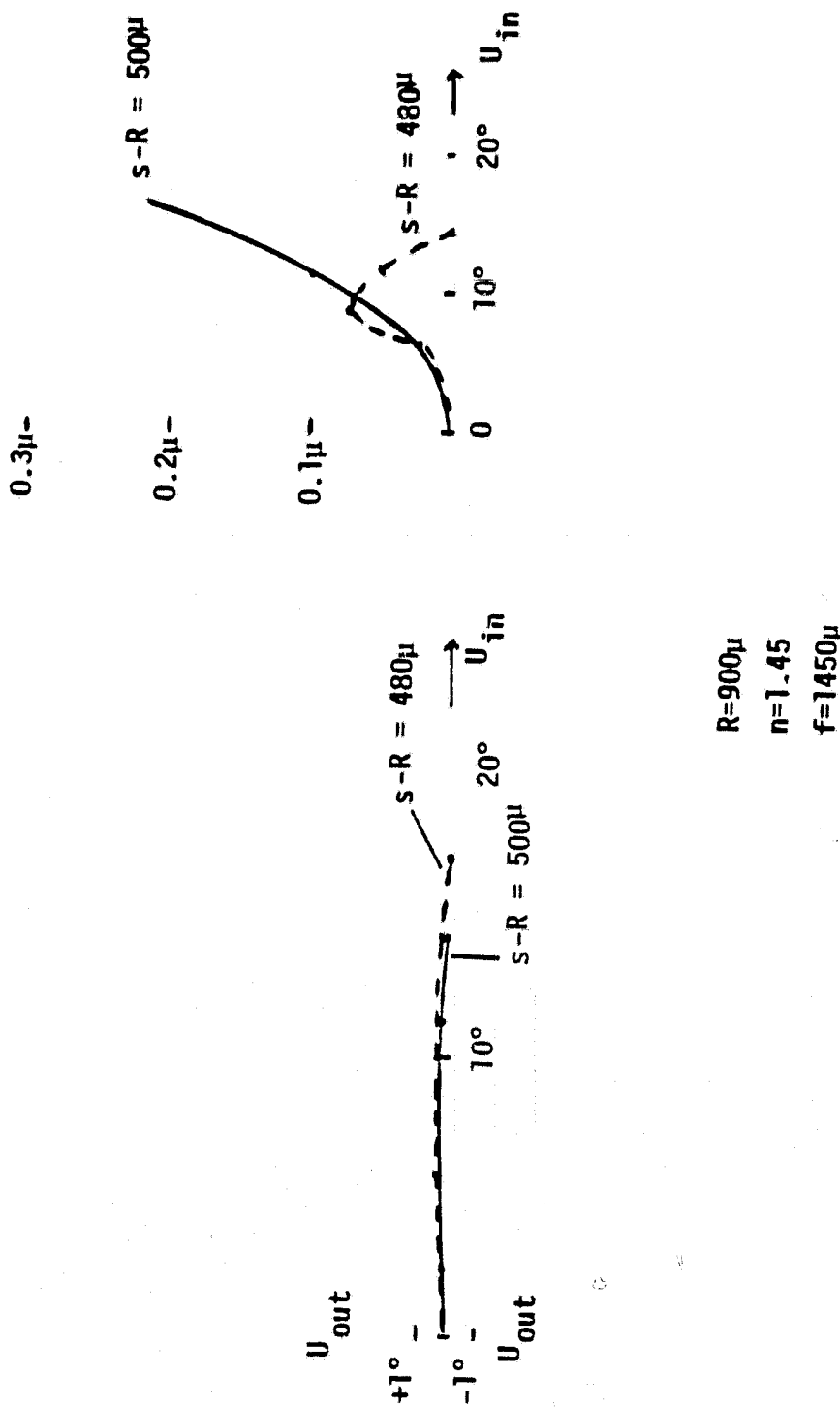
$$2w_g = \frac{3}{\pi} \lambda_o \frac{f}{a} \quad (5-4)$$

where $\frac{a}{f}$ is the numerical aperture of the microlens 2. The numerical aperture of microlens 2 which is $\frac{a}{f} = \sin 20^\circ = 0.342$, yields the Gaussian width of the focused laser radiation in Equation 5-4 to $2w_g = 2.3$ microns. Thus, the Gaussian width of the transformed laser radiation will be rather closely matched to the Gaussian width of the optical waveguide mode of the switching matrix of 1.8 microns.

5.6 TRANSFORMATION IN MERIDIAN PLANE PARALLEL TO X-Z PLANE

In the meridian plane parallel to the x-z plane the radiation from the optical fiber must be collimated to form a beam of 200 microns Gaussian width (Figure 5-5b). To perform this transformation with an optical fiber core its focal length should be 480 microns and its radius should be 300 microns, for a refractive index of $n=1.45$ (Glass)*. No computation on the beam transformation of this type of cylindrical microlens has been performed. To approximate the properties of this type of lens, we show in Figure 5-8, the transformation characteristic of an optical fiber core with a focal length of $f = 1450$ microns, a radius of $R = 900$ microns, and a refractive index of $n = 1.45$, which had been computed previously. The optical transform properties of an optical fiber core with a focal length of

*This type of microlens would require an increase in the beam center spacings on the switching matrix from 0.4mm to 0.6mm, or a Sofloc fiber microlens could be used.



Angle transformation by optical fiber core for different spacings $s-R$ between object and vertex of fiber core.

Deviation from spherical wavefront (In fractions of an optical wavelength) for different spacings $s-R$ between object and vertex of optical fiber.

Figure 5-8.

$f = 480$ microns, will be between those shown in Figures 5-7 and 5-7a, and those in Figure 5-8. The optical fiber core with a focal length of 1450 microns in Figure 5-8 transforms the laser radiation to become very close to be parallel up to a half-angle of incidence of 7.5° (for a spacing between optical fiber and the vertex of the microlens of 480 microns. Also, over this angle range the spherical aberrations are well below a fourth wavelength.

A comparison of Figures 5-7, 5-7a and 5-8 indicates that a smaller focal length cylindrical microlens can transform the fiber radiation to become even closer to be parallel over a half angle range of the incident radiation of 7.5° . We conclude that an optical fiber core with a focal length of 480 microns (microlens 3 in Figure 5-5b) should be able to transform the radiation from the single mode optical fiber with a half angle of 7.5° to become very close to be parallel and to form a beam of 200 microns Gaussian width.

The computation of an optimized spacing $s-R$ for the cylindrical microlens with a focal length of 480 microns will be similar to the computation which resulted in Figures 5-7, 5-7a and 5-8. In designing the optical transformation path parallel to the meridian x-z plane (Figure 5-5b), one has also to consider the effect of microlens 1 on the optical transformation. Microlens 1 forms an image of the p-n junction in the x-z plane. The image formation by the microlens 1 in the x-z plane requires an increase of the optimized spacing $s-R$ of the microlens 3, by Δ , given in Eq. 5-2. It is the image distance of microlens 3 which must be made $s-R$. Since the image distance of lens 3 is smaller by Δ than the distance between fiber and the vertex of lens 3, the vertex of lens 3 must be spaced from the fiber by $s + \Delta - R$. For the parameters of lens 1 where $R = 90$ microns and $n=1.62$, Δ from Equation 5.2 is $\Delta = 69$ microns.

The field distribution at the exit surface of the microlens expands by wave diffraction as the radiation propagates in space. Using the relation for beam expansion (Section 4) the radiation will have expanded by wave diffraction by no more than 14 microns at a distance of 3.2cm.

5.7 END-FIRE COUPLING BETWEEN SECTIONS OF THE SWITCHING MATRIX ON SEPARATE SUBSTRATES

When the physical size of the switching matrix exceeds the size of a single crystal LiNbO_3 or LiTaO_3 substrate, the switching matrix must be subdivided into sections on separate substrates. These sections of the switching matrix must then be combined by optical interconnections. Because of the large aspect ratio of the laser radiation propagating through the switching matrix, the optical connections must also be formed by cylindrical lenses. The schematic of the interconnections is shown in Figure 5-9. In the y-direction where the Gaussian width of the planar optical waveguide mode is 1.8 microns wide, the beam transformation will be similar to the transformation by lens 2 in Figure 5-5a. The transformation of the radiation in the meridian plane parallel to the y-direction between planar optical waveguides will be similar to the end-fire coupling in Figure 5-5a using two microlenses, similar to lens 2 in Figure 5-5b.

In the x-z plane the function of the optical connection is to collimate the slightly expanding laser beam. A single lens with a focal length f , could transform an incoming spherical wave with a radius R_1 to the left of the lens, into a spherical wave-front with the radius R_2 , to the right of it, where

$$\frac{1}{R_2} = \frac{1}{R_1} - \frac{1}{f} \quad (5-4)$$

and R_2 is negative for a converging wave. The radius of the incoming wave is

$$R(x) = x \left[1 + \left(\frac{\pi w_0^2 n}{\lambda_0 x} \right)^2 \right] \quad (5-5)$$

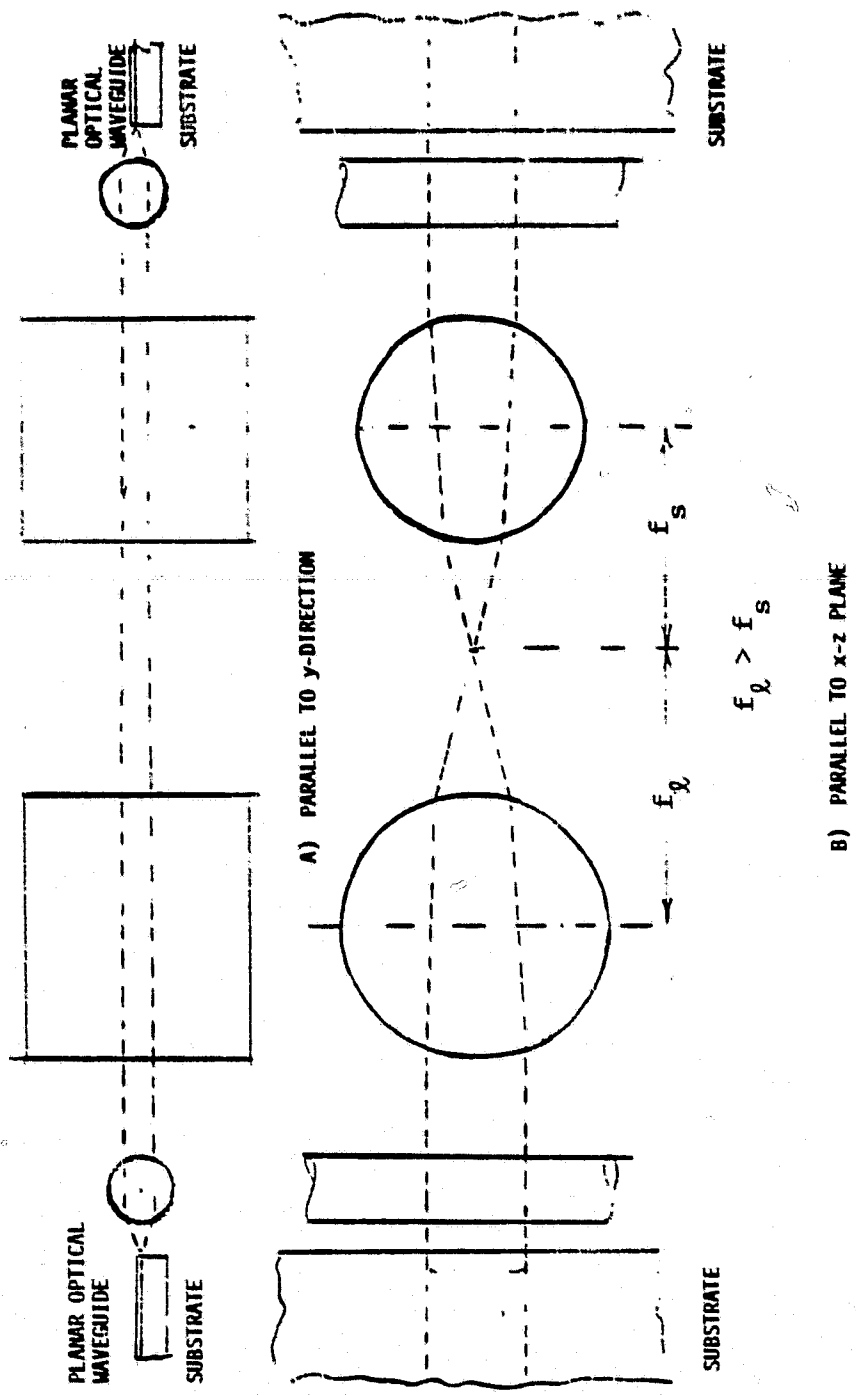


Figure 5-9. Optical connection between sections of switching network.

For $w_0 = 100$ microns and $x=3.2\text{cm}$, $R=15.3\text{cm}$. From Equation 5-5 it follows that a cylindrical lens with a large focal length would be required to collimate the expanding laser radiation.

The collimation of the slightly expanding laser beam in the $x-z$ plane can also be performed by the two microlenses in Figure 5-9b. The two microlenses can be implemented by similar optical fiber cores, as were described in Section 5.6 for end-fire coupling the fiber to the switching matrix in Figure 5-5b. To collimate the slightly expanding beam the focal length of the second lens in Figure 5-9b must be slightly smaller than the focal length of the first lens.

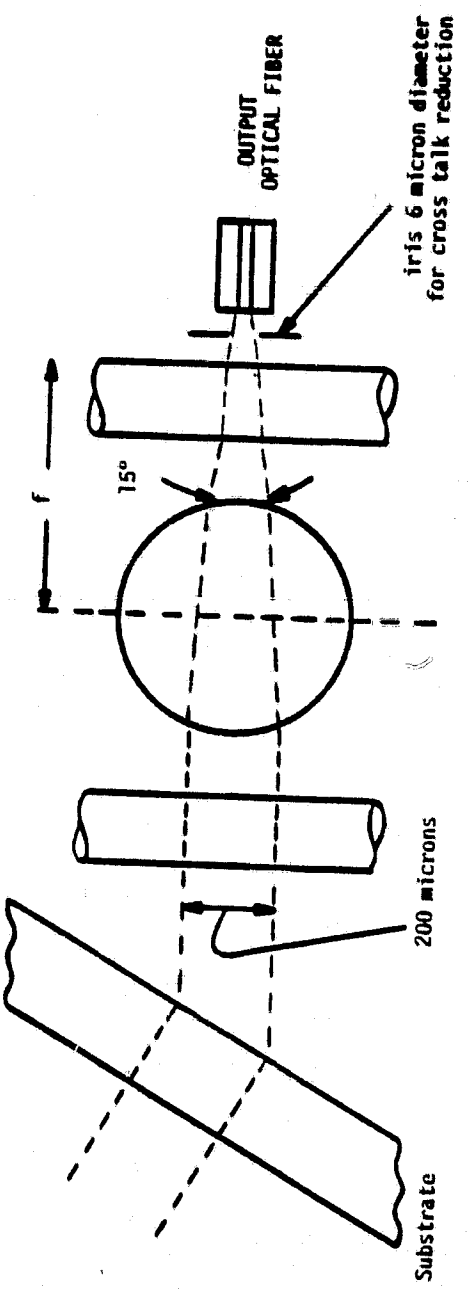
SECTION 6

CROSS TALK REDUCTION

To reduce the cross talk between the collimated laser beams of the switching matrix, advantage can be taken of a property of lenses derived from wave diffraction theory. Eq. 5-4 defines the Gaussian width of the laser spot in the focal plane of a lens. However, this equation is valid only for spatially coherent waves. Waves which are not spatially coherent will form a wider laser spot. Waves which enter the lens off-axis or under a different angle than the wave deflected to this terminal, will form a laser spot off the optical axis of the lens. An iris (Figure 6-1) in the focal plane of the lens at the output coupler of the switching network, along the optical axis, with a diameter of

$$2 w_g = \frac{3}{\pi} \frac{\lambda_{of}}{a} = 6 \text{ microns}$$

(where $\frac{a}{f}$ is the numerical aperture of the lens) will reject all interfering waves and should greatly reduce cross talk.



Parallel to x-z plane

Figure 6-1. Cross Talk Reduction

SECTION 7

P-N JUNCTION LASER

7.1 INTRODUCTION

Semiconductor p-n junction lasers, because of their small size and high gain, are uniquely suited as sources in integrated optical systems. Of these lasers the AlGaAs laser is the best developed, and consequently, we will begin our discussion based upon the properties of this device for use with single transverse mode optical switches, and low-loss single-mode fibers. The light source not only needs small size and high gain, but for compatibility with integrated optic switches the laser must oscillate in a single transverse mode. Furthermore, the laser design should be such that the laser oscillation can be coupled efficiently to a single mode optical fiber.

"Buried" heterostructure AlGaAs lasers were the first to operate reproducably in a single transverse mode. However their small junction width, which made the single mode radiation possible, also limits the optical CW power at room temperature to close to 1 mW. Recently a transverse mode stabilized AlGaAs injection laser with a channeled-substrate-planar structure had been reported with CW power at room temperature up to 10 mW. This device is commercially available.

7.2 DOUBLE HETEROSTRUCTURE LASER

7.2.1 Structure

The transition from GaAs injection lasers operating efficiently at liquid nitrogen temperature to CW injection lasers operating efficiently at room temperature, required close confinement of the injected carriers as well as confinement of the optical field close to the active region of the laser. Both was accomplished by epitaxial growth of a double heterostructure laser, where the active region formed of $Al_aGa_{1-a}As$ is sandwiched between two layers of $Al_xGa_{1-x}As$. In the DHS laser at room

temperature $0 \leq a \leq 0.1$ and $x > a$. Carrier confinement to the active region is attained by the higher bandgap energy of the confining $\text{Al}_x\text{Ga}_{1-x}\text{As}$ layers. The optical field confinement results from the higher refractive index of the active $\text{Al}_a\text{Ga}_{1-a}\text{As}$ layer at the center of the structure.

The DHS AlGaAs laser has a stable structure because of the close match in the lattice parameters of $\text{Al}_a\text{Ga}_{1-a}\text{As}$ and $\text{Al}_x\text{Ga}_{1-x}\text{As}$.

A typical double heterostructure is shown in Figure 7-1. The n-type $\text{Al}_x\text{Ga}_{1-x}\text{As}$ layer is grown on a n-type GaAs substrate. The second layer is the active layer of p-type $\text{Al}_a\text{Ga}_{1-a}\text{As}$, and the third layer is p-type $\text{Al}_y\text{Ga}_{1-y}\text{As}$, where $y \approx x$. A fourth layer of p-type GaAs is added for contacting purposes.

The optical field distributions inside the DHS laser is that of the fundamental mode of a dielectric waveguide. The mode is guided by the active layer which has a higher refractive index than the adjacent layers. For instance, the difference of the refractive indices of the active $\text{Al}_a\text{Ga}_{1-a}\text{As}$ layer and the adjacent $\text{Al}_x\text{Ga}_{1-x}$ layers for $x = 0.3$ is close to 5 percent. The extent of the optical field of the dielectric waveguide mode into the adjacent layers is largely determined by the thickness of the active regions. When the thickness of the active layer is more than 0.5 microns the fraction of the optical energy confined to the active layer is close to 90 percent. However, the fraction of the optical energy confined to the active region decreases rapidly when the thickness of the active layer becomes comparable to the lasing wavelength in GaAs of 0.25 microns. But the carrier confinement to the active layer produced by the potential barriers introduced by the higher bandgap of the $\text{Al}_x\text{Ga}_{1-x}\text{As}$ layers still holds even when the active layer is thinner than 0.25 microns. The characteristics of the different types of AlGaAs lasers had been introduced primarily by changing the thickness of the active layer and with it, by changing the distribution of the optical field.

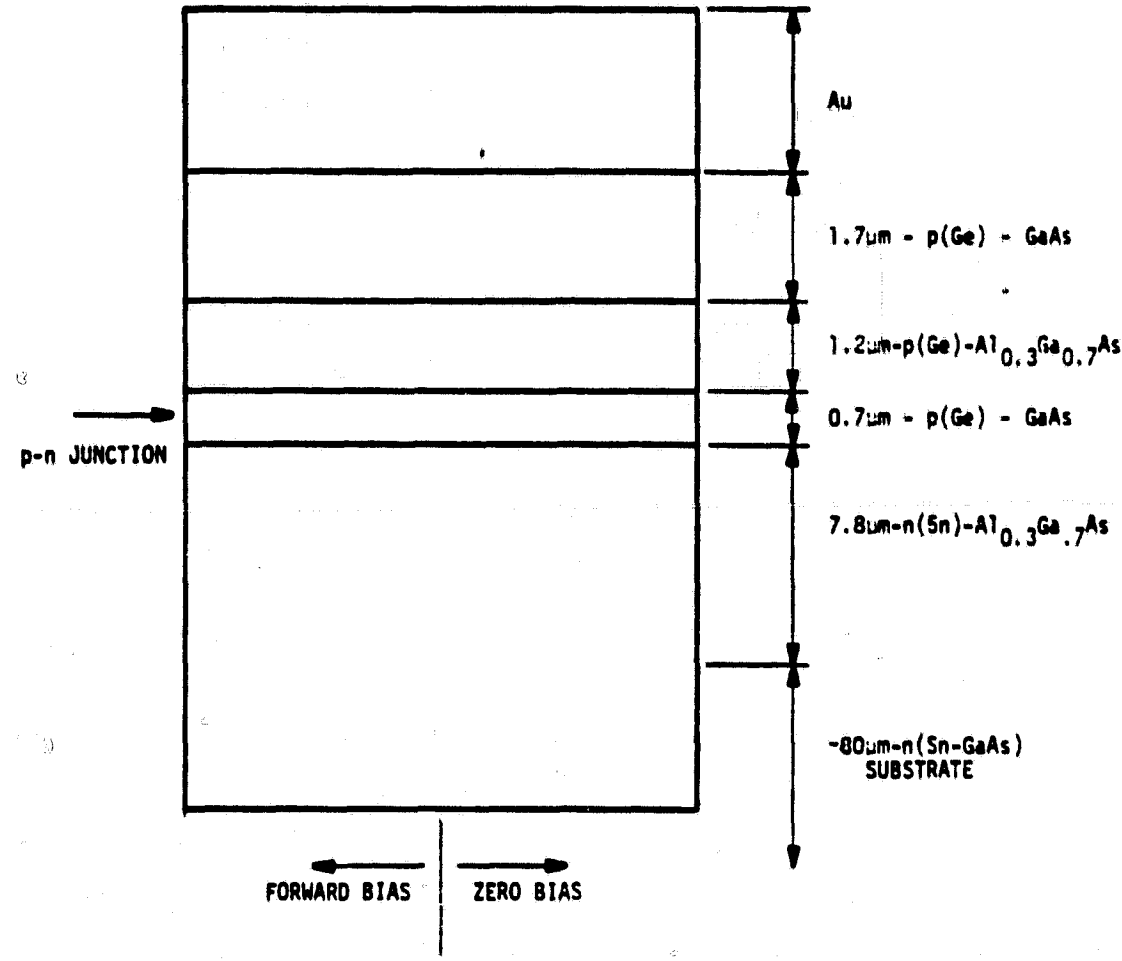


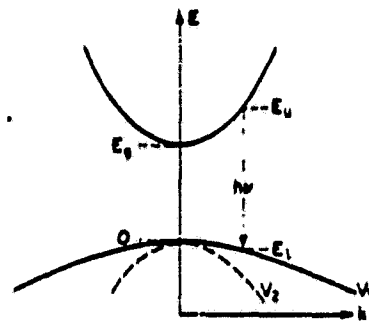
Figure 7-1. Structure of DH diode laser with p-type active layer [n-p-p) DH structure].

7.2.2 Operation Wavelength

The photon energy of the stimulated emission of the DHS laser is close to the energy gap of the $\text{Al}_a\text{Ga}_{1-a}\text{As}$ in the active layer. For $a = 0$, the wavelength at room temperature is around 9000\AA . For $a > 0$ the higher energy gap of AlGaAs moves the wavelength of the laser radiation to lower values. However, the mole fraction of AlAs is limited to $a = 0.34$, where, at room temperature, the direct band-to-band radiative transition changes to indirect radiative transitions as shown in Figure 7-2. The transition probability is much higher for direct transition than for indirect transition, a mole fraction of AlAs corresponding to $a > 0.34$, would seriously decrease the efficiency of the laser. The cross-over between direct and indirect transition at room temperature with $a = 0.34$ corresponds to an energy of 1.92 volts, and to a wavelength of 6600\AA , as shown in Figure 7-3. For a mole fraction of AlAs of no more than 10 percent, corresponding to a wavelength shift from 9000\AA to 8000\AA , the threshold current density and the external quantum efficiency are nearly equal to the equivalent values of injection lasers, having a GaAs active region. An increase of the mole fraction from $a = 0.1$ to larger values, results in noticeable increase in threshold current and a decrease in quantum efficiency. The shortest wavelength from an AlGaAs laser for $a = 0.37$ was measured at 77°K to be 6192\AA .

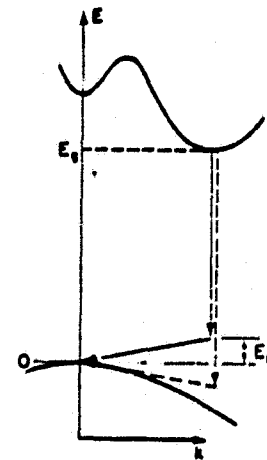
7.2.3 Stable Transverse Mode Radiation With up to 10 Microns Junction Width

From the theory of gain-induced guiding in the AlGaAs laser, the channeled-substrate-planar DHS laser has been developed which radiates in the fundamental TEM_{00} mode up to twice the threshold current, where the CW power at room temperature is close to 10 mW. In the AlGaAs laser where the Fabry-Perot resonator is completely filled with the high gain medium, the modes are determined by the refractive index and gain variations of the medium. In the direction normal to the p-n junction the optical field of the DHS, due to the small height of the active layer, will always be in the fundamental mode. Along the junction the



(a)

Direct band-to-band radiative transition.



(b)

Radiative indirect transition.

Figure 7-2

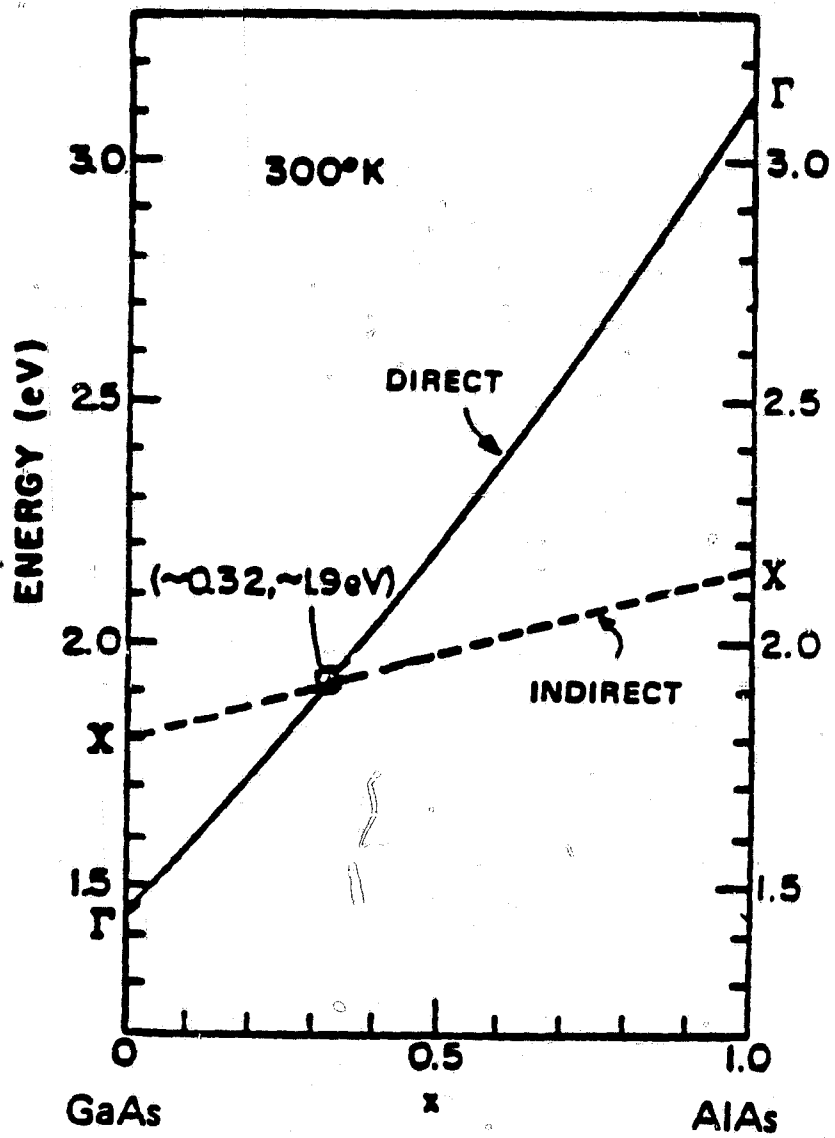


Figure 7-3. Mole Fraction AlAs.

dominant factor in selecting the lowest order transverse mode, is the gain-guiding mechanism.

The gain-guiding mechanism is an extension of the mode selection in a dielectric waveguide when the refractive index is complex. In a dielectric waveguide with real refractive index the wave is guided by the real part of the refractive index which is higher in the center region. In the DHS lasers the mode normal to the junction plane is that of a dielectric waveguide where the real part of the refractive index of the active $Al_xGa_{1-x}As$ layer is higher than that of the adjacent $Al_xGa_{1-x}As$ layers, since $a < x$. Because of the small thickness of the active layer the optical field normal to the junction plane is in the lowest order transverse mode.

For the analysis of gain-induced guiding along the junction the assumptions have been made that the complex dielectric constant is spatially parabolic, it can be written as

$$\epsilon(x) = \epsilon_0 - a^2 x^2 \quad (7-1)$$

where ϵ_0 is the complex dielectric constant on the z-axis, (where $x = 0$), and the x-direction is along the junction. Also, the lowest order modal electric field, near threshold, is given by

$$E(x, z) \propto \exp [-1/2 kax^2] \exp [-j\beta z] \quad (7-2)$$

where $k = \frac{2\pi}{\lambda}$, considering only the component along the junction $E(x)$, and the component along the direction of propagation $E(z)$. In the high gain medium the propagation constant β and the factor a in Eqs. 7-1 and 7-2 are both complex. From the relation between these parameters and the complex refractive index $n(x) = \sqrt{\epsilon(x)}$, the complex term $a = a_r + ja_i$ has been calculated. Along the junction where the real part of the refractive index does not vary, guiding of the fundamental mode must be provided by the spatial gain variation. From Eq. 7-2 the half width w_x (where the field equals e^{-1}) of the Gaussian mode, guided by the gain

variation, can be defined as

$$1/2 k a_f = 1/w_x^2$$

and

$$w_x^2 = S (2/3 \lambda \bar{n} g'')^{1/2} \quad (7-3)$$

where S is the width of the pumped region in Figure 7-4, and

$$g'' = g - \alpha + \alpha_2$$

where g is the gain in the active region, $g - \alpha$ is the gain above threshold as shown in Figure 7-4 and α_2 is the loss in the adjacent unpumped region. To define the equivalence between gain induced guiding and guiding in a dielectric waveguide having a real refractive index, the mode width w_d is derived from Eq. 7-2 where the gain term $a_f = 0$. This derivation gives

$$1/2 k a_n = 1/w_d^2$$
$$w_d^2 = (\lambda S/2 \sqrt{3 \pi n}) (\Delta n_1/\bar{n})^{-1/2} \quad (7-4)$$

where Δn_1 is the increase of the real part of the refractive index of the center region over that of the outer regions, in the equivalent dielectric waveguide shown in Figure 7-4. From Eqs. 7-3 and 7-4 it follows that the gain g'' that gives the same confinement of a Gaussian mode as an incremental refractive index Δn_1 does, is given by $g'' = \frac{8\pi}{\lambda} \Delta n_1$. (7-5)

The parabolic gain distribution having its maximum at the junction center, can occur only near threshold. At higher injection currents the stimulated emission depletes the gain. The depletion is most effective at the center of the junction where the Gaussian mode has its maximum.

For transverse mode stability along the junction, the gain-induced guiding mechanism must be stronger than the mode deformation by gain depletion. The structure of the channeled-substrate-planar (CSP) laser which accomplishes this, is shown schematically in Figure 7-5. The spatial variation of gain and loss along the junction, required for stable transverse mode guiding, is accomplished by introducing losses at the regions outside of $\pm S/2$. In the CSP laser, the active region is only

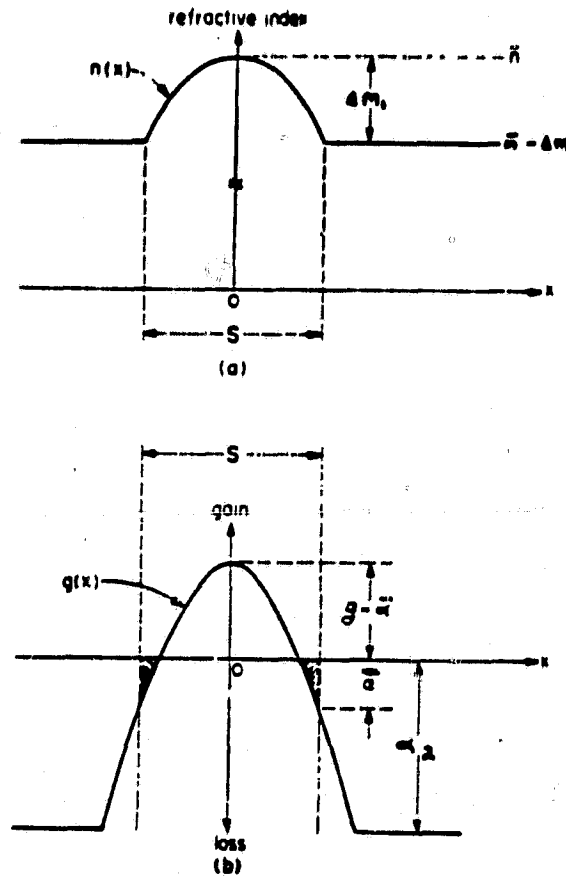


Figure 7-4. A) Schematic of real refractive-index profile.
 B) Schematic of spatial gain profile.

(D.D. Cook and F.R. Nash, J. Appl. Physics.
 Vol. 46, No. 4, April 1975, p. 1660.)

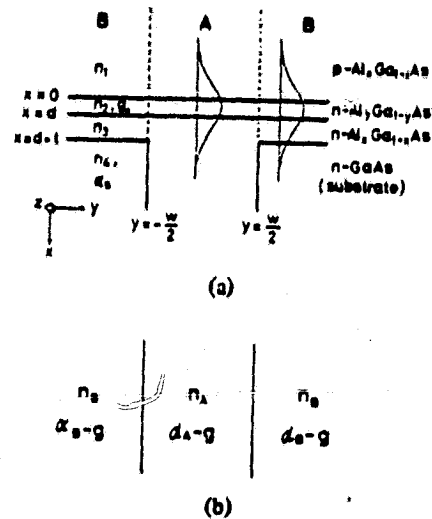


Figure 7-5.

A) Schematic cross section of the Channeled-Substrate Planar (CSP) laser. B) An equivalent slab-waveguide used in the analysis. Uniform gain g_0 was assumed in the active layer.

(K. Aiki, et al., J. Quantum Electronics, Vol QE 14, Feb. 1978, p. 89)

0.1 micron thick so that the optical field (normal to the junction) extends far into the adjacent confining $Al_xGa_{1-x}As$ layers. One of these layers, the n-type $Al_xGa_{1-x}As$ layer, does not have uniform thickness along the junction. This layer is thicker over the junction width S , and only 0.3 micron thick outside $\pm S/2$. The optical field over the junction width S is well confined and subjected only to low losses in the $Al_xGa_{1-x}As$ layer with its higher energy gap. Outside the junction width S , the optical field penetrates into the n-type GaAs substrate. Due to the lower energy gap of GaAs it causes high optical loss.

The test results of the CSP laser show that the transverse mode control by gain-loss guidance can be accomplished up to about twice the threshold current. The CW power at room temperature is about 10 mW; the threshold current 40-90 mA. The radiation is a stable TEM_{00} - mode. The modulation characteristic is linear and does not show any "kinks."

7.2.4 High Bit Rate PCM Modulation of DH-AlGaAs Lasers

Though the direct modulation of p-n junction lasers is a most efficient modulation method, the inherent properties of the laser can introduce distortions at very high bit rates. The properties which can adversely affect the modulation characteristics are: a) time delay between the leading edge of the injection current pulse and the onset of stimulated emission, b) excitation of a damped oscillation caused by a resonance-like phenomena, and c) radiative recombination time in the range of several nano-seconds.

The most direct method to impress information on the light output of an injection laser, is to amplitude modulate the light by varying the strength of the laser excitation. This type of modulation lends itself well to analog modulation. The optical power varies proportional to the injection current, once the threshold current is exceeded. And the photodetector current varies proportionally to the optical power. Thus, there is a linear relationship between injection current and photodiode current. To take advantage of the linear modulation characteristic, the injection laser has to be biased with a constant pumping current, to the middle of the linear

modulation range. This bias current requirement makes analog modulation inefficient.

The more efficient modulation for injection lasers is the pulse modulation of the excitation. However, the modulation rate can not exceed an upper limit which is given by the time delay between the leading edge of the injection current pulse and the onset of stimulated emission. This "turn-on" time is required for the buildup of the electron density to the level required to overcome the losses in the laser. In double heterostructure lasers operating at room temperature a delay of the order of several nanoseconds is typical, giving a theoretical upper limit of modulation rate of 100 MHz.

The lasing delay time which is proportional to the spontaneous lifetime τ_s can be reduced by the superposition of a d-c bias current which is close to or slightly above the threshold injection current. Modulation rates up to 1 GHz have been reported when operating with a d-c bias current equal to the threshold current.

At the upper frequency limit, short pulses are distorted and longer pulses are ringing. These effects are introduced by the spiking fluctuations, a resonance phenomena of the laser itself. The spiking fluctuations are damped oscillations, which result from the dynamic instability in the interaction between the inverted electron population and the optical field in the laser. The response of the injection laser to a sudden current increase is an increase in photon density which rapidly depletes the inverted electron population. This results in a reduction of the optical field until the inverted electron density can be rebuilt by the injection current. Consequently, a damped oscillation between photodensity and inverted electron density is set up, until equilibrium is established with the new operating condition.

The spiking resonance frequency depends on the photon life time $\tau_{\text{stimulated}}$, the spontaneous life time $\tau_{\text{spontaneous}}$, and the ratio of the drive current to the threshold current. The spiking resonance is an inherent

property of the injection laser and can only be changed by varying the injection current. However, in the CW laser the injection current can only be varied over a small range. The resonance-like phenomenon occurs at frequencies of 1GHz or higher. A low pass filter amplifier with a bandwidth of 500 MHz can reduce the effect of the damped oscillation on the PCM modulation.

For a high bit rate PCM modulation, a radiative recombination lifetime of a few nanoseconds of the AlGaAs laser causes the initial condition of the carrier density at each bit to vary depending on whether the preceding bit was a 1 or a 0. For high bit rate PCM modulation the recombination lifetime must be reduced; this can be accomplished by driving the laser with an injection current well above the threshold current.

In a laser the total number of transitions per unit time from the higher energy state to the lower energy state, is

$$N_{kl} = N_\ell \left[B_{kl} \bar{\rho}(v_{kl}) + A_{kl} \right] \quad (7-6)$$

where N_ℓ is the total number of carriers in the higher energy state, B_{kl} is Einstein's coefficient of induced emission, A_{kl} is Einstein's coefficient of spontaneous emission and $\bar{\rho}(v_{kl})$ is the time average of the energy density of the electromagnetic-radiation at the frequency v_{kl} . The frequency

$$v_{kl} = \frac{E_\ell - E_k}{h} ,$$

where E_ℓ and E_k are the energies of the higher and lower quantum states. The energy density $\bar{\rho}(v_{kl})$ can be specified by the average number of photons \bar{n} per mode;

$$\bar{\rho}(v_{kl}) = \frac{8\pi h v_{kl}^3}{c^3} \bar{n}$$

where h is the Plank's constant and $c = 3 \times 10^{10}$ cm/s. From the definition of the Einstein's coefficients follows that

$$\frac{A}{B} = \frac{8\pi\hbar\nu^3}{c^3} \quad (7-7)$$

The transition rate from the higher to the lower energy states from Eq. 7-6 is

$$R_{kl} = B_{kl}\bar{\rho}(\nu_{kl}) + A_{kl} \quad (7-8)$$

While the transition rate for spontaneous emission in Eq. 7-9 is independent of the energy density of the electromagnetic radiation, the transition rate for induced emission is proportional to the energy density $\bar{\rho}(\nu_{kl})$.

From Eqs. 7-7, 7-8 and 7-9 follows that the ratio of the induced transition rate to the rate of the spontaneous emission into a given mode, is equal to the number of quanta \bar{n} in the mode.

Since $R_{kl} = \frac{1}{\tau}$, where τ is the radiative recombination time of the AlGaAs laser, Eq. 7-9 becomes

$$\frac{1}{\tau} = \frac{1}{\tau_{\text{stimulated}}} + \frac{1}{\tau_{\text{spontaneous}}} \quad (7-10)$$

It follows from Eqs. 7-7, 7-9, and 7-10 that the radioactive lifetime τ depends on the photon density within the laser cavity and hence on the degree of excitation.

The higher the laser is driven above threshold, the smaller the stimulated lifetime becomes. It becomes the dominant factor of the radiative lifetime of the laser. For high excitation the stimulated lifetime τ_{stim} can reduce the radioactive lifetime τ by at least one magnitude over the spontaneous lifetime τ_{spont} .

Experimental results have been reported where the injection current was increased by more than twice the threshold current to eliminate the effect of prepumping due to the preceding bits. In doing so pulse code modulation of DH AlGaAs lasers of up to 500M bits/s could be realized with hardly any pattern distortions.

SECTION 8 FABRICATION OF ELECTRO-OPTIC BRAGG DIFFRACTION SWITCH

In Section 8-1 the fabrication of thin-film waveguides with electro-optic properties in single domain crystals is described; followed in Section 8-2 by an outline of the precision fabrication of metal electrode structures. In Section 8-3 the properties of an electro-optic Bragg diffraction switch in Ti-diffused LiNbO_3 are derived. The implementation of the Bragg diffraction switch in Ti-diffused LiNbO_3 has the advantage over that in $\text{LiNb}_x\text{Ta}_{1-x}\text{O}_3$, that the diffusion temperature for Ti is lower than the Curie temperature of LiNbO_3 , while the diffusion temperature of Nb is higher than the Curie temperature of LiTaO_3 . In Section 8-4 the function of the buffer layer is outlined.

A large single crystal of LiNbO_3 , y-cut, poled into single domain material with electro-optic properties must be purchased from "Crystal Technology" in California. The surface of the LiNbO_3 substrate should be smooth to approximately $\lambda/5$. It also has to be free of defects such as scratches and pits. Specifically, since the evanescent field penetrates into the substrate, the substrate also has to be defect-free below its surface for about one micron. A combination of chemical and mechanical polishing can yield the required results.

Before the metal is diffused, the substrate has to be cleaned thoroughly. This should be done without destroying the surface smoothness of the crystal.

For diffusion of Ti into the LiNbO_3 crystal, a thin layer of approximately 300Å of titanium is evaporated on the x-z surface of the

LiNbO_3 crystal. The crystal is heated in an Argon atmosphere at approximately 980°C for 4.5 hours and cooled off in flowing oxygen. This process should yield a single mode thin-film, electro-optic waveguide with a thickness between 1 and 2 wavelengths.

A layer of SiO_2 of 1000\AA thickness has to be coated on the thin-film waveguide to form a buffer layer.

A conformable photomask has to be fabricated which is the replica of the periodic electrode structure of the Bragg diffraction switch.

Photoresist AZ 1350 must be coated on the SiO_2 layer with a thickness of approximately 8000\AA . The conformable photomask must be placed in intimate contact with the photoresist, using a vacuum frame designed for this process. The collimated light of a mercury arc lamp must expose the photoresist below the gaps in the electrode pattern on the photomask. Following the exposure, a development step removes the exposed polymer, thereby leaving a relief pattern on the SiO_2 film.

The residual polymer and other organic contaminations must be removed from the interstices by the use of oxygen plasma.

In the following lift-off process, first the metal (Al or Au) is deposited by electron-beam evaporation on the top of the relief pattern and into the interstices to a thickness of about 1000\AA . Subsequently, the polymer of the relief pattern is dissolved to leave the periodic electrodes on the SiO_2 layer.

This is the last step in fabricating an electro-optic Bragg diffraction switch. The switch should now be ready to be tested optically.

8.1 FABRICATION OF ACTIVE OPTICAL WAVEGUIDES

The fabrication of the electro-optic Bragg diffraction switches for the integrated optic switching matrix is simplified because the coherent light needs only be confined in one dimension by the dielectric waveguide. The collimation of the coherent light beam in the orthogonal dimension is performed by an external microlens. Because of the one-dimensional confinement, the thin film guide can be a planar waveguide.

8.1.1 Ferroelectric Crystals

The electro-optic Bragg diffraction switch depends for its operation on the monocrystalline structure of the optically active material. This requires that the entire integrated switching matrix of eight inputs and sixteen outputs be fabricated on a single crystal. Because of their large electro-optic linear coefficients, the crystals should be either LiNbO_3 or LiTaO_3 . Both are ferroelectric. They are optically uniaxial with point group symmetry 3m. They also have high electrical resistivity to allow application of the modulation voltage. The most important properties of LiNbO_3 and LiTaO_3 are summarized in Table 8-1.

The lithium niobate is grown in large single crystals by the Czochralski pulling technique and single crystals are converted into single domain material by poling at elevated temperature. Large single domain crystals can be purchased from Crystal Technology. The largest standard size is 10mm x 10mm x 50mm. However, larger crystals up to 375mm length can be ordered. The lithium tantalate large single crystals are grown by the same pulling technique. The single crystals are poled at the Curie temperature. They can also be purchased from Crystal Technology. The largest standard size is 5mm x 5mm x 30mm. Again, larger crystals can be ordered.

Table 8-1. Properties of Single Domain Crystals

	LiNbO_3	LiTaO_3
Melting Point:	1260°C	1650°C
Curie Temperature:	1210°C	660°C
Optical Transmission:	Transparent from 0.4 to 5 microns	Transparent from 0.3 to 6 microns
Refractive Indices: at 0.6328 microns	$\begin{cases} n_o = 2.295 \\ n_e = 2.203 \end{cases}$	$\begin{cases} n_o = 2.177 \\ n_e = 2.181 \end{cases}$
at 0.8 microns	$\begin{cases} n_o = 2.257 \\ n_e = 2.175 \end{cases}$	
Electro Optic Coefficients at 0.6328 microns	$\begin{aligned} r_{33} &= +30 \times 10^{-10} \text{cm/V} \\ r_{13} &= +10 \times 10^{-10} \text{cm/V} \\ r_{22} &= +6 \times 10^{-10} \text{cm/V} \\ r_{51} &= +28 \times 10^{-10} \text{cm/V} \end{aligned}$	$\begin{aligned} r_{33} &= +30 \times 10^{-10} \text{cm/V} \\ r_{13} &= +7 \times 10^{-10} \text{cm/V} \\ r_{51} &= 1 \times 10^{-10} \text{cm/V} \\ r_{51} &= +20 \times 10^{-10} \text{cm/V} \end{aligned}$
Structure	Rhombohedral	Rhombohedral
	$a_H = 5.148 \text{\AA}$	$a_H = 5.143 \text{\AA}$
	$c_H = 13.863 \text{\AA}^\circ$	$c_H = 13.756 \text{\AA}^\circ$

8.1.2 Planar Active Optical Waveguides

The planar thin-film waveguide is formed on the surface of the single crystal of LiNbO_3 or LiTaO_3 by a layer of higher refractive index. The guiding layer for an efficient electro-optic Bragg diffraction switch must also have electro-optic properties. Several techniques have been reported to form the electro-optic thin-film waveguide; they are: out diffusion, metal diffusion and epitaxial-growth-by-melting.

8.1.2.1 Out-diffusion

To form a thin-film electro-optic guide by out-diffusion, advantage was taken that LiNbO_3 and LiTaO_3 can crystallize in a slightly nonstoichiometric form, $(\text{LiO}_2)_v(\text{M}_2\text{O})_{1-v}$, where $\text{M}=\text{Nb}$ or Ta and v ranges from 0.48 to 0.5. While the ordinary refractive index n_o is independent of v , the extraordinary refractive index n_e increases as v decreases. Therefore, reducing v at the surface of the crystal should result in an optical guiding layer. Because of the smaller size of Li compared to Nb or Ta, Li will diffuse more readily than Nb or Ta. Experiments are reported on heating LiNbO_3 and LiTaO_3 in vacuum for out-diffusion of LiO_2 .

Three LiNbO_3 crystals were heated in vacuum to 1100°C for 21 hours (I-2), 64 hours (I-3) and 135 hours (I-5), respectively. Air was then admitted while the samples were maintained at 1100°C for 2 hours. The crystals which had been clear, colorless and well polished before the treatment remained the same after the treatment. The change of the refractive index along the depth of the crystal, resulting from out-diffusion of LiO_2 is displayed in Figure 8-1. The shift of the interference fringes from the unperturbed pattern in Fig. 8-1 depicts the index profile. Distinct shifts in the interference fringes can be observed in Figures 8-1c and 8-1d, where the optical axis c is parallel to the crystal surface and the incident light is polarized as the extraordinary ray, parallel to the optical axis. The experimental index profile corresponding to the interference fringe shifts in Figures 8-1c and 8-1d is shown in Figure 8-2.

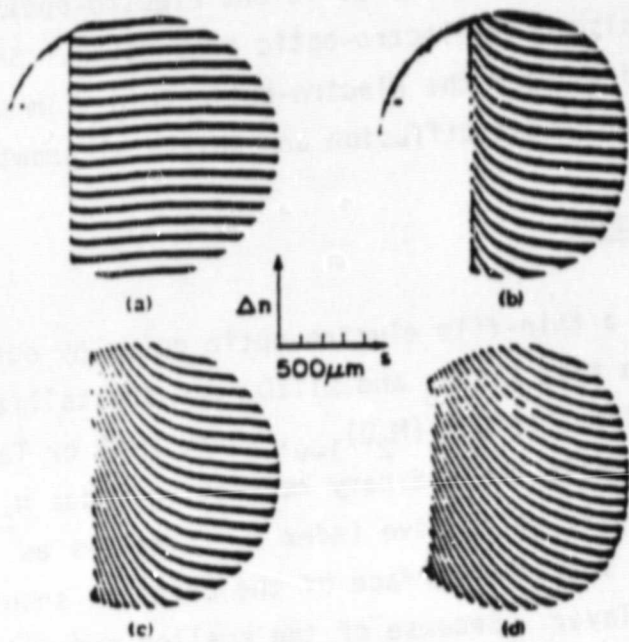


Figure 8.1 Interferograms: (a) ordinary wave, diffusion along c , I-2; (b) extraordinary wave, diffusion along c , I-2; (c) extraordinary wave, diffusion normal to c , I-2; (d) extraordinary wave, diffusion normal to c , I-3.

(I.P. Kaminow and J.R. Carruthers, Appl. Phys. Letters, Vol. 22, No. 7, 1 April 1973, p. 326)

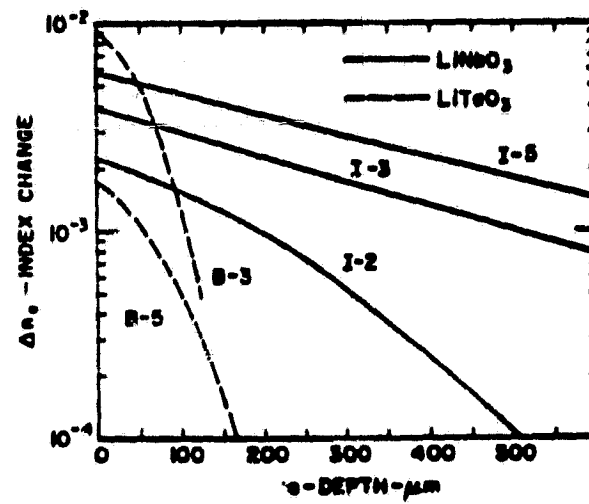


Figure 8.2 Experimental index profiles in LiNbO_3 and LiTaO_3 for diffusion normal to z.

(I.P. Kaminow and J.R. Carruthers, Appl. Phys. Letters, Volume 22, No. 7, 1 April 1973, p. 326.)

The profile of the extraordinary refractive index can be approximated by the complementary error function

$$\Delta n_e = A \operatorname{erfc}(s/B) \quad \text{Eq. 8-1}$$

where s is the depth below the surface and $B = (Dt)^{1/2}$ where D is the diffusion constant, t is the diffusion time and A is a function of t and T , where T is the diffusion temperature.

From Table 8-1 we conclude that the diffusion temperature remained below the Curie temperature ($T_c = 1210^\circ\text{C}$). Therefore, the crystals should not become depoled by the out-diffusion process at $T = 1100^\circ\text{C}$. This had been confirmed since the electro-optic coefficient r remained the same before and after the heat treatment.

Out-diffusion of LiO_2 from LiTaO_3 at temperatures below the Curie temperature of 660°C would be too slow. For out-diffusion of LiTaO_3 , diffusion temperatures were used which were above the Curie temperature and the depoled samples were subsequently repoled to reestablish their electro-optic properties. One crystal was heated in vacuum at 1150°C for 3 hours (B-5) and the other at 1400°C for 20 minutes. The experimental index profiles are shown in Fig. 8-2, where the optical axis is parallel to the crystal surface and the incoming wave is polarized as the extraordinary ray. Because the out-diffusion parameters for LiTaO_3 are different from those of LiNbO_3 , the product of diffusion constant D and diffusion time t , becomes smaller. Consequently, the diffusion depth s in Fig. 8-2 becomes also smaller for LiTaO_3 .

From the index profiles in Figure 8-2 we can conclude that the out-diffused waveguide can guide a large number of modes rather than a single mode and a different technique must be used to form an electro optic single mode waveguide.

8.1.2.2 In-Diffusion

The most promising technique is the in-diffusion of metal into LiNbO_3 or LiTaO_3 to provide electro-optic, single mode low-loss waveguides. However, at the high diffusion temperatures, out-diffusion occurs simultaneously with the metal in-diffusion.

The most efficient electro-optical thin-film waveguides which have been reported, are formed by diffusion of titanium into LiNbO_3 and by diffusion of Nb into LiTaO_3 . Diffusion of certain metals into the ferro-electric single crystals produce a composition gradient, where the metal mole fraction decreases towards the interior of the crystal. The refractive indices for ordinary and extraordinary rays decrease with decreasing mole fraction of the metal.

Prior to the diffusion the crystal surface must be cleaned and polished to great smoothness. The surface must be free of any defects as far into the substrate as the evanescent field of the guided mode will reach. Mechanical or chemical polishing or a combination of both can produce such a defect-free surface.

To form a metal-diffused, thin-film, electro-optic waveguide, a thin layer of metal of thickness τ is first evaporated onto the surface of the ferro-electric crystal and then the crystal is heated at temperature T in a nonreactive atmosphere for a time t . The important waveguide parameters - number of modes M , maximum index change Δn and effective guide thickness b - can be independently controlled by the diffusion parameters τ , T and t .

8.1.2.2.1 Ti-Diffusion into LiNbO_3

For diffusion of Ti into LiNbO_3 , thin layers (200 - 800 \AA) of Ti are evaporated on one of the crystal faces of the LiNbO_3 crystal. The crystals are heated in flowing Ar (to prevent oxidation of the metal) to a temperature in the range of 850 - 1000°C (below the Curie temperature of LiNbO_3) in a time less than 1 hour and the diffusion time t was

measured from that point. After time t , flowing oxygen was admitted (to reoxidize the LiNbO_3) and the oven switched off. For sufficiently long diffusion times, all the metal disappears from the surface. If the diffusion is stopped before all the metal enters the crystal, an oxide residue forms on the surface which can be removed by very lightly hand-polishing the surface.

Observation of the index profile has shown that Ti-diffusion forms a layer where the refractive indices of the ordinary and the extraordinary ray are higher than those of LiNbO_3 . The concentration profile, that is the Ti to Nb count ratio versus depth below the surface (y) approaches a Gaussian function for diffusion times long compared to the time required for the metal film to completely enter the crystal. It is

$$c(y, t) = (2/\sqrt{\pi}) (\alpha\tau/b) \exp(-\lambda^2/b^2) \quad \text{Eq. 8-2}$$

where α is the number of atoms per unit volume in the deposited Ti film of thickness τ ,

$$b = 2(Dt)^{1/2} \quad \text{Eq. 8-3}$$

and the diffusion constant D is

$$D = D_0 \exp(-T_0/T). \quad \text{Eq. 8-4}$$

For short diffusion times, where the metal is not completely diffused into the crystal, the concentration profile should be a complementary error function, as given in Equation 8-1.

Several experimental LiNbO_3 crystals with Ti layers of 400Å were heated at 850°C for 6 hours and at 950°C for 6 hours. In both cases the metal film appeared to be completely diffused into the crystal. However, in the first case the concentration profile had the shape described by a complimentary error function. In the second case, because the diffusion rate is much greater at the higher temperature,

the concentration profile has Gaussian shapes.

Since the refractive index change $\Delta n(y)$ is proportional to the concentration change of Ti $c(y)$ for the Gaussian profile, the increase of the refractive index at the surface, $\Delta n(0)$, is

$$\Delta n(0) = (2 \sqrt{\pi}) (\alpha \tau / b) \frac{dn}{dc} \quad \text{Eq. 8-5}$$

While the increase of the refractive index at the crystal surface can be controlled by adjusting τ , the diffusion depth in Equations 8-3 and 8-4 can be controlled independently by varying t and T .

The largest increase of refractive index by Ti-diffusion on the surface of a LiNbO_3 crystal which had been reported, was the increase of the extraordinary refractive index to $\Delta n_e(0) = 0.04$. It was measured on crystals where the surface was parallel to the optical axis. The diffusion depth b was 1 micron.

The dominant sources of waveguide loss are scattering from crystal surface imperfections and, possibly, absorption by the metal ions. The measured losses at 0.63 microns were estimated to be about 1db/cm.

Experimental Ti-diffused thin-film waveguides in LiNbO_3 for the single section Cobra switch have been reported. Approximately 500Å of Ti was deposited by rf sputtering on the LiNbO_3 substrate. The Ti was diffused into the LiNbO_3 in an O_2 atmosphere at 1100°C for 11 hours to form the desired guided structure.

For the experimental two-section Cobra switch, a z-cut LiNbO_3 crystal was used and the Ti-diffused waveguide was parallel to the y-axis. To form the waveguide a layer of Ti 300Å thick was evaporated on the LiNbO_3 . The Ti was diffused into the LiNbO_3 at 980°C for 4.5 hours in an argon atmosphere and cooled in oxygen to form a single mode waveguide.

For the experimental Bragg diffraction switch in thin-film channel waveguide, Ti 200 \AA thick was e-beam-evaporated on a y-cut LiNbO_3 substrate. Diffusion was carried out at temperatures of 850 - 900°C in a flowing oxygen atmosphere. The diffusion time varied from 5 to 16 hours.

8.1.2.2.2 Nb Diffusion into LiTaO_3

Thin-film electro optic waveguides were also formed in LiTaO_3 by diffusing a layer of metallic Nb into the surface to exchange some of the Ta^{+5} for Nb^{+5} ions, so as to form a layer of $\text{LiNb}_x\text{Ta}_{1-x}\text{O}_3$. Since both the refractive indices of the ordinary and the extraordinary ray of LiNbO_3 exceed those of LiTaO_3 , (Table 8-1) a guiding thin-film waveguide results.

The waveguides are formed by evaporating metallic Nb onto polished LiTaO_3 substrates. The Nb thicknesses were varied from 150 \AA to 1500 \AA . The coated crystals are annealed in an argon atmosphere at temperatures close to 1100°C for times ranging upwards from 6 hours. The Nb diffuses into the crystal and takes up lattice positions replacing some of the Ta. Since the diffusion temperature of 1100°C is higher than the Curie temperature of LiTaO_3 of 660°C (Table 8-1), the crystals become depoled. To reestablish their electro-optic properties the crystals must subsequently be repoled.

The crystals, after the treatment, are clear and transparent. A typical concentration profile for the Nb after in-diffusion into the LiTaO_3 crystal, is shown in Figure 5-2. The relative Nb concentration (x in the formula $\text{LiNb}_x\text{Ta}_{1-x}\text{O}_3$) as a function of the depth, is consistent with film formation by a diffusion process. The refractive indices of the single mode $\text{LiNbTa}_{1-x}\text{O}_3$ are higher than those of the LiTaO_3 . In fact they are between those of LiNbO_3 and those of LiTaO_3 . In an x-z plane $\text{LiNb}_x\text{Ta}_{1-x}\text{O}_3$ crystal for the TE_0 -mode, propagating at 51° to the z-axis (used for the Bragg diffraction switch in Figure 3-4) the refractive index is 2.188 at 0.632 \AA . This falls in the range between 2.179 and 2.237 which are the indices in this direction for pure LiTaO_3 and LiNbO_3 , respectively.

To evaluate whether the $\text{LiNb}_x\text{Ta}_{1-x}\text{O}_3$ thin film can guide only a single mode, the mode content was computed using the analysis by D. Marcuse. In this analysis the squares of the graded refractive index distribution is approximated by a piece-wise, linear distribution, for which exact solutions of the guided - wave problem can be obtained. Since the refractive index change is proportional to the change of Nb concentration with depth, the distribution in Figure 5-2 was used for the computation. The linear pieces for $n_0=2.188$ to $n_1=2.1833$ extended from $x=0$ to $x_1=0.77$ micron, and for $n_1=2.1833$ to $n_2=2.179$ extended from $x_1=0.77$ micron to 1.5 microns.

The result of the computation was that the $\text{LiNb}_x\text{Ta}_{1-x}\text{O}_3$ film with the concentration profile in Figure 5-2 can only support a single mode.

One has to realize that at a high diffusion temperature simultaneously to the metal in-diffusion, out-diffusion of LiO_2 occurs (Section 8.1.2.1). This presents a serious problem when channel waveguides are diffused since the out-diffusion forms a planar waveguide outside the channel waveguide, formed by metal in-diffusion. However, for the electro-optic Bragg diffraction switch which is built in planar waveguide, the increase in refractive index at the crystal surface due to out-diffusion only adds to the increase in refractive index due to metal in-diffusion. Furthermore, for metal in-diffusion, the increase of the refractive index is approximately 10 times as large as the refractive index increase by LiO_2 out-diffusion.

8.2 FABRICATION OF PERIODIC METAL ELECTRODES

In the electro-optic Bragg diffraction switch, the precision in setting up the diffraction grating is determined primarily by the precision in forming the periodic electrodes. Photolithography, specifically shadow printing, together with lift-off techniques, should yield a precision in forming the electrode structure of better than 1

micron. These techniques have been used previously to form a periodic electrode structure, with a periodicity of 4 microns and an electrode gap-to-width ratio of one.

Photolithography requires that the surface of the Bragg diffraction switch is coated with a radiation sensitive polymer film and exposed to radiation through a photomask to form the desired pattern. Following the exposure, a development step removes the exposed polymere (positive process), thereby leaving a relief pattern on the surface. In the following process, the lift-off process, the metal which forms the electrodes, is desposited into the interstices of the polymer relief pattern. The fabrication of the metal electrodes is shown schematically in Figure 8-3.

For thin film optical work, a positive polymere, named photoresist AZ 1350, has been developed with resolution better than 0.05 micron. The photoresist AZ 1350 is a strong absorber of ultraviolet light. When exposed to radiation it undergoes photochemical decomposition and enhanced solutility of the photoresist in aqueous alkaline solutions.

To form the pattern on the photoresist, a photomask of the pattern must be generated. The photomask is a glass plate where the pattern is formed of a thin-film absorber of ultraviolet light, as chromium, F_2O_3 , silicon or photographic emulsion. The thin-film absorber pattern is placed in contact with the photoresist and the pattern is transferred to the photoresist by passing collimated ultraviolet light through the photomask. Photolithography is comparatively simple and inexpensive and the field of view is limited only by the size of the photomask and the diameter of the collimated ultraviolet light.

To consistently achieve line-width control of 1 micron or below, any diffraction effects have to be greatly reduced. This can be accomplished only when any gap between the photomask and the photoresist is avoided. For intimate contact, a conformable photomask must be used,

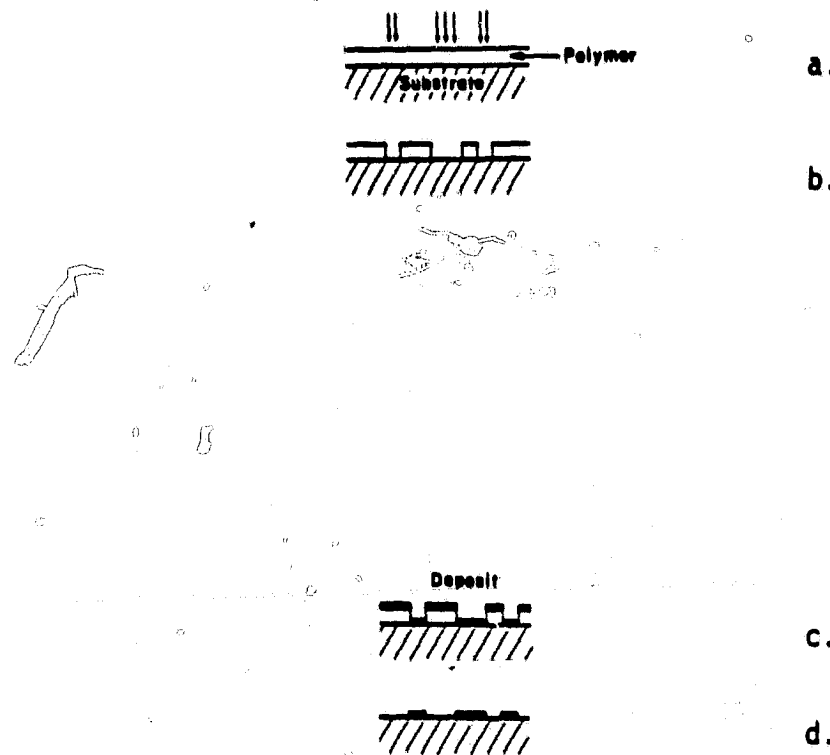


Figure 8-3. Schematic of fabrication of metal electrodes.

as shown in Figure 8-4.

The conformable photomask consists of a pattern in thin-film chromium of 0.05 to 0.1 micron of Fe_2O_3 of 0.13 micron, on Corning type 0211 glass, 0.2 mm thick. The vacuum sucks the photomask to the photoresist to readily conform to its contour.

With intimate contact, diffraction effects can take place only over the thickness of the photoresist film. Wave diffraction occurs because of the nature of light which penetrates into the shadow area of the absorbing sections of the photomask. In the Fresnel region, progressive diffusion of the optical field into the shadow region occurs with increasing distances from the absorbing strips of the photomask. For an index of refraction of the photoresist of $n=1.6$, the wavelength of a mercury arc lamp of 4000\AA in air, becomes 2500\AA inside the photoresist. Thus, to avoid rounding of the sidewalls of the relief pattern, the photoresist should have no more than a few wavelength thickness. Some compensation is possible by adjusting the exposure time to obtain more vertical side walls. (Figures 8-5, 8-6). However, when exposure takes place and the photomask is not in intimate contact with the photoresist, diffraction in the air gap causes the profile to have sloped side walls. (Figure 8-7). Such a profile is unsuitable for the lift-off technique.

The relief pattern formed by contact photolithography is shown schematically in Figure 8-3b. The lift-off process which deposits the metal into the interstices of the polymer relief pattern is shown in Figures 8-3c and 8-3d. In the first step of the lift-off process, the metal, which is either aluminum or gold, is electron-beam evaporated from a source at a distance of approximately 40cm. The metal must arrive at the relief pattern at near-normal incidence. In the second step of the lift-off process, the polymer is dissolved to leave the periodic electrode pattern on the surface of the thin-film waveguide. To dissolve the polymer, it is required that there is little or no continuity between the material deposited on the thin-film waveguide and that deposited on top of the polymer. For preventing this continuity, it is required that the sidewalls of the polymer relief pattern be vertical.

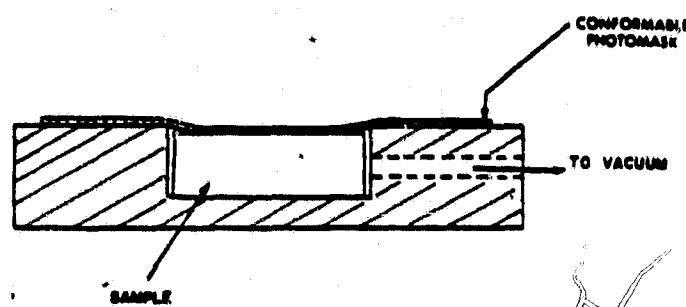


Figure 8-4. Schematic diagram of a simple vacuum frame for obtaining intimate contact between a substrate and a conformable photomask.

(H.I. Smith, Proc. IEEE, Vol. 62, No. 10, Oct. 1974,
p. 1361.)

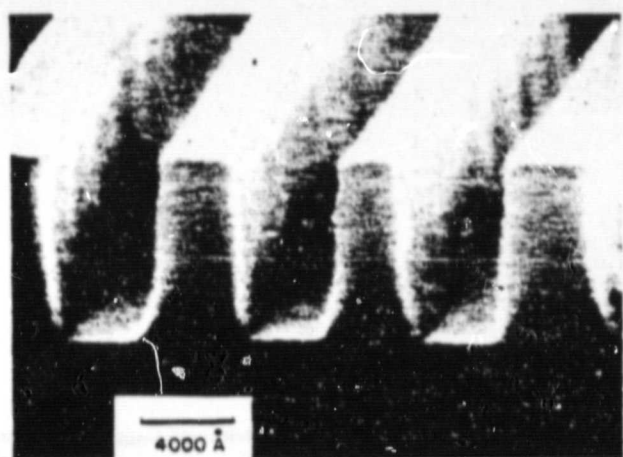


Figure 8-5.

Scanning electron micrograph of the cross section of a grating pattern exposed in AZ 1350H photoresist using a high-pressure mercury arc lamp and the conformable photomask-intimate contact technique. The photoresist is 9800 Å thick. Because of the angles used in microscopy, vertical dimensions are foreshortened relative to lateral dimensions. The scale refers to lateral dimensions only. The photomask consisted of 5 slits in an 800-Å thick chromium film on 0211 glass. It was made by scanning-electron-beam lithography and chemical etching of the chromium, which caused irregularities along the edges of the slits. These small irregular features are replicated in the photoresist. The smaller space between two of the slits was in the original mask, and was caused by an error in the scanning-electron-beam pattern generator. (Micrograph by Eager.)

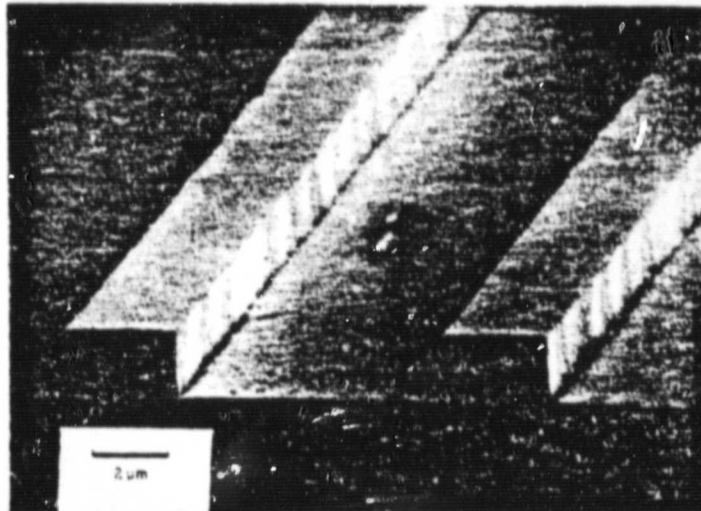
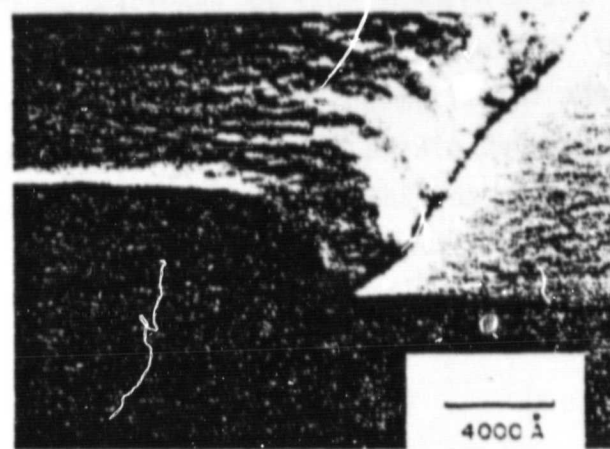


Figure 8-6.

Scanning electron micrograph of the cross section of a grating pattern exposed in AZ1350H photoresist, 18 000 Å thick.

(H.I. Smith, Proc. IEEE, Vol. 62, No. 10,
Oct. 1974, p. 1361)

ORIGINAL PAGE IS
OF POOR QUALITY



Scanning electron micrograph of the cross section of the edge of a pattern exposed in AZ1350 photoresist, 5000 Å thick. The photo-mask was located about 2 μ m away from the top of the AZ1350. The resulting diffraction caused the rounding of the side-wall profile.

Figure 8-7.

(H.I. Smith, Proc. IEEE, Vol. 62, No.10,
p. 1361.)

For good adhesion of the deposited metal, residual polymer or other organic contamination must be removed from the interstices of the relief pattern prior to the lift-off process. This can be accomplished most efficiently by the use of oxygen plasma. Oxygen plasma is harmless to most crystals used for thin-film optical waveguides. The treatment must be short because some of the polymer of the relief pattern is also removed. It has been found that exposure of the thin-film optical waveguide with the polymer pattern to an oxygen plasma for a time sufficient to remove about 100 \AA of the polymer thickness is more than adequate to ensure clean-up of the exposed thin-film surface.

SECTION 9

SINGLE-MODE FIBER SPLICING

The development of single mode optical fibers has proceeded very quickly in the last year. In addition, splicing technology has rapidly advanced, i.e., fiber fusion splicing sets have become commercially available for multimode and single mode fiber. Specifically, "Northern Telecom Canada, Limited", in Montreal, is producing a fiber fusion splicing set for single mode fibers, as shown in Figure 9-1. Fusion is achieved, using an AC arc. The unit is also used to install a protective heat-shrinkable tubing package over the fused fibers.

Alignment of the fibers is achieved without micromanipulation. A prefusion cycle can be used to minimize insertion loss. The arc power and duration are adjusted for the specific fiber being used and then controlled automatically by the set. The splicing loss averages about 0.25dB for multimode fiber. In the application of interest, single mode fiber would be used. This fiber would result in somewhat higher losses in splicing.

The operating procedure is as follows:

- 1) Strip the fiber ends of any protective coating.
- 2) Cleave the fiber ends (using a suitable tool) to provide a smooth, flat end surface.
- 3) Place the heat-shrinkable tubing package over one fiber end, away from the fusion area.

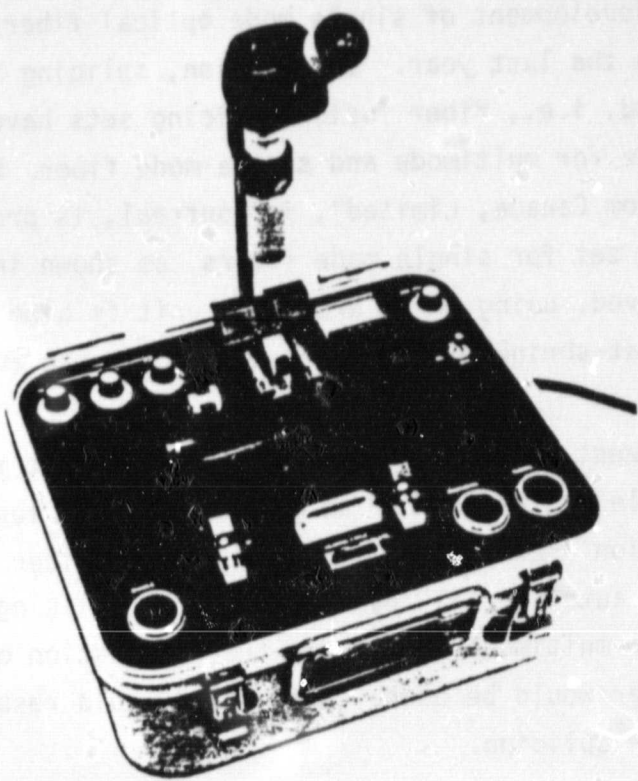


Figure 9-1. Fiber Fusion Splicing Set
by Northern Telecom Canada Limited

ORIGINAL PAGE IS
OF POOR QUALITY

- 4) Clean the fiber ends, using methanol or acetone.
- 5) Locate the fiber ends in the alignment head.
- 6) Observing through the magnifier, separate the fiber ends slightly and preheat (to round the ends).
- 7) Touch the fiber ends together and fuse.
- 8) Place the package over the fuse area, lower the fibers into the heater and activate the timed heater.
- 9) Raise the completed splice out of the heater and remove from the handling arms.

At this stage of the switch development, it appears that the single mode fiber splicing will be commercially available with low loss in the early 1980's. As a result, the fiber splicing is not believed to be a significant problem.

SECTION 10

DATA FLOW, ACCESS TECHNIQUE, ARCHITECTURE AND PROTOCOL

In the Final Report on the NASA Contract NAS5-24449 of February, 1979, the conceptual design of an optical switching center had been developed, which is shown in Figures 10-1 and 10-2. The switching function is performed by an integrated optics switching matrix, using electro-optic Bragg diffraction switches. The data flow through the switching matrix in Figures 10-1 and 10-2 is that characteristic of a common control space-division switching module. In a common control space-division switching system, the number of connections are limited by the number of physical lines between stations. Also, the common equipment is occupied only during the initial stage of a connection and after the connection is terminated. The connection itself requires only the activation of the appropriate relays in the respective transmission lines.

In the integrated switching matrix, the number of connections is also limited by the number of input and output laser beams. Also, to establish a connection, a single Bragg diffraction switch at the intersection of the respective input-output laser beams needs to be activated. It follows that the optimum data flow through the optical switching center in Figures 10-1 and 10-2 can only be that of a common control space-division switching system.

The typical access technique in a common control space-division switching system is shown schematically in Figure 10-3. The actual switching function between input and output lines, performed by the switching matrix, is controlled by the marker (MKR). The function of the marker is first to interpret the address which precedes the information on the incoming data stream. The address is, in general, in form of a pseudo-noise digital waveform. After interpreting the address, the marker establishes the connection by activating the respective Bragg diffraction switch. The marker is assisted in its work by an originating register (OR), the main function of which is the interpretation of the address.

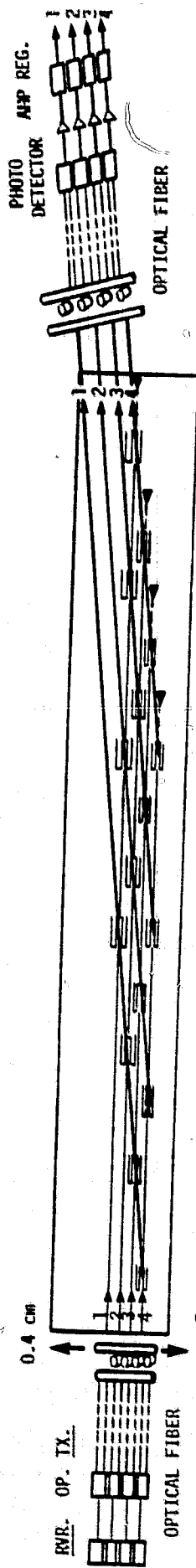


Figure 10-1. Conceptual design of optical switching system

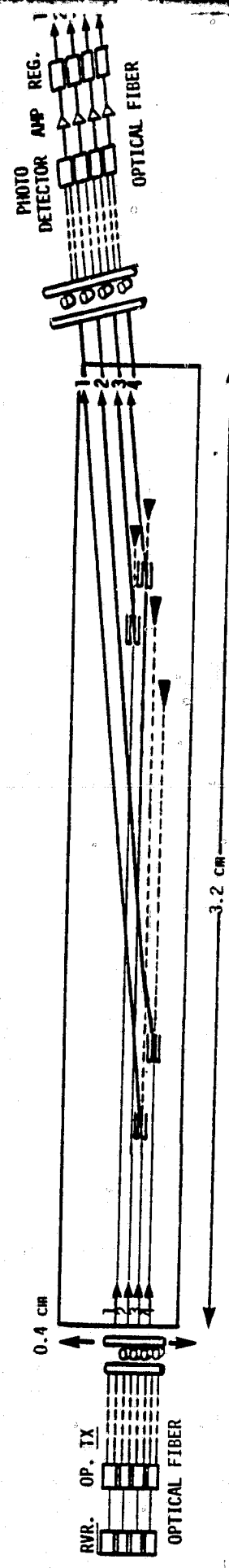


Figure 10-2. Conceptual design of optical switching system (in operation)

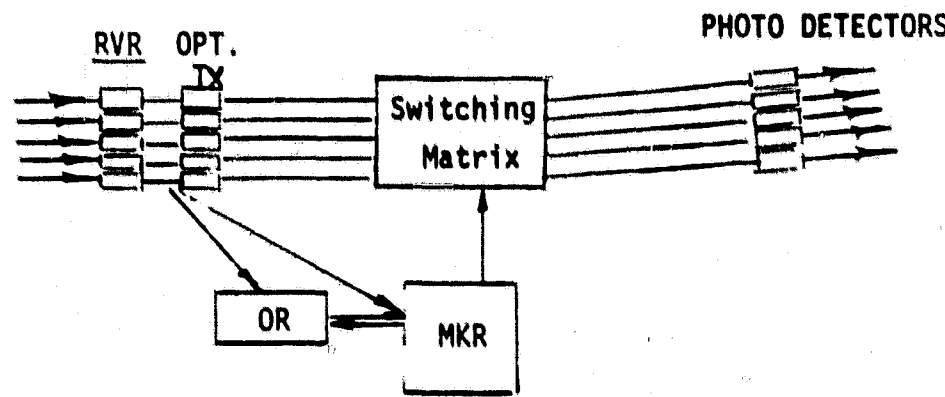


Figure 10-3. Access Technique in Common Control Space-Division Switching System

The keys to establishing a connection are:

- 1) The market is signalled that a new connection is to be made, for example, for input line A.
- 2) The marker instructs input line A to connect to the input of OR; then the marker releases.
- 3) The OR interprets the address and passes it to the marker.
- 4) The marker tests whether the output line to be addressed is already connected. If it is a priority override can be established.
- 5) The marker makes the appropriate interconnection between line A and the designated user line.

The architectural scheme for the optical switching system is shown in Figures 1 and 2. The digital high data rate stream of each channel is modulated on an injection laser. The properties of the integrated optics switching matrix require that the laser radiation be spatially coherent. Because of the high data rate (up to 300Mb/s) and because of the considerable distances (up to 200 feet) for transmission of the data streams, optical fibers are used from the optical transmitters to the switching matrix. For these input connections single mode optical fibers must be used. The optical fibers are connected by an endfire coupler, formed by crossed cylindrical micro-lenses, to the switching matrix. A similar endfire coupling technique is used to form the output connections from the switching matrix to the output optical fibers. Each channel is then detected, amplified, reshaped and processed.

The optical switching system, using a space-division switching module, does not limit the protocol, that is, the data packaging of the incoming data streams. The data streams can be frequency-division

multiplexed by loading each input line with N channels each of a discrete narrow frequency range, which are transmitted simultaneously. The data streams can also be time-division multiplexed, where representative samples of each of the N channels are taken and transmitted sequentially. The design approach of the integrated optics switching matrix, which uses a space-division scheme, is such that it does not restrict the multiplexing or data packaging technique.

SECTION 11 RESOURCES

The capability to build an optical high data rate switching center as shown conceptually in Figures 10-1 and 10-2 with up to 8 inputs and 16 outputs relies on present developments of large elongated single LiNbO_3 or LiTaO_3 crystals and single transverse mode injection lasers, operating at 0.83 and 1.23 microns.

The elongated shape of a single crystal LiNbO_3 or LiTaO_3 substrate required for a 8 X 16 switching matrix, can be fabricated from a single large crystal, made by the Czochraski pulling technique. "Crystal Technology, Inc.", in Mountain View, Ca., is the only supplier of high quality single crystal LiNbO_3 and LiTaO_3 substrate in the United States. Single x-cut and y-cut crystal substrates 1 in. and $1\frac{1}{2}$ in. square are available (delivery time not to exceed eight weeks). Single y-cut LiNbO_3 crystals are being developed where the length along the z-axis can be up to 15 in. and along the x-axis can be up to 2 or 3 inches. But these crystals can not be used for building the switching matrix with the electro-optic Bragg diffraction switches. No development is planned to pull y-cut single crystals so that the longer dimension is along the x-axis.

However, single x-cut crystals are presently being developed by "Crystal Technology, Inc." with the long dimension along the y-axis. Tentative dimensions are 5 to 10 in. along the y-axis, and $1\frac{1}{2}$ in. along the z-axis. Fortunately, there is complete symmetry of the electro-optic properties of the integrated optics switching matrix, using electro-optic Bragg diffraction switches, between the y-cut single crystal with the direction of propagation along the x-axis, and the x-cut single crystal with the direction of propagation along the y-axis. Consequently, the large switching matrices using Bragg diffraction switches can also be implemented on the elongated x-cut single LiNbO_3 crystal substrate where the longer dimension is along the y-axis.

The development of the x-cut crystal with the long dimension along the y-axis at "Crystal Technology, Inc." is expected to proceed simultaneously with the development of the 2 X 2 building block of the larger switching matrix. Hopefully, the large elongated x-cut single crystal LiNbO_3 substrate with the long dimension along the y-axis will become available at the time when the large switching matrices under a follow-up contract should be fabricated.

An important development of new injection lasers can lead to a decrease in length of the large switching matrices. "Laser Diode Laboratories" in Metuchen, New Jersey, is in the process of fabricating InP lasers with the center wavelength at 1.23 microns. The same company has also, in the last year, developed a single transverse mode $\text{Al}_{1-x}\text{Ga}_x\text{As}$ laser and will proceed to develop a single transverse mode InP laser, radiating at 1.23 microns. Using these lasers with $\lambda_0 = 1.23$ microns will allow to increase the Bragg angle to $\theta_B = 4^\circ$ and to decrease the minimum spacing between Bragg diffraction switches along the input laser beams by a factor of 0.68. Thus, i.e., the length of the 8 X 16 switching matrix could be reduced to 220mm or to less than 10 inches.

SECTION 12

CONCLUSIONS AND DEVELOPMENT PROGRAM

12.1 CONCLUSIONS

The feasibility study of the switching center, using an integrated optic switching matrix has been completed. The tentative requirements for the switching center are a high data rate throughput (up to 300 Mbits/s) having 8 input lines and 16 output lines. Fiber optic transmission is considered for interconnection in the switching center owing to the high data rate and considerable transmission distances within the center. The optical transmitters of the switching center use injection lasers and transform the output from RF receivers to optical data streams. Direct modulation of the injection lasers is used, which requires a separate optical channel for each RF receiver.

The feasibility study shows that a high data rate switching center, using an integrated optics switching matrix, can be implemented and should meet the requirements outlined in the Statement of the Problem in Section 1. The switching matrix uses electro-optic Bragg diffraction switches. It also uses terminations in-line with the input laser beams. A key feature of the electro-optic Bragg diffraction switches is that the switched "off" position does not adversely affect wave propagation. The feed-through owing to the limited deflection efficiency (80 percent) of the switch in the "on" position can be eliminated by optical terminations. An additional feature is that only one switch in the matrix needs to be energized for connection of an input port to an output port.

The electro-optic Bragg diffraction switches in the switching matrix are built in planar waveguide. This one-dimensional confinement property makes it possible for the "off" position to not adversely affect wave propagation. This design requires that the radiation from the input optical fibers be collimated with external

optics. The collimated laser beams forming the 8 input terminals and the deflected laser beams forming the output terminals, must be parallel to each other. The collimation of the input laser beams is performed by the microlenses of the endfire coupler. Achieving low cross talk depends on the precision alignment of these microlenses. Though the endfire coupling method has not been tested, a related technique had been used previously with very good results.

A novel method of cross talk reduction based on coherent mode selection in the Fourier plane of the output coupling microlenses should help to reduce the cross talk to the required level.

The development effort of the program must be directed towards designing the electro-optic Bragg diffraction switches to be commensurable with the limited size of the single ferroelectric crystal, forming the substrate of the switching matrix. Fortunately, the geometry of the switching matrix is well matched to the cross section of a pulled single ferroelectric crystal. Also, the development effort must concentrate on the implementation of the endfire coupler with specific emphasis on the precision alignment of the cylindrical microlenses forming the parallel laser beams.

Cross talk reduction technique, which is based on coherent mode selection in the focal plane of the output coupling microlenses, must be tested. The modulation of single transverse mode laser transmitters up to 300 Mbits/s should be perfected to minimize distortion and prepumping effects.

12.2 DEVELOPMENT PROGRAM

The objective of the development program is to develop an operational optical switching center, using an integrated optical switching matrix by 1982. The different phases of the program are given in the phasing charts 12-1 and 12-2.

Table 12-1

**INTEGRATED OPTIC SWITCHING SYSTEM
DEVELOPMENT PROGRAM
1979-1981**

PHASE 2

DEVELOPMENT OF SINGLE ELECTRO-OPTIC
Bragg Diffraction Switch
FOR USE IN
4x4 AND 8x16 SWITCHING MATRIX

1. Develop and evaluate optical waveguide for electro-optic Bragg diffraction switch

Test at $\lambda = 0.632$ micron

 - Order material including single crystal LiNbO_3 1" x 1"
 - Diffuse Ti into LiNbO_3 to diffusion depth of ≈ 1 micron
 - Test Ti-diffused LiNbO_3 waveguide
 - Coat Ti-diffused LiNbO_3 with SiO_2
 - Test SiO_2 coated Ti-diffused LiNbO_3 waveguide
2. Investigate 4 X 4 and 8 X 16 Switching Matrix

 - Investigate crystal availability as a function of size, cost and purity for 1982.
 - Optimize design of Electro-Optic Bragg diffraction switch for 4 X 4 and 8 X 16 switching matrix for largest crystal size in 1982.
3. Develop & Evaluate Optimized 2 X 2 Switching Matrix at $\lambda = 0.632$ microns

 - Fabricate periodic electrode on SiO_2 coated Ti-diffused LiNbO_3
 - Test electro-optic Bragg diffraction switch at 0.6328 microns
 - Build and test 2 X 2 switch matrix at 0.6328 microns
4. Demonstration

PHASE 3

1. Evaluate 1 X 1 Switch at $\lambda = 0.32$ micron
 - Purchase single mode AlGaAs laser
 - Develop End-fire coupling
2. Investigate Cross-talk rejection
3. Couple Single Mode laser to Optical Fiber
4. Evaluate and Implement End-fire Coupling
5. Build and Evaluate 2 X 2 Switching Matrix at $\lambda = 0.32$ micron
6. DEMONSTRATION

A Gantt chart illustrating the timeline for the construction of a bridge, spanning from week 1 to week 18. The tasks and their scheduled start and end dates are as follows:

Task	Start Date	End Date
Foundation	Week 1	Week 4
Piling	Week 4	Week 7
Deck	Week 7	Week 12
Railing	Week 12	Week 18

Notes: A horizontal line is drawn at week 12, and a vertical line is drawn at week 12, both labeled with the Greek letter Δ . There are also several small rectangular boxes drawn on the chart, particularly in the Foundation and Piling phases.

ORIGINAL PAGE IS
IF POOR QUALITY

Table 12-2
INTEGRATED OPTIC SWITCHING SYSTEM
DEVELOPMENT PROGRAM

	1978-1979	1979-1980	1980-1981	1981-1982	1982-1983
Phase 1 Feasibility Study					
Phase 2 Develop 2 X 2 switch; test with HeNe laser					
Phase 3 Test 2 X 2 switch with AlGaAs laser using optimized endfire coupling					
Phase 4 Develop and test 4 X 4 switching matrix; incorporate in switching center Modulate laser with 300Mb/s					
Phase 5 Develop and test 8 X 16 switching matrix,; incorporate in switching center					
Phase 6 Field test switching center					

APPENDIX A

The concept of the integrated optics switching system in Figure 3-1 has been developed in the course of the feasibility study. To derive at the switching concept in Figure 3-1, the characteristics of different types of integrated switches were investigated, also different types of switching network designs, couplers and integrated laser configurations were studied.

A1.1 INTEGRATED COBRA SWITCH

A1.1.1 Introduction

In general, optical switching techniques for integrated optical systems either take advantage of the electro-optic or the acusto-optic effect. Of these integrated switches, the alternating ΔS cobra switch has the special property that the straight-through power transfer as well as the cross-over power transfer can be controlled independently by voltage tuning. This feature allows the cross-talk to be minimized in both switching positions. The operation principle of this type of switch is described and the effect of temperature changes evaluated in the following.

A1.1.2.1 Operating Principle

The objective of this investigation is to determine the merits and performance characteristics of an integrated "cobra" switch.

A1.1.2.1 Operation Principle

The cobra switch is formed by an integrated optical directional coupler where the electro-optic effect is used to switch from the synchronous coupling mode to the asynchronous coupling mode. The switch had been realized in LiNbO_3 by diffusion of titanium to form channel waveguides. Thin metal electrodes are sputtered on the two channel waveguides. The electrode configuration is shown in Figure A-1. An electric voltage across the electrodes increases the refractive index in one waveguide and decreases it in the second waveguide.

The electric field E is applied along the optical axis of the uniaxial LiNbO_3 crystal (Figure A-2). The optical E_{11}^y - mode (TM) is excited with the optical electrical field vector parallel to the optical axis of the crystal (Figure A-2). This linearly polarized field vector is in direction of the extra-ordinary wave of the crystal. Its change in effective index with voltage is

$$n_{1, \text{TM}} = n_e - \frac{n_e^3}{2} r_{33} E \quad \text{A(1)}$$

where for LiNbO_3 $n_e = 2.17$ at a wavelength of 0.8 micron and the electro-optic tensor coefficient $r_{33} = 32.2 \times 10^{-10} \text{ cm/volt}$.

Though the electro-optic coefficient has the highest value for the E_{11}^y mode, the metal contact should adversely affect the channel

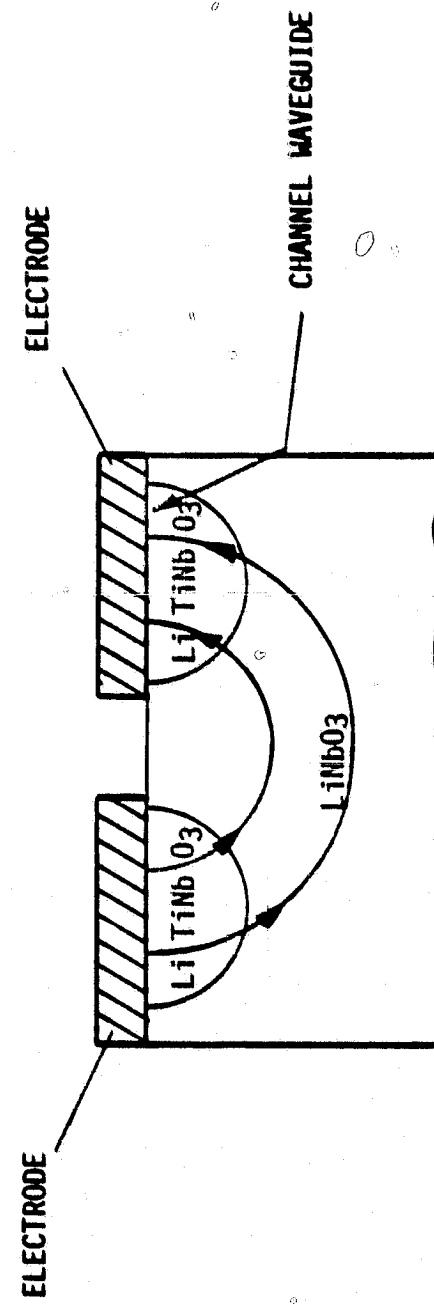
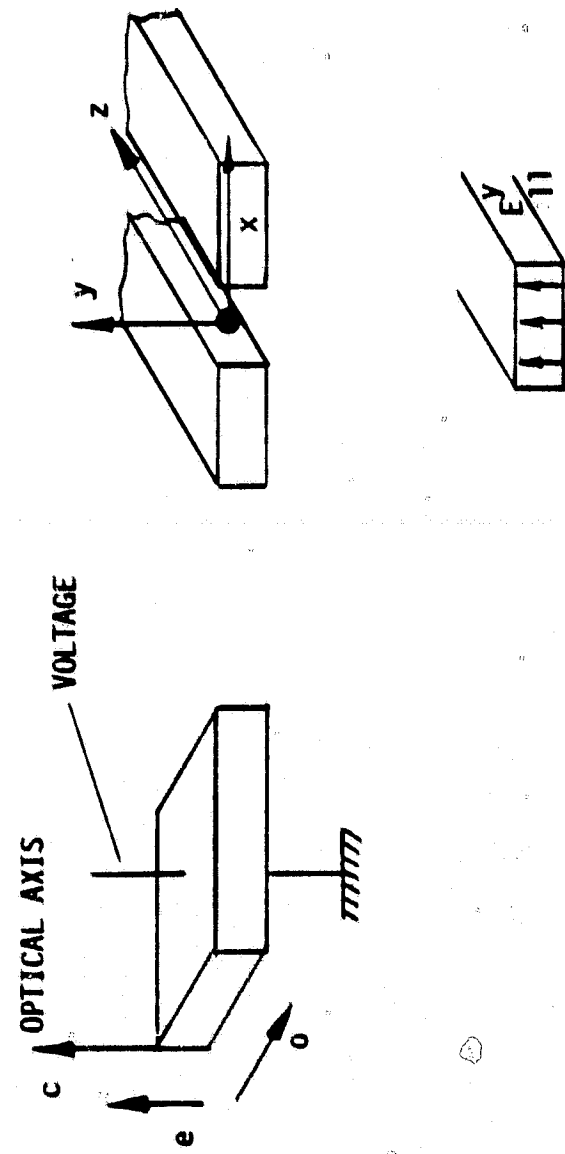


Figure A-1. Cobra Switch

M. Papuchio, et al.
Appl. Phys. Letters, Vol. 27, No. 5, 1 Sept. 1975, p. 269

Figure A-2. Orientation of TM-Mode



waveguide mode. That is, the maximum thickness b_{\max} for which the channel waveguide can support only the fundamental mode,

$$b_{\max} = \frac{\lambda}{2(n_1^2 - n_2^2)^{1/2}} \quad A(2)$$

(where n_1 is the refractive index inside the guide and n_2 is the refractive index of the substrate) is changed by the metal contact to a smaller value.

Also losses are introduced. Though the losses are only 2 db/cm, they should adversely affect the characteristics of the directional coupler. This is because the coupling equations which were derived for lossless elements are also valid for lossy propagation, but only when the propagation constant k_z (along the coupler) is complex but the term $n_1^2 - n_2^2$ is real. Such a case occurs when the absorption in the guide and in the substrate are the same. The metal contacts on the guides in the TM-mode in Figure A-1 increase the losses in the guides but not in the substrate. Therefore, the symmetry required for the validity of the coupling equations will not exist any longer. The effect of the metal contacts on the characteristics of the directional coupler could be greatly reduced by sputtering a thin layer of a dielectric on top of the directional coupler before the metal contact is made, as shown in Figure A-3. The dielectric layer should preserve the dielectric waveguide mode without greatly increasing the required electric voltage for switching.

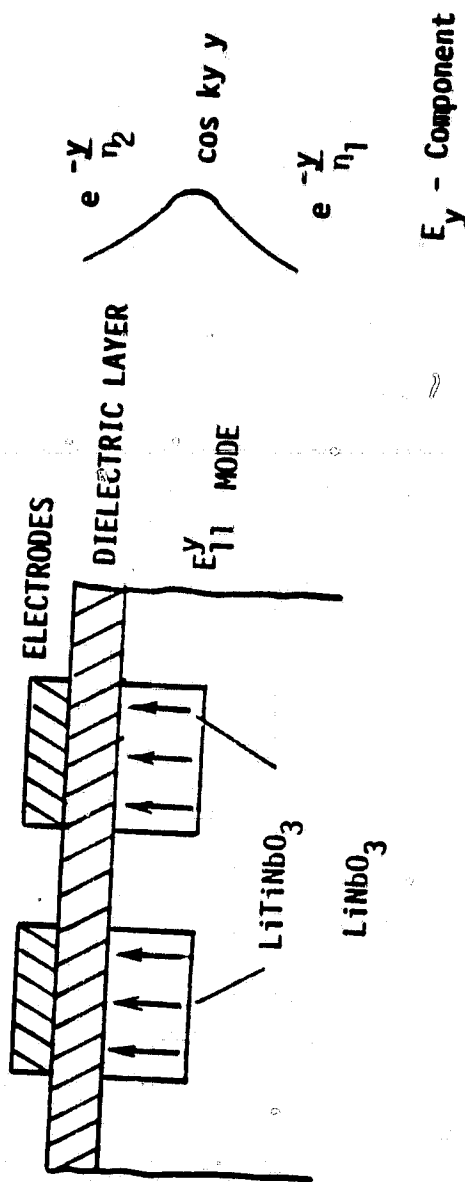


Figure A-3. Cross-section of Ti-Diffused LiNbO_3 Waveguide With Buffer Layer and Electrodes

In Figure A-4 the optical E_{11}^X - mode (TE) is excited, where the optical electrical field vector is perpendicular to the optical axis of the uniaxial LiNbO_3 crystal. This orientation of the electric field vector corresponds to the ordinary wave in the crystal. The change of the refractive index with the external electrical field is

$$n_{1,TE} = n_0 - \frac{n_0^3}{2} r_{13} E \quad A(3)$$

for LiNbO_3 where $n_0 = 2.26$ $\lambda = 0.8$ micron and $r_{13} = 10 \times 10^{-10}$ cm/volt.

The effect of the metal contact on the TE mode should be smaller than on the TM mode. This is because in the TE mode the optical electrical field vector is parallel to the metal contact. The change in the field distribution, introduced by the metal contact for the TE mode, should only affect the evanescent field component which is proportional to $\exp(-\frac{y}{n_2})$ by decreasing n_2 . Thus, it seems possible that the losses introduced by the metal contact for the TE mode are sufficiently small and will hardly exceed those of the substrate. In that case the general coupling equations would be valid for the TE mode. Also a dielectric layer between waveguide and metal contact could be added (Figure A-3) in order to mitigate the effect of the metal contact on the waveguide mode.

A1.1.2.2 Directional Coupler

The coupled mode equations between two parallel guides were derived for two incident waves, they are:

$$a(z,t) = A e^{j(\omega t - k_{z,a} z)}$$

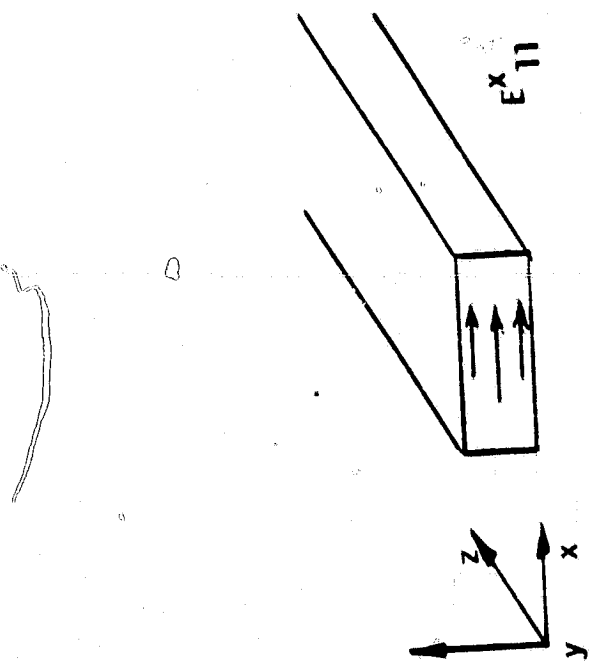


Figure A-4. Orientation of TE-Mode

and

A (4)

$$b(z, t) = B e^{j(\omega t + k_{z,b} z)}$$

The complex normalized amplitudes A and B of the incident waves are independent of z. In the directional coupler coupling between the evanescent regions of the two waves perturb the traveling waves and the complex amplitudes A and B become dependent of the propagation direction z. Then the coupled mode equations between two parallel guides become:

$$\frac{dA(z)}{dz} = -j \kappa B(z) e^{-2j\delta z}$$

A (5)

$$\frac{dB(z)}{dz} = -j \kappa A(z) e^{+2j\delta z}$$

where κ is the coupling coefficient, and $\delta = \frac{k_{z,a} - k_{z,b}}{2}$. By the substitution:

$$A = R e^{-j\delta z}$$

and

A (6)

$$B = S e^{+j\delta z}$$

the coupled wave equations become:

$$R' - j\delta R = -jkS$$

A (7)

$$S' + j\delta S = -jkR$$

The solution of Eq. A-7 in matrix form assuming that the input amplitudes at the beginning of the coupling region are R_0 and S_0 , is:

$$\begin{pmatrix} R \\ S \end{pmatrix} = \begin{pmatrix} A_1 & -j B_1 \\ -j B_1^* & A_1^* \end{pmatrix} \begin{pmatrix} R_0 \\ S_0 \end{pmatrix}$$

A (7a)

where the asterisk indicates a complex conjugate. The matrix coefficients are:

$$A_1 = \cos z \sqrt{\kappa^2 + \delta^2} + j\delta \frac{\sin (z \sqrt{\kappa^2 + \delta^2})}{\kappa^2 + \delta^2}$$

A(8)

$$B_1 = \frac{\kappa \sin (z \sqrt{\kappa^2 + \delta^2})}{\kappa^2 + \delta^2}$$

The propagation constant k_z in Eq. A-4 is given by Eq. A-12 together with Eqs. A-11, A-13 and A-14. The propagation constants $k_{z,a}$ and $k_{z,b}$ in the two guides under the influence of an external electric voltage follow from the same equations, where the refractive index n_1 is given by Eq. A-1 for the TM mode and by Eq. A-3 for TE mode. The coupling coefficient κ is given by Eq. A-10, it will also change when an electric voltage is applied to the waveguides because of the change in refractive index n_1 in Eqs 11 to 15.

For the synchronous case where $k_{a,z} = k_{b,z} = k_z$ and $\delta = 0$, complete power transfer from one guide to the other occurs when

$$A_1 = 0 \text{ (Eq. 8), that is for } z = \frac{2 v_0 + 1}{\kappa_0} \frac{\pi}{2}$$

where

$$v_0 = 0, 1, 2, 3$$

A (9a)

In the single section cobra switch the power will be transferred from one guide to the other when no external electrical field is applied.

For the asynchronous case no power will be transferred between the guides when $B_1 = 0$. This occurs when:

$$(\kappa_e^2 + \delta^2) L^2 = (v_e \pi)^2 \quad v_e = 1, 2, 3 \quad (9b)$$

In the single section cobra switch the coupling length L of the directional coupler is determined by Eq. 9a, where the shortest coupling length is

$$L = \frac{\pi}{2 \kappa_0}$$

For switching an external voltage must be applied until the relation in Eq. 9b is met. It is

$$(\kappa_e^2 + \delta^2) \left(\frac{1}{2} \kappa_e\right)^2 = 1$$

$$\text{For } \delta = \frac{\Delta k_z}{2}$$

$$\frac{\Delta k_z}{\pi} L \approx \sqrt{3}$$

A1.1.2.3 Coupling Coefficient

The length of the single section directional coupler for complete power transfer is strongly dependent on the coupling coefficient κ . It seems important therefore, to investigate the functional relation of the coupling coefficient and the characteristics of the cobra switch. The coupling coefficient between two channel waveguides with a width a , and thickness b and a separation between guide c , (Figure A-5) is

$$\kappa = 2 \frac{k_x^2}{k_z} \frac{\xi_2}{a} \frac{\exp(-\frac{c}{\xi_2})}{1 + \frac{k_x^2}{k_z^2} \frac{\xi_2^2}{c^2}} \quad A(10)$$

where for the TM mode (E_{11}^y)

$$k_x = \frac{\pi}{a} \frac{1}{\frac{1 + \frac{\lambda}{c}}{(n_1^2 - n_2^2)^{\frac{1}{2}} \pi a}} \quad A(11)$$

$$k_z = (k_1^2 - k_x^2 - k_y^2)^{\frac{1}{2}} \quad A(12)$$

$$k_1 = \frac{2\pi}{\lambda} n_1 \quad A(13)$$

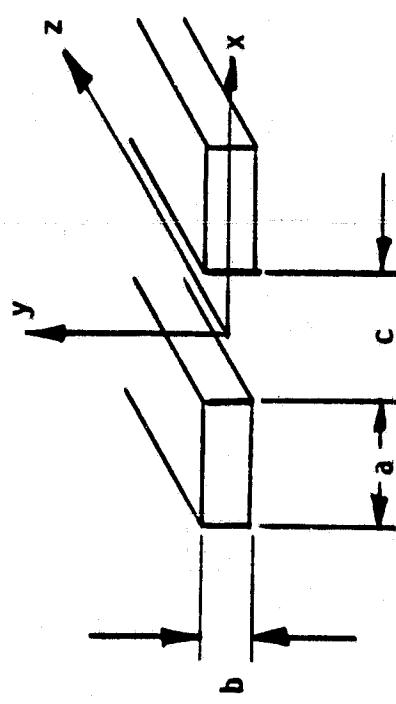


Figure A-5. Coupled Optical Channel Waveguides

$$k_y = \frac{\pi}{b} \frac{1}{1 + \left(\frac{n_3^2 \lambda}{2(n_1^2 - n_2^2)^{1/2}} + \frac{n_2^2 \lambda}{2(n_1^2 - n_2^2)^{1/2}} \right) \frac{1}{\pi n_1^2 b}} \quad A(14)$$

$$\xi_2 = \frac{\lambda}{2(n_1^2 - n_2^2)^{1/2} \pi} \left[\frac{1 - \left\{ \frac{2(n_1^2 - n_2^2)^{1/2}}{\pi} \frac{1}{1 + \frac{\lambda}{(n_1^2 - n_2^2)^{1/2} \pi a}} \right\}^2}{1 + \frac{\lambda}{(n_1^2 - n_2^2)^{1/2} \pi a}} \right] \quad A(15)$$

where n_1 is the refractive index of the guide, n_2 the refractive index of the substrate and n_3 the refractive index of the metal contact (For the TE mode similar equations were derived).

The coupling coefficient in Eq. A-10 will change primarily with dimensional changes, especially with changes in the spacing between guides. Since this dimension is of the order of 2 microns, the tolerances during the device fabrication for constant κ become too tight to be met. In reference 2 and 3 a cobra switch had been reported with alternating $\Delta\beta$ sections to accomplish voltage tuning also for the power transfer position of the cobra switch.

A1.1.2.4 Alternating $\Delta\beta$ Switch

In the alternating $\Delta\beta$ switch the coupling length L is divided into two equally long sections, their electric voltages are equal in magnitude but reversed in sign (Figure A-6). The assumption is made that in Eq. A-12, $k_z = k_1$, then $\Delta\beta$ is positive in one section and negative in the other section (Figure A-6). The transfer through the two sections is given by the multiplication of the matrix in Eq. A-7a with the corresponding matrix for the negative $\Delta\beta$. This is

$$\begin{pmatrix} A_2 - jB_2 \\ -jB_2^* A_2^* \end{pmatrix} = \begin{pmatrix} A_1 - jB_1 \\ -jB_1^* A_1^* \end{pmatrix} \begin{pmatrix} A_1^* - jB_1 \\ -jB_1^* A_1 \end{pmatrix} \quad A(16)$$

$$A_2 = 1 - 2B_1^2$$

$$B_2 = 2 A_1^* B_1$$

where the matrix elements given in Eq. A-8 are evaluated for $z=L/2$. For cross over, $A_2 = 0$, then $2B_1^2 = 1$ and from Eq. A-8.

$$\frac{\frac{k_e^2}{2}}{\frac{k_e^2}{2} + \delta^2} \sin^2 \left(\frac{L}{2} \sqrt{\frac{2}{k_e^2} + \delta^2} \right) = 1/2 \quad A(17)$$

For complete power transfer the external electric voltage must be varied until the relation in Eq. A-17 is met.

For straight through power transfer in the guides it is

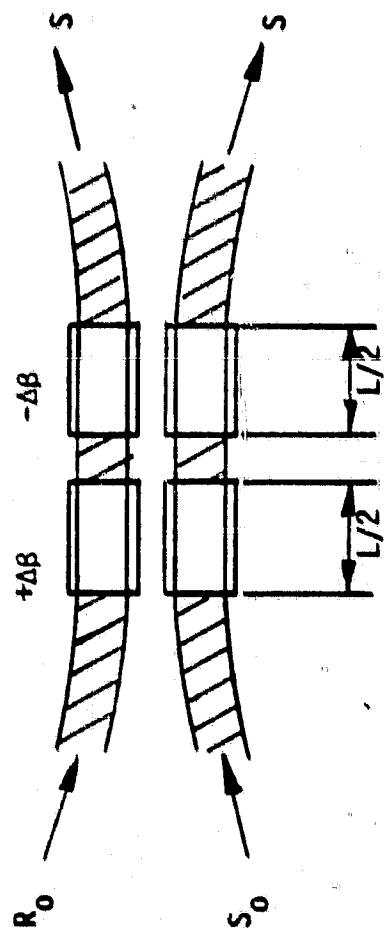


Figure A-6. Alternating $\Delta\phi$ Switch

required that $B_2 = 0$. This occurs when either $A_{11}^2 = 0$ or $B_{11}^2 = 0$.

The first condition implies that $\Delta\beta = 0$ and the second that

$$\left(\frac{L}{2}\right)^2 (\kappa_e^2 + \delta^2) = (v\pi)^2 \quad v = 1, 2, 3, \dots \quad (18)$$

$$(\kappa_e^2 + \delta^2) L^2 = 4 (v\pi)^2$$

To switch to straight-through power transfer the electric voltage must be changed until the relation in Eq. A-8 is met.

The alternating $\Delta\beta$ switch was implemented.

It is a two-section switch. The term κL was made

$\sqrt{2} \frac{\pi}{2}$, because it had been determined analytically that for this product of coupling coefficient times coupling length, the same voltage yields cross over for the reversed $\Delta\beta$ switch and straight through for the uniform (non revised $\Delta\beta$) switch, as shown in Figure A-7).

The question which needs to be answered numerically using Eqs. 10 and 18, is whether a two section cobra switch can be voltage tuned for optimum switching performance and maintain its performance over a certain temperature range. The numerically evaluation can be performed for LiNbO_3 (but not for titanium diffused LiNbO_3) where the temperature dependence of the refractive indices n_0 and n_e and of the electroptic coefficients r_{13} and r_{33} are published.

Also the approximations that $k_z \approx k_1$ and that the coupling coefficient does not change with the external electric field, must be checked to their validity.

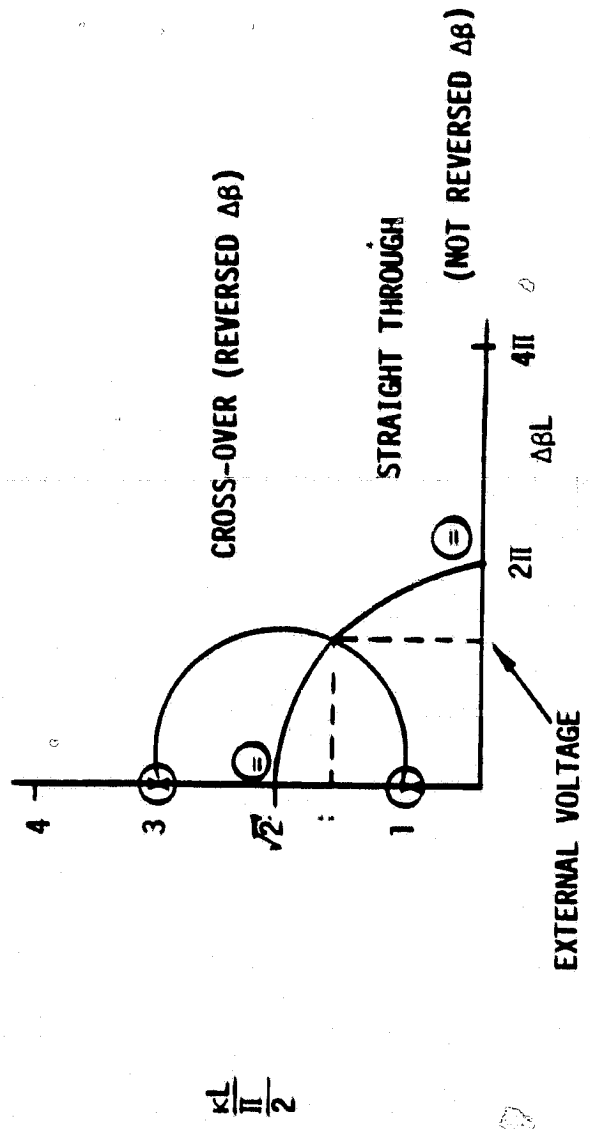


Figure A-7. Crossover of Alternating $\Delta\beta$ Switch

R.V. Schmidt and H. Kogelnik, Appl. Physics Letters, Vol. 28, No. 9,
1 May 1976, p. 503.

A1.1.2.5 Numerical Evaluation

To optimize the design of a cobra switch the electric field vector of the optical wave should be parallel to the extra ordinary wave of the LiNbO_3 crystal (E_{11}^y mode). This polarization minimizes the electric voltage required for switching from straight through to cross over. To maintain the E_{11}^y mode, the width of the channel waveguides (a) should be larger than its height. It seems important that the metal contracts are not placed directly on the channel waveguides, but that a thin dielectric layer of approximately 2 microns be inserted between the LiNbO_3 crystal with the channel waveguides, and the metal contacts, as shown schematically in Figure 3. The thin dielectric layer will confine the optical wave of the waveguides and of the substrate between the waveguides. It will accomplish that the field configuration of the dielectric waveguide mode is not affected by the metal contacts.

The coupling coefficient between the channel waveguides will be computed for the E_{11}^y mode, where the width of the channel waveguides is twice their height. The refractive index of their dielectric layer between waveguides and metal contact will be assumed to be the same as the refractive index of the substrate of $n_e = n_2 = 2.17$. The refractive index of the Titanium diffused LiNbO_3 will be assumed to $n_1 = 2.175$. The computation of the coupling coefficient will use Eqs. 10 to 18 and $\lambda = 0.8$ microns.

To insure that each guide only supports the fundamental mode (E_{11}^y) the normalized dimension is limited to

$$\frac{2b}{\lambda} (n_1^2 - n_2^2)^{\frac{1}{2}} \leq 0.8$$

This yields

$$b = 2.2 \text{ microns},$$

for

$$a = 2 b$$

$$a = 4.4 \text{ microns}$$

$$k_x = 0.51 \times 10^4 \quad k_y = 0.8 \times 10^4$$

$$k_1 = 17.08 \times 10^4$$

$$k_z = (k_1^2 - k_x^2 - k_y^2) \approx k_1 = 17.08 \times 10^4$$

$$\xi = 0.966 \times 10^{-4}$$

$$\eta = 1.2 \times 10^{-4}$$

where ξ and η are the penetration depth of the field into the adjacent dielectric with the refractive index n_2 .

Then $\kappa = 6.78 \text{ cm}^{-1}$ for 2 microns separation between guides.

For the alternating $\Delta\theta$ switch for cross-over $kL = \frac{\pi}{2} \sqrt{2}$
and $L = 0.27 \text{ cm}$. From Eq. 17, $\delta = 6.78 = \frac{kza - kzab}{2} = \frac{2\pi}{\lambda} \Delta n$
 $\Delta n = 0.863 \times 10^{-4}$.

$$\text{From Eq. 1, } \Delta n = \frac{n_e^3}{2} \quad r_{33} \quad E = \frac{n_e^3}{2} \quad r_{33} \quad \frac{V}{T}$$

For $n_e = 2.175$, $r_{33} = 32.2 \times 10^{-10} \text{ cm/volt}$, and a length of the electric field lines (e) of $(3.2 \pi + 4) \cdot 10^{-4} \text{ cm}$, $V = 7.34 \text{ volt}$.

For complete cross-over of the two section switch where each section is 0.164 cm long, a positive voltage of 7.3 volts must be applied to one section and a negative voltage of -7.3 volts must be applied to the other section.

For straight through power transfer Eq. 9b must be satisfied. To accomplish this the same voltage of 7.38 volts is applied to both sections of the switch.

When the temperature changes, the refractive index of LiNbO_3 and its electro-optic coefficient also change, the changes are $0.7 \times 10^{-4}/^\circ\text{C}$ and $4.9 \times 10^{-4}/^\circ\text{C}$, respectively. Assuming a temperature increase of 20° which will result in an increase of n_1 to 2.1764 and r_{33} to 32.2098. This causes a decrease in the coupling coefficient to 6.775 and an increase of δ to 0.6795. Both changes with temperature seem too small to affect the performance of the switch. However, should the temperature range become larger, consideration should be given that the temperature change of the ordinary wave is smaller than the temperature change of the extra ordinary wave. Consequently, operation of the switch in the TE mode would be less affected by temperature change than in the TM mode.

A1.1.2.6 Material

The cobra switch had been built of Titanium diffused LiNbO_3 . However, LiNbO_3 has shown refractive index inhomogeneities which would adversely affect the performance characteristics of the cobra switch. Considerations should be given to the use of LiTaO_3 or $\text{K}_6\text{Li}_4\text{NbO}_3$ which have not exhibited similar inhomogeneities.

A1.2 SWITCHING NETWORKS USING COBRA SWITCHES

In the switching network design in Figure A-8 the light is guided in channel waveguides and the DPDT electro optic switches are of the single section "Cobra" type. In the single section "Cobra" switch only the cross talk in the asynchronous mode can be reduced by voltage tuning. The cross talk in the synchronous coupling mode depends on the dimensional precision of the length and the distance between the coupled channel waveguides, which can not always be controlled. Therefore, the single section "Cobra" switch would work well in the switching matrix in Figure A-8 which is especially designed to compensate for leakage in switches where the cross talk is primarily in one coupling mode.

The drawback of this type of switching matrix is that it uses n^2 switches and each "Cobra" switch, whether in the synchronous (off) or in the asynchronous (on) coupling mode, introduces losses and scattering. Also, voltage tuning of the asynchronous mode of n^2 "Cobra" switches in the switching matrix must represent a serious problem.

In the alternating $\Delta\beta$ "Cobra" switch, both coupling modes can be voltage tuned to minimize cross talk. This type of switch can be incorporated into a switching network which need not compensate for excessive cross talk and therefore, requires no termination and a smaller number of switches. An optical switching network with four input and four output ports requiring 5 alternating $\Delta\beta$ switches is shown in Figure A-9. Because of the limited number of switches in the network, a connection between a particular pair of ports may block connection

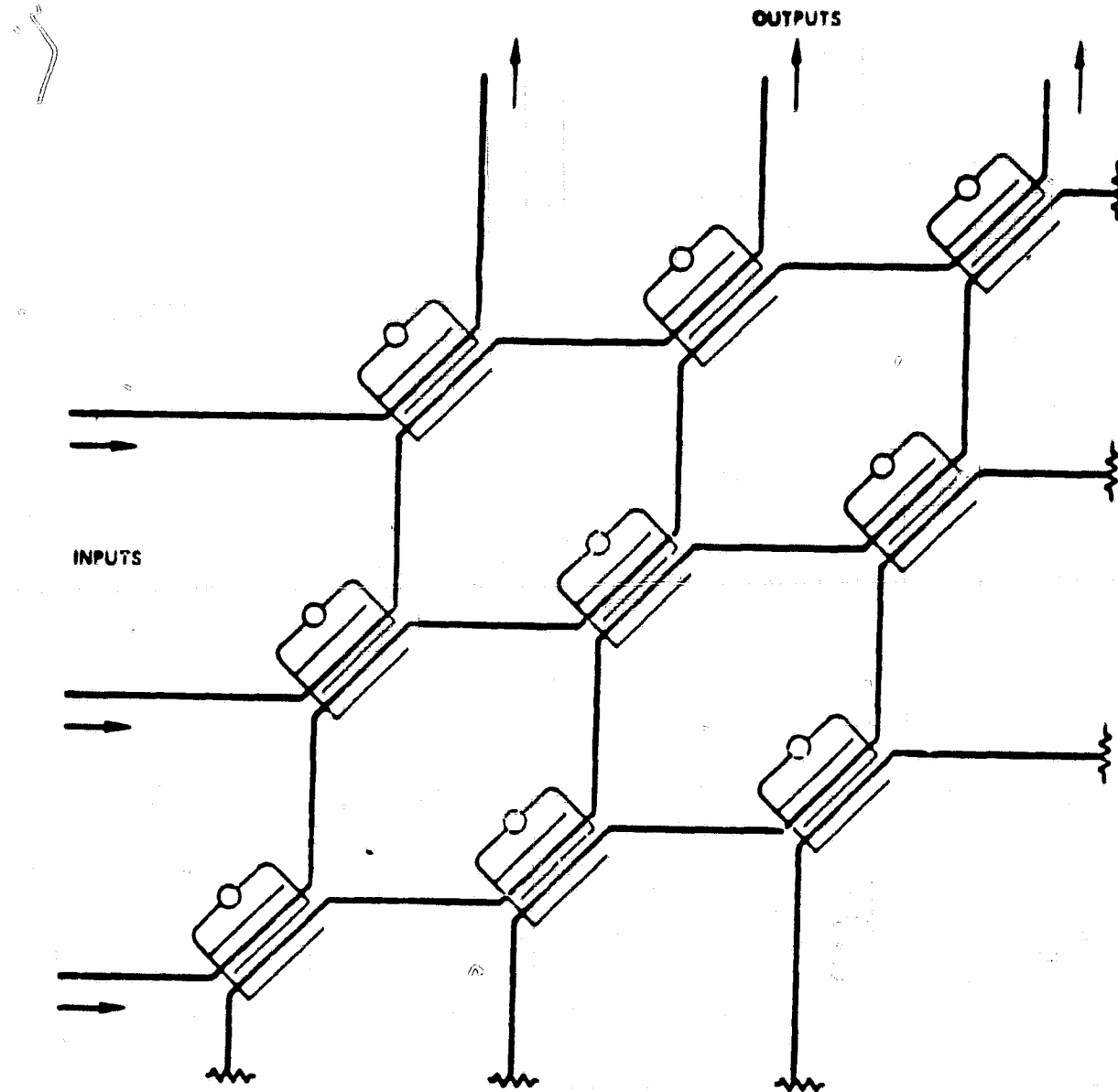


Figure A-8. Schematic of a Terminated $n \times n$ Optical Matrix ($n=3$) Utilizing Single Section "Cobra" Switches

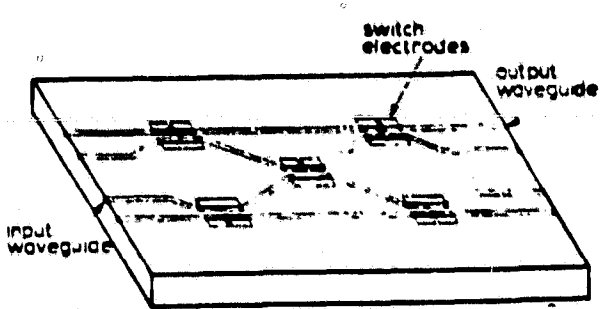


Figure A-9a. Representation of $n \times n$ Optical Matrix ($n=4$) Utilizing Alternating AB Cobra Switches

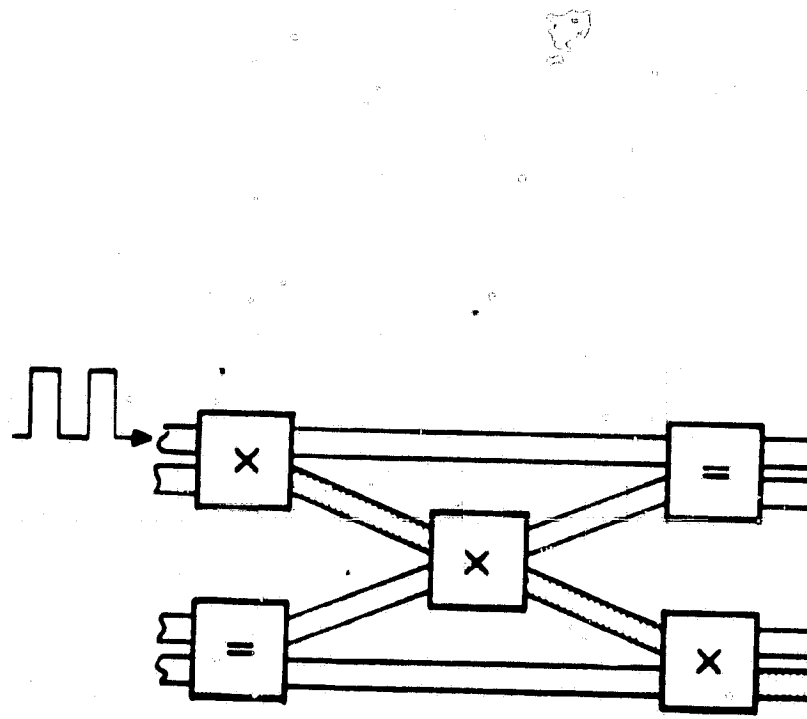


Figure A-9b. Typical Connection

between another pair of ports. While adjustment of the voltage for minimum cross talk in a single alternating $\Delta\theta$ switch is straightforward, it must require much more complicated adjustments when 5 integrated switches or more are used in the network.

The study to find the optimum design for a comparatively large integrated optic switching network seems to favor the switching network using electro optic Bragg diffraction switches in planar waveguide where attenuation, cross talk and distortion should be very low, rather than using "Cobra" switches.

A1.2 ACOUSTO-OPTIC BRAGG DIFFRACTION SWITCH

A1.2.1 Introduction

Acousto-optic devices can be used to switch light from one port to n ports, where $n = 2$. In their use as light switches they can be either operated in the isotropic or in the anisotropic mode. In the isotropic mode, the polarization of the undiffracted optical wave and the diffracted optical wave is the same. The direction of the diffracted optical wave always differs from the direction of the incident optical wave. In their use as light switches advantage is taken of the property that the direction of the diffracted optical wave can be deflected by a change in the acoustic frequency. In the isotropic mode there is no limitation to the acoustic frequency other than set by the generation of acoustic waves and their attenuation at room temperature. In this mode isolation between the n output ports is determined by the beam properties of the diffracted light.

To increase the number of output ports while maintaining isolation between ports, an array of interdigital acoustic-wave transducers should be used.

In the anisotropic mode the polarization of the undiffracted and the diffracted optical wave is orthogonal, so that large isolation can be achieved by polarization discrimination. This large isolation, however, is effective only for switching from one port to either of two ports. When switching from one port to n ports ($n > 2$), the acoustic frequency must be varied to change the deflection of the diffracted optical light beam. In the anisotropic mode the acoustic frequency has a lower limit where the

undiffracted and the diffracted optical waves become collinear. An upper frequency limit occurs where the isotropic Bragg diffraction begins to dominate. Close to the upper limit, where the direction of the diffracted light is normal to the acoustic wave vector, the deflection range of the diffracted optical wave becomes very large. In this acoustic frequency range a light switch should be operated to switch from one port to n ports for $n \gg 2$.

In the anisotropic mode for $n > 2$ the isolation between the output ports is also determined by the beam properties of the diffracted light.

It is important to realize that an acousto-optic device can never function as a switch alone. The wave nature of the sound beam periodically moves the optical beam from the direction of the undiffracted wave to the direction of the diffracted wave. This effect results in intensity modulation of the optical waves at the frequency of the acoustic wave. In a communication system care must be taken that the acoustic frequency lies outside the information frequency band.

1.1.2 Operation Principle

Acousto-optic interactions in solids are due to the photo-elastic effect where mechanical strains set-up by the acoustic waves cause a change in the refractive index Δn . The strain and therefore the refractive index variation is periodic with a wavelength equal to that of the acoustic wave Λ . The variation of the refractive index can affect the phase of the light beam, which traverses the strained medium. However, the variation of the refractive index by the photo-elastic effect is only in the order of 10^{-4} . For appreciable phase modulation the interaction length must be increased by approximately $\lambda_0/\Delta n$, where λ_0 is the optical wavelength.

Efficient acousto-optic devices use parametric interaction of traveling optical waves. The optical waves are coupled by the acoustic wave, which changes the refractive index by an amount proportional to the strain produced by the acoustic wave. For sound waves with frequencies in the hundreds of MHz region and below, the interaction in the Bragg region is most efficient. In this region the optical phase grating set up by the periodic index changes can diffract all the incident light into a single 1st order diffraction lobe. The condition for Bragg diffraction is that

$$w > \frac{n\Lambda^2}{\lambda_0}$$

where w is the width of the acoustic beam, Λ is the acoustic wavelength, and λ_0 is the free space optical wavelength.

Optimum coupling will occur if the wave vectors k of the three waves and their frequencies ω satisfy the phase match conditions, which are

$$k_1 = k_2 + k_s \quad (1a)$$

$$\omega_1 = \omega_2 + \omega_s \quad (1b)$$

where the indices 1 and 2 refer to the incident and the diffracted optical waves and s to the sound wave. For the isotropic mode, the vector diagram for Bragg diffraction is shown in Figure A-10. The vector components can be written as

$$k_1 \cos \theta_1 = k_2 \cos \theta_2$$

$$k_1 \sin \theta_1 + k_2 \sin \theta_2 = k_s$$

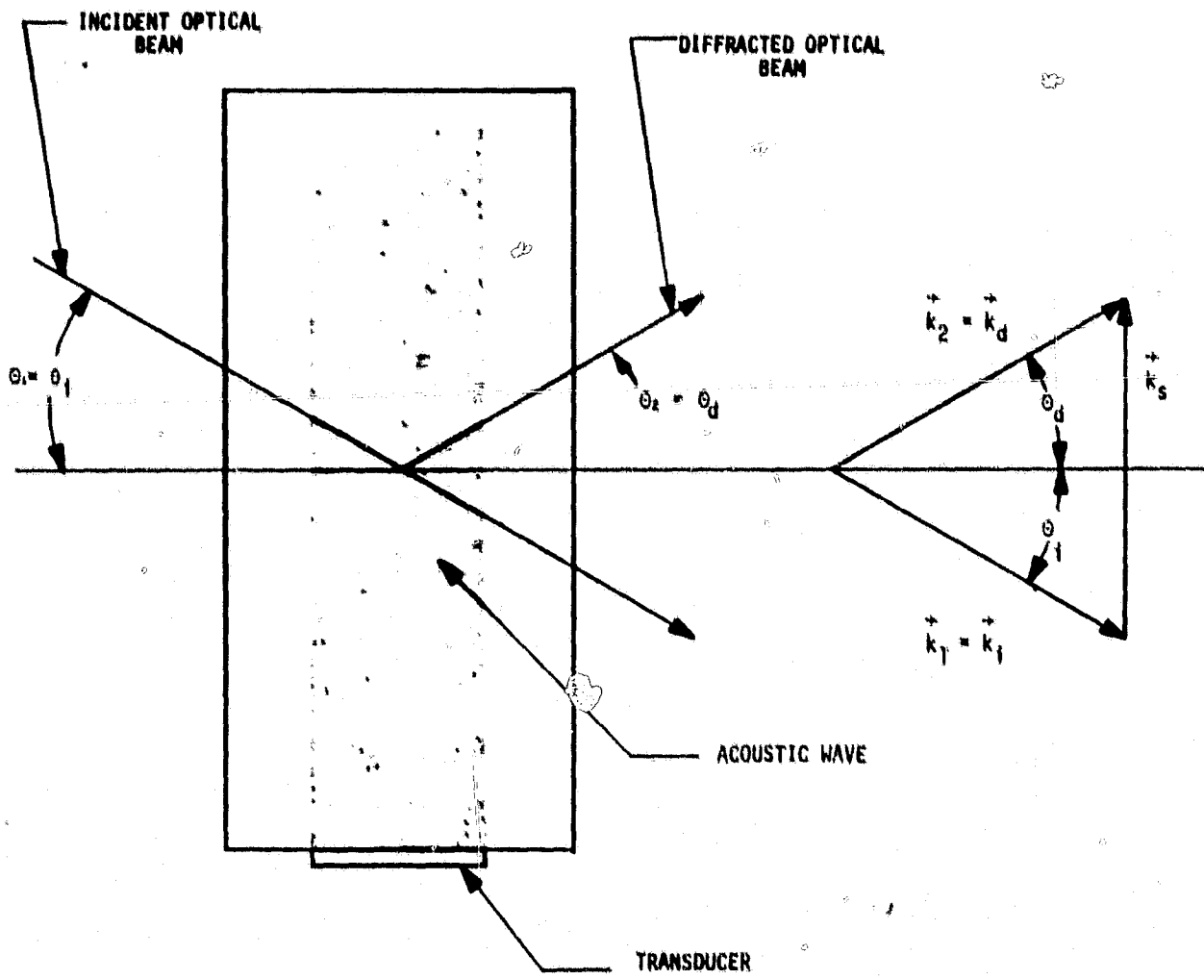


Figure A-10. Normal Bragg Diffraction Geometry

Since the polarization of the incident optical wave and the diffracted optical wave are the same, $n_1 = n_2$, and

$$\frac{\cos \theta_1}{\cos \theta_2} = \frac{k_2}{k_1} \approx 1$$

and $2k \sin \theta_0 = k_s$ which yields the Bragg angle θ_0

$$\theta_0 = \sin^{-1} \frac{\lambda}{2\Lambda} = \sin^{-1} \frac{\lambda_0}{2nv} f_s \quad (2)$$

where λ is the optical wavelength in the diffracting medium, v is velocity of the acoustic wave and f_s is the frequency of the acoustic wave which is much lower than the frequency of the optical wave, v_0 .

The Bragg angle θ_0 is the angle of the incident optical wave and twice the Bragg angle, $2\theta_0$, is the difference in direction of the incident and the diffracted light. For $f_s \ll v_0$, the Bragg angle is very small so that the light is incident on the acoustic columns at an angle θ_s which is nearly normal to the acoustic wave vector. Also the diffracted wave is Doppler-shifted by the traveling acoustic wave to the frequency

$$v_0 + f_s \text{ or } v_0 - f_s.$$

For a change of the acoustic frequency Eq. 1b will remain valid since the diffracted light will shift in frequency to maintain a value $\omega_1 = \omega_s$. However, the wave vectors will not sum. A change of the acoustic frequency by Δf_s yields an equivalent change of Δk_s ; then Eq. 1a becomes

$$\vec{k}_1 = \vec{k}_2 + \vec{k}_s + \vec{\Delta k}_s$$

and the difference in direction between the incident and the diffracted light increases by

$$\Delta(2\theta) = \sin^{-1} \frac{\lambda_0}{nv} \Delta f_s \quad (3)$$

To operate an acousto-optic device as a switch advantage can be taken of the change of the direction of the diffracted light with the variation of the acoustic frequency. However, a deviation from the phase match condition in Eq. 1a, also results in a decrease in intensity of the diffracted light, which can be represented by

$$P(\Delta k_s) \approx \frac{\sin^2 \left(\frac{\Delta k_s}{2} L \right)}{\left(\frac{\Delta k_s}{2} L \right)^2} \quad (4)$$

where L is the interaction length of the optical and acoustic waves,

$L = w \tan \theta$, and w is the width of the sound wave. The range of the frequency change for deflecting the incident light beam and consequently, the number of output ports is limited by Eq. 4.

Allowing a decrease in intensity by -4 db, the total frequency deviation becomes

$$2\Delta f_s = 2 \frac{v\lambda}{w\Delta}$$

and the deflection angle range becomes

$$\pm \Delta(2\theta)_{\max} = \pm \frac{\lambda_0}{n^2} \frac{1}{wv f_s}$$

The number of output ports of a multiport switch is also limited by the required isolation between ports. The deflected beam results from the diffraction of the incoming beam at the phase grating, which is set up by the acoustic wave. The diffraction of a plane wave by a grating is the product of two functions, one of them represents the effect of a single period of the grating, the other represents the effect of the interference of light from all the illuminated periods of the grating.

Each single period of the grating effectively represents a reflector to the incoming wave. The length of its apertures is given by the width of the acoustic wave projected in the direction of the incident optical wave given as

$$s = w \sin \theta \quad (5)$$

In the far-field the beam width corresponding to this aperture (the first minimum on each side of the beam) is

$$\Delta\phi = \frac{2^2 \lambda_0}{w \sin \theta} \quad (6)$$

The incident optical beam with the diameter D illuminates N acoustic

wave periods, where $N = \frac{D}{\Lambda}$. In the far-field, the width of the interference function set up by the N periods (the first minimum to each side) is

$$\Delta\theta = \frac{2\lambda_0}{D} \quad (7)$$

The interference maximum are spaced $\frac{\lambda_0}{\Lambda}$ apart.

Because the Bragg angle θ_0 is very small the beamwidth of the diffracted beam is determined primarily by Eq. 7. However, Eq. 7 only defines the beamwidth within the first minima. But the sidelobes outside the first minima can not be neglected. The first set of sidelobes outside the beamwidth given in Eq. 7 are only 13 db below the main beam for uniform illumination. The sidelobe level gradually decreases to lower levels for higher order sidelobes. For adequate isolation between adjacent output ports, the output ports must be spaced further apart than indicated by the beamwidth in Eq. 7.

The number of output ports limited by Eq. 4 can be made larger by using an array of interdigital transducers rather than a single transducer, as shown schematically in Figure A-11. The transducers have different center frequencies and generate acoustic beams that are tilted in respect to each other to meet the Bragg condition in Eq. 2.

If the diffracted optical polarization differs from the incident wave, in the anisotropic medium, the optical birefringence requires that $|k_d| \neq |k_i|$. As an example, a positive uniaxial crystal is considered in which an extra-ordinary polarized optical wave is incident perpendicular to the optical axis, and the acoustic wave is assumed to be propagating perpendicular to the optic axis. The photoelastic interaction is such that the diffracted wave is polarized in the direction of the ordinary wave. The phase match condition for traveling wave interaction is the

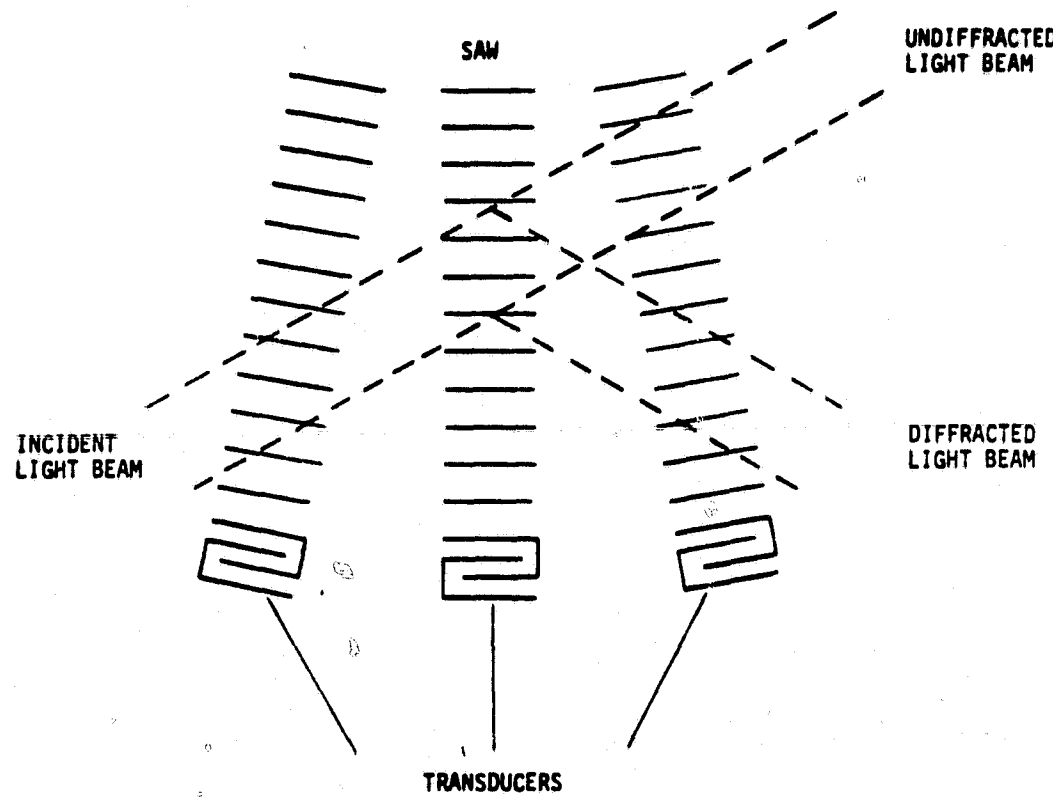


Figure A-11. Guided Wave Bragg Diffraction-Three Tilted Surface Acoustic Waves

same as given in Eqs. 1a and b. For $n_i \neq n_d$ the vector relation is given by

$$\sin \theta_i = \frac{\lambda_0}{2n_i \Lambda} \left[1 + \frac{\Lambda^2}{\lambda_0^2} (n_i^2 - n_d^2) \right] \quad (8)$$

$$\sin \theta_d = \frac{\lambda_0}{2n_d \Lambda} \left[1 - \frac{\Lambda^2}{\lambda_0^2} (n_i^2 - n_d^2) \right]$$

where the subscripts i and d denote incident and diffracted wave, respectively. The definition of positive θ_i and θ_d are shown in Figure A-12. Eqs. 8 written as functions of the acoustic frequency f_s become

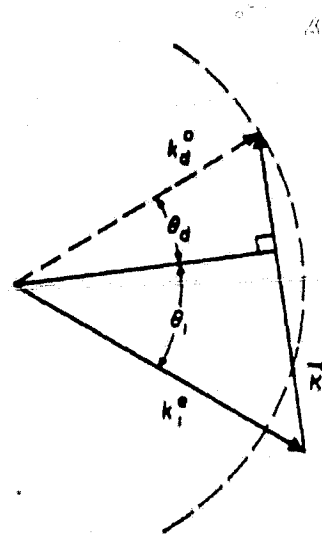
$$\sin \theta_i = \frac{\lambda_0}{2n_i v} \left[f_s + \frac{v^2}{f_s \lambda_0^2} (n_i^2 - n_d^2) \right] \quad (9)$$

$$\sin \theta_d = \frac{\lambda_0}{2n_d v} \left[f_s - \frac{v^2}{f_s \lambda_0^2} (n_i^2 - n_d^2) \right]$$

Large isolation between two output ports can be achieved with an acousto-optic switch when operating in an anisotropic mode. The large isolation between the two output ports is obtained by polarization discrimination. But to switch from one port to n ports ($n > 2$) in the anisotropic mode, the acoustic frequency must be varied to change the deflection of the diffracted optical wave.

In the anisotropic mode the acoustic frequency has a lower limit f_{\min} where the undiffracted and the diffracted optical waves are collinear given as

$$f_{\min} = (n^e - n^0) \frac{v}{\lambda_0}$$



(C. S. Tsai, SPIE
East 1978).

Figure A-12. Wavevector construction describing Bragg diffraction at frequency $v_d = v_i + f_s$ in a positive uniaxial crystal when the incident optical wave is extra-ordinarily polarized

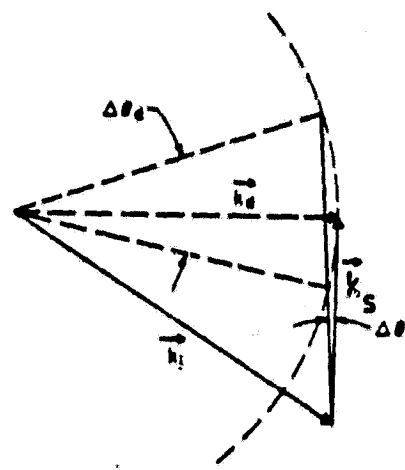
In the anisotropic mode the acoustic frequency has an upper limit noted in Eq. 9 to result when f_s becomes much larger than the second (anisotropic) term. In this case the isotropic mode tends to dominate.

At the acoustic frequency f' where

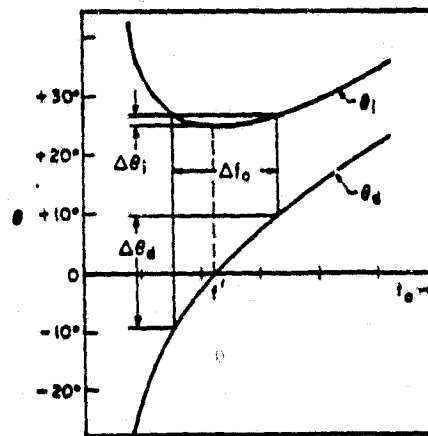
$$f' = \frac{v}{\lambda_0} \sqrt{n_i^2 - n_d^2} \quad (10)$$

the two terms in Eqs. 9 are equal and the deflection range of the diffracted optical wave becomes very large. For operation near the acoustic frequency $f_s \approx f'$ the wave vector diagram is shown in Figure A-13. For $f_s = f'$, $\theta_d = 0$ the vector k_s is tangent to the locus of allowed solutions of k_d . The change of θ_i and θ_d with a variation of the frequency f_s follows from Eq. 9. While the angle θ_i changes slowly, the angle θ_d changes very fast away from $\theta_d = 0$, as shown schematically in Figure 1-4. Actually, the deflection range in the anisotropic mode where $f_s \approx f'$, is close to 10 times the deflection range for isotropic Bragg diffraction.

An acousto optic switch from one port to n ports ($n \gg 2$) should operate in the anisotropic mode where $f_s \approx f'$. The large deflection range will make it possible to space the output ports sufficiently far apart to achieve large isolation among them.



a.
Figure A-13. Wave vector construction illustrating Bragg diffraction near the acoustic frequency $f_s = f'$. The angular scan $\Delta\theta_d$ is much larger than the diffraction angle $\Delta\theta_i$ of the incident acoustic beam.



b.
Figure A-13. Graph of angles of incidence and diffraction for Bragg diffraction near the acoustic frequency $f_s = f'$. The large angular sweep $\Delta\theta_d$ obtainable with a small incident diffraction angle $\Delta\theta_i$ is illustrated.

A1.1.3 Implementation

A.1.1.3.1 Acousto Optic Switch - Single Pole Double Throw (SPDT)

The design of a light switch for a communication system must consider the requirement for large isolation between the output ports. To accomplish large isolation in an acousto-optic switch which connects alternatively one port to two output ports, the two output ports should not correspond to the diffracted and the undiffracted beam. This restriction results because the incident light is being diffracted by the periodic index variations produced by the acoustic wave and both the diffracted and the undiffracted light intensities follow the envelope of the acoustic wave. Their variations are in-phase and out-of-phase, respectively, with the acoustic modulation wave. Thus, with the acoustic power being turned on, the switch can only function as a periodic 3 db coupler between the ports corresponding to the diffracted and the undiffracted beams. (It can also function as a periodic power divider with variable power division from 0 to 3 db by changing the acoustic power)

For a proper design, the two output ports of an acousto-optic switch should both correspond to symmetrical deflections of the diffracted beam from the phase matching direction. The angular dependence of the diffraction efficiency is given by

$$\eta = \frac{\sin^2(\frac{1}{2} k_s L \Delta\theta)}{(\frac{1}{2} k_s L \Delta\theta)^2} \quad (1)$$

where $\Delta\theta$ is the excursion from the Bragg angle, L is the acoustic beamwidth and k_s is the acoustic wave vector. At the half power points of Eq. 1

$$\frac{1}{2} k_s L \Delta\theta \approx 0.45 \pi$$

and the half power points appear at the angles $\pm \Delta\theta = \pm 0.45 \frac{\lambda}{L}$. This corresponds to the deflection of the diffracted beam from the phase matching condition by

$$\pm 2 \Delta\theta = \pm 0.9 \frac{\lambda}{L} \quad (3)$$

Using the relation for the Bragg diffraction

$$\sin \theta_0 = \frac{\lambda_0}{2n\lambda} = \frac{\pi f_s}{nv k_0} \quad (4)$$

and

$$\cos \theta_0 \Delta\theta_0 = \frac{\pi \Delta f_s}{nv k_0}$$

we obtain the required frequency change for the deflection in Eq. 3.

$$\pm \Delta f_s = \pm 0.9 \frac{n k_0 v^2 \cos \theta_0}{2\pi f_s L} \quad (5)$$

For large isolation between the two output ports the deflection of the diffracted beam from the phase matching condition, $2\Delta\theta$, must be larger than the beamwidth of the diffracted optical beam which is

$$\Delta\theta = \frac{2\lambda_0}{D} \quad (6)$$

where D is the diameter of the incident optical beam.

Also, for the design of an acousto-optic switch the switching speed is an important parameter. The switching speed is limited by the transducer bandwidth Δf_t and by the acoustic transit time across the optical beam. The switching time τ can be given as

$$\tau \leq \frac{1}{\Delta f_t} + \frac{D}{v} \quad (7)$$

The intensity of the diffracted guided light beam I_d in respect to the undepleted incident beam intensity I_i is given by

$$\frac{I_d}{I_i} = \sin^2 \left(\frac{\pi}{\lambda_0 \cos \theta_0} F \sqrt{\frac{M_2}{2}} P_{ac} \frac{L}{H} \right) \quad (8)$$

where θ_0 is the Bragg angle for phase matching condition, L is the acoustic beam width, F is the overlap integral which has a value from 0 to 1, depending on the transverse field distribution of the guided optical waves and the acoustic surface wave, and

$$M_2 = \frac{n^6 p^2}{\rho v^3}$$

where n is the refractive index, p the effective photoelectric constant, ρ the density, v the velocity of the acoustic surface wave and H is the acoustic beam height.

For the total conversion of the incident beam to the diffracted beam, the expression inside the parenthesis in Eq. (1) must be $\frac{\pi}{2}$. Total conversion of the incident light beam to the diffracted light beam can be accomplished by adjusting the input acoustic power.

The design of an acousto-optic integrated switch in the isotropic mode is shown schematically in Figure A-14 the crystal is a y - cut planar of LiNbO_3 with the optical axis (z-axis) orientated along the propagation direction of the acoustic wave. The optical waveguide is formed by in-diffusion of Ti. The waveguide can confine the guided light to within less than 2 microns of the surface.

For an efficient switch the acoustic frequency should be sufficiently high so that the confinement of the optical waves matched the penetration depth of the surface acoustic wave. This can be approximated for an acoustic center frequency of 1 GHz where the wavelength of the acoustic surface wave is close to 3.5 microns.

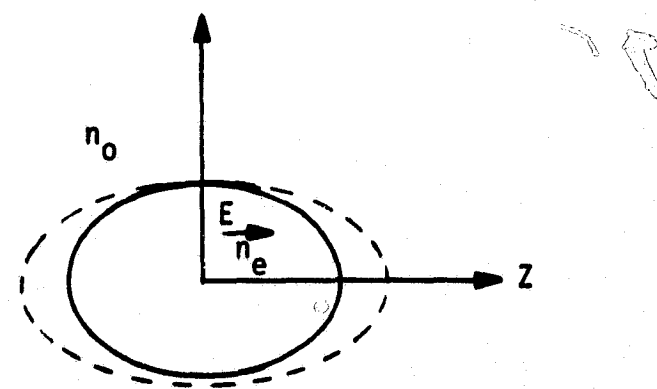
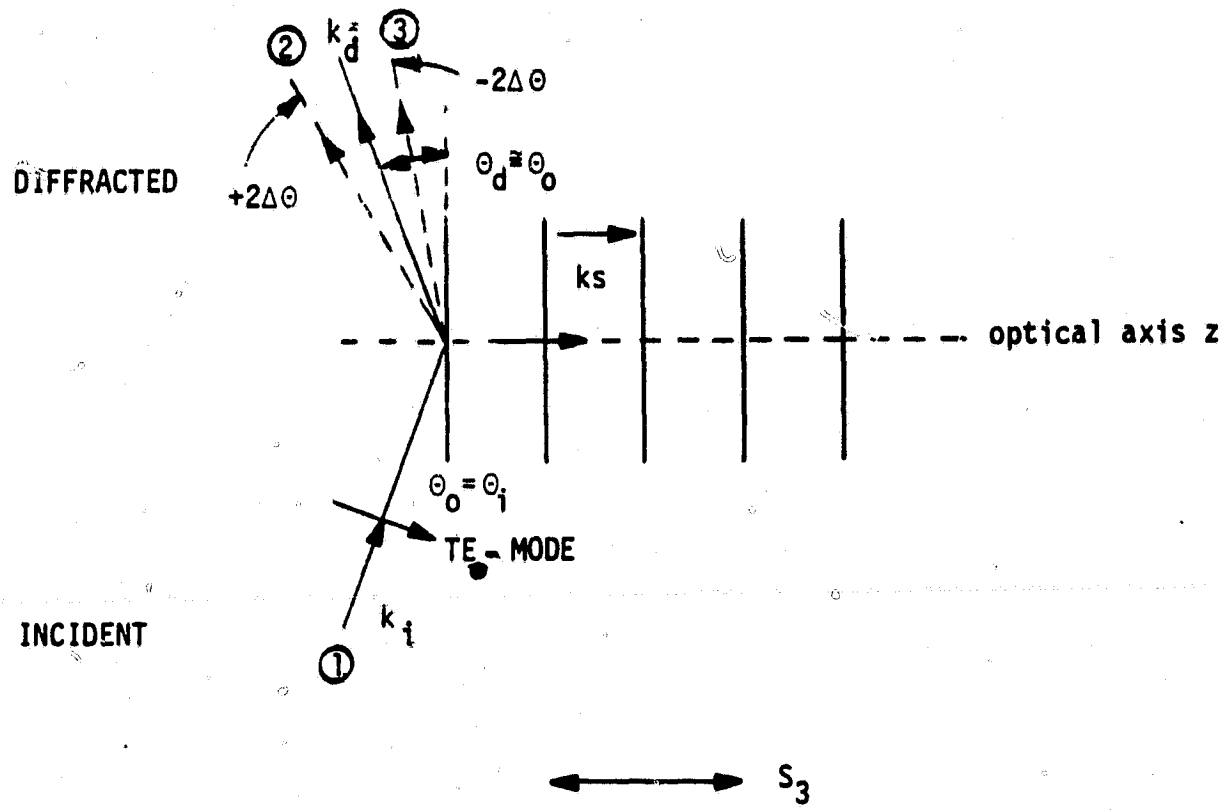


Figure A-14. (a) Single Pole Double Throw (SPDT) Acousto-Optic Switch
 (b) Photo Elastic Effect for an Applied Strain S_3

The incident optical beam from a He-Ne laser is at $\lambda_0 = 0.633$ microns. The guided optical wave is in the TE_0 mode where the electric field vector is polarized in the direction of the extraordinary ray, in order to take advantage of the larger induced index change in the extra-ordinary index.

The laser beam must be incident under the Bragg angle in Eq. 4, which is

$$\theta_0 = 45 \text{ milliradian}$$

The two output ports of the acousto-optic switch correspond to the angle $\theta_0 + 2\Delta\theta$ and $\theta_0 - 2\Delta\theta$. For these deflections of the diffracted optical beam the frequency of the acoustic wave must be switched from $fs + \Delta f$ to $fs - \Delta f$.

For a diameter of the incident optical beam of 1 mm, the beam-width of the diffracted beam to the first minima in the diffraction pattern, from Eq. 6, is

$$\Delta\theta = 1.2 \text{ milliradian}$$

Consideration must be given to the Gaussian field distribution of the incident laser beam which yields a diffracted beam with low sidelobes. Still, to assure large isolation between output ports, the two beam positions should be separated by at least $4\Delta\theta = \frac{6\lambda_0}{D} = 3.6 \text{ milliradian}$.

For this deflection, using Eq. 3, a width of the acoustic wave of $L = 1.75 \text{ mm}$ is required. This width meets the requirement for the Bragg condition that the term $\frac{2\pi\lambda_0 L}{n\Lambda^2}$ be larger than 10. In fact, $\frac{2\pi\lambda_0 L}{n\Lambda^2} = 282$.

The frequency deviation is $\pm \Delta f$ to accomplish the deflection from the phase matching condition of $\pm 2\Delta\theta$, from Eq. 5, is $\pm 20 \text{ MHz}$.

The acoustic power requirement for depleting the incident optical beam and forming the throughput to one of the output ports follows from Eq. 8, where the figure of merit for LiNbO_3 is $M_2 = 7 \times 10^{-18} \text{ sec/g}$. To use these cm-g-sec units, 1 mW must be expressed in the same units, where $1 \text{ mW} = 10^4 \frac{\text{g cm}^2}{\text{sec}^3}$. Then the required acoustic power assuming the overlap-integral $F = 0.4$, is 360 mW.

The speed of switching from Eq. 7 is

$$\tau = \frac{1}{40 \cdot 10^6} + \frac{0.1}{3.5 \times 10^5} = 0.3 \times 10^{-6} \text{ sec.}$$

In order to reduce the acoustic power requirement the width of the acoustic wave should be made larger. Assuming $L = 7 \text{ mm}$, then the acoustic power becomes 180 mW. However, the increase in the surface wave aperture reduces the deflection angle to $\pm 2\Delta\theta = \pm 0.45$ milliradian and requires an increase in the optical beam diameter to 4 mm.

Then $\Delta\theta = 0.3$ milliradian. The speed of the switch reduces to

$$\tau = \frac{1}{10 \times 10^6} + \frac{0.4}{3.5 \times 10^5} = 1.2 \times 10^{-6} \text{ sec.}$$

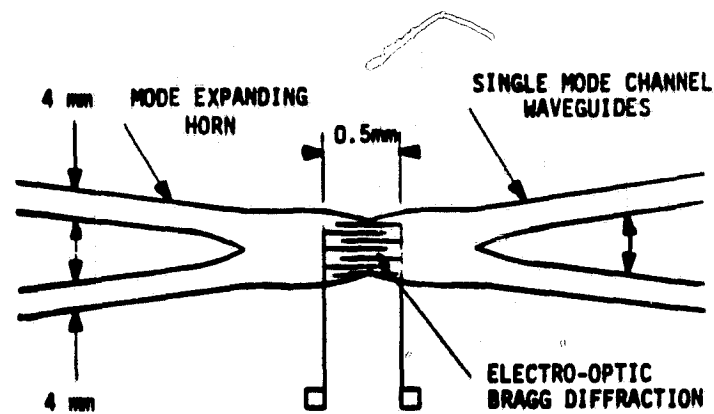
To extend the acousto optic switch in Figure A-14 to n ports where $n > 2$, the bandwidth of the device must be made larger. This can be accomplished in the isotropic mode by the use of an array of transducers. Or the acousto optic multi-port switch can be operated in the anisotropic mode where $f_s \approx f'$ as outlined in Section A1.2.

The acousto optic Bragg diffraction switch can attain large isolation when connecting one input port alternately to two output ports only when the two output ports correspond to symmetrical deflections of the diffracted beam from the phase matching condition. Thus, the acousto-optic Bragg diffraction switch induces a phase grating in the "on" as well as in the "off" position (with different periodicity).

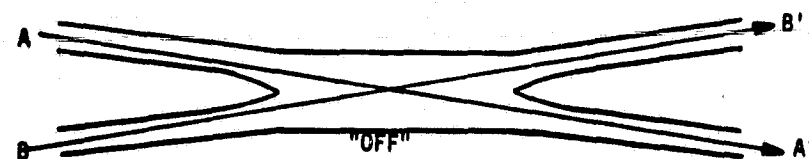
In a switching matrix the acousto-optic Bragg diffraction switches will introduce to the propagating waves scattering and losses in the "on" as well as in the "off" position.

A1.1.3 Electro optic Bragg Diffraction Switch in the Channel Waveguide

An electric optic Bragg diffraction switch has also been reported using channel waveguides. The design is a hybrid between guided transmission at the input and output ports and free space interaction at the diffraction grating. For the free space interaction, the channel waveguide must be increased in width from 4 to 30 microns so that the laser beam can intercept 10 periods of the diffraction grating as shown in Figure A-15. This design does not have the advantage that the wave can propagate without scattering in the "off" position of the switch.



(A)



(B)

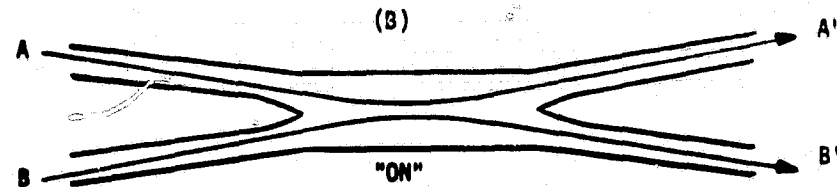


Figure A-15. Channel Waveguide Bragg Diffraction Switch
 (a) Schematic Illustration
 (b) Operation Status

B. Chen and C. M. Meier
 Applied Phys. Letters
 33 (1), 1 July 1978

A1.1.4 Switch Comparison

Three types of switches have been analyzed. They are the 2x2 "Cobra" switch, the 2x2 electro-optic Bragg diffraction switch and the 1xn, acousto optic Bragg diffraction switch (where $n > 2$). The 2x2 switches represent the building blocks for large switching matrices. The 1 x n switch would be used primarily in time-division multiplexing to connect n information channels to one guided output line and retrieve the n channels from one guided input line.

The 2x2 "Cobra Switch" uses the electrooptic effect, its energy consumption is low and isolation between ports up to 26 db has been demonstrated on a 2x2 two section switch. The electro optic switch requires energy primarily for switching rather than for holding in the "on" or "off" position. The equivalent lumped circuit element of the Cobra Switch is that of a capacitance. Energy is required primarily to charge up the capacitance, the energy to hold the charge on the capacitance is much smaller. Specific values were given for a six-section "Cobra Switch" where the design uses 3 volts d-c bias for the "cross-over" state and a pulse amplitude of 3.3 volts for the "straight through" state. The resistance of the input transmission line was 50 ohms and the capacitance of the device 22pF.

The energy to charge up the capacitance is

$$E = C \frac{V^2}{2}$$

$$E = 10^{-10} \text{ W sec}$$

The time to charge up the "Cobra Switch" is

$$T \approx \pi CR \approx 4 \times 10^{-9} \text{ sec}$$

Should the switch be turned on and off i.e. 10^6 times per second, then the energy required would be 0.11 mW sec.

In a switching matrix where i.e. 10 of these switches are used the switching energy would increase to 1 mW.

The electro optic Bragg diffraction switch also has low energy consumption, the required switching energy should be about the same magnitude as in the "Cobra" switch. But the reported values of isolation between ports are considerably lower than for the "Cobra" switch.

In the acousto optic switch energy is not required to switch but to hold the switch in the "on" and "off" positions. The required energy is approximately 450 mW sec (assuming 5 db transducer loss). The required energy is independent how often the switch is turned on or off. Also the required energy remains the same when the number of output ports is increased by using an array of transducers.

Isolation between ports of 25 db should be obtainable.

A1.3 COUPLERS FOR INTEGRATED OPTICS

A1.3.1 Introduction

The prism coupler and the grating coupler have both been devised for the conversion of a collimated laser beam into a surface wave and its reciprocal operation, that is the conversion of a surface wave into an outgoing collimated laser beam. But these couplers can not efficiently transform the wide angle radiation from an injection laser into the guided mode of a dielectric waveguide. For efficient coupling using one of these couplers the radiation from the injection laser must be collimated, preferably by a set of microlenses.

The tapered thin-fiber waveguide coupler which converts a guide wave into a divergent output beam, seems to lend itself well (in the reciprocal operation) to couple the radiation from an injection laser directly into a guided surface wave.

A1.3.2 PRISM Coupler

The prism coupler provides an efficient technique for coupling a collimated laser beam into a dielectric waveguide. It uses the principle of distributed mode coupling between the fields in the prism and the guide. The coupling occurs between the evanescent fields in the small gap of lower refractive index between the prism and the waveguide. The coupler permits excitation of the fundamental transverse mode in the waveguide (rather than one of the higher order modes) by proper orientation of the direction of the incident laser beam. The principle of operation of the prism coupler can best be described using ray optics. The model of the prism coupler used for this analysis is shown in Figure A-16. A more exact analysis will then be used to describe the principle of operation of the optimized design, shown in Figure A-17.

A1.3.2.1 Principle of Operation Using Ray Optics

A typical configuration of a planar dielectric waveguide for use in integrated optical circuits is shown in Figure A-18. It is formed by a thin film on a substrate, where the refractive index of the thin film n_f is higher than that of the substrate n_s or the cover n_c , which, in general, is air. It is

$$n_f > n_s > n_c$$

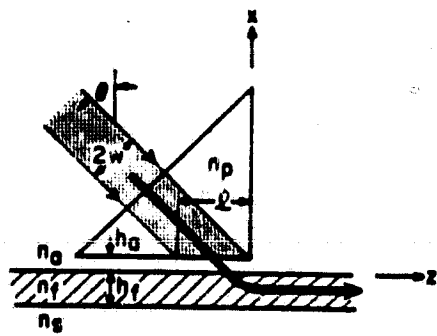


Figure A-16. Prism Input Coupler

T. Tamir "Integrated Optics" Topics in
Applied Physics, P. 87.

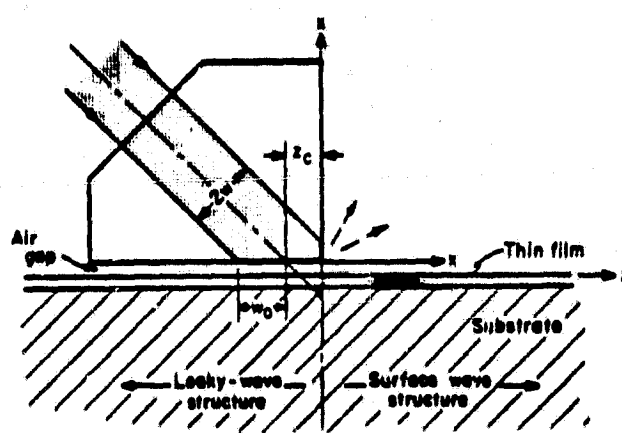


Figure A-17. Alignment Of Incident Beam In Prism Input Coupler For Increasing Coupling Efficiency. Maximum Efficiency Achievable For Gaussian Beams Is 80.1%, Which Is Obtained If $\omega_0 = 0.68$ and $z_c/w_0 = 0.733$

T. Tamir and H. L. Bertoni
 Opt. Soc. America
 Vol. 61, No. 10,
 October 1971, P. 1397

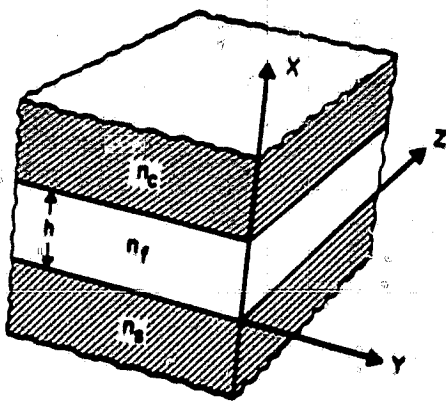


Figure A-18. "Asymmetric" Planar Dielectric Waveguide

For a wave which propagates along the planar waveguide, only the x dimension of the beam cross section is guided while in the y dimension, the wave propagates freely. Using ray optics, a plane wave incident on the boundary of the film under an angle θ which is larger than the angle of total reflection θ_c , (where $\sin \theta_c = \frac{n_s}{n_f}$ (1)), follows a zig-zag path as shown in Figure A-19. The wave is coherent with a free space wavelength λ_0 , the wave travels with a wave vector $\vec{k} n_f$ in the direction of the wave normal and

$$k = \frac{2\pi}{\lambda_0}$$

The field of the wave varies as

$$e^{j(\pm k_x x + k_z z - wt)} = e^{j k n_f (\pm x \cos \theta + z \sin \theta - wt)}$$

For a guided mode in the planar waveguide, the zig-zag picture predicts a propagation constant β_{sw} , which is the z component of the wave vector $\vec{k} n_f$

$$k_z = \beta_{sw} = k n_f \sin \theta \quad (2)$$

Only a limited range of angles θ are allowed which meet the transverse resonance condition

$$2 k n_f w \cos \theta - 2 \theta_s - 2 \theta_c = 2M\pi \quad (3)$$

where w is the thickness of the film with the refractive index n_f , θ_s and θ_c are the phase shift on total reflection from the film-

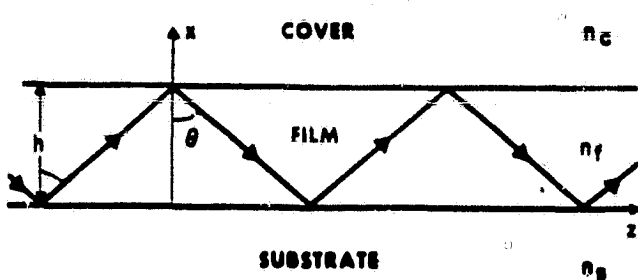


Figure A-19. Side-View Of A Dielectric Waveguide Showing Wave Normals Of The Zig-Zag Waves Corresponding To A Guided Mode.

substrate interface and film-cover interface, respectively, and M is an integer, ($M = 0, 1, 2$) which identifies the mode number. The phase shifts θ_s and θ_c are functions the angle θ and of the refractive indices n_f , n_s and n_c . Equation 3 is the dispersion equation for the waveguide, yielding the propagation constant β_{sw} as a function of wavelength λ_0 and film thickness w . From equations 1 and 2 it follows for guided modes that the propagation constant β_{sw} is bounded by the plane wave propagation constants of substrate and film

$$kn_s < \beta_{sw} < kn_f$$

A typical $\omega - \beta_{sw}$ relation of a dielectric waveguide is shown in Figure A-20 for the modes $M=0$ to 2.

The waves in the dielectric waveguide are not contained entirely within the thin film as shown in Figure A-19 but also penetrate into the adjacent layers in the form of evanescent fields, as shown in Figure A-21. For the fundamental mode ($M=0$) the transverse fields in the three layers of the TE-mode, are

$$E_y = E_c e^{-j\beta c(x-w)} \text{ for } w < x$$

$$E_y = E_f \cos[(kn_f \cos \theta) x - \theta_f] \text{ for } 0 < x < w$$

$$E_y = E_s e^{j\beta s x} \text{ for } x < 0 \quad (4)$$

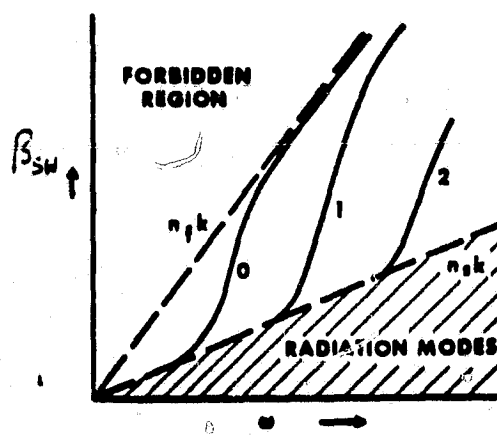


Figure A-20. Typical $\omega-\beta_{sw}$ Diagram of A Dielectric Waveguide
 (T. Tamir "Integrated Optics" Topics in Applied Physics, p. 22.)

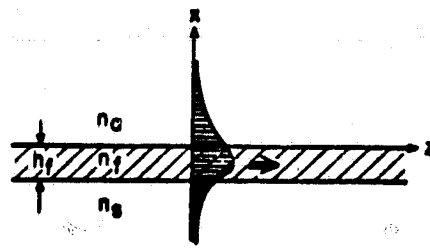


Figure A-21. Field of a Surface Wave Propagating along a thin film, with $n_f > n_a, n_s$

The fields of the guided mode in the dielectric waveguide are those of a homogeneous plane wave; where the wave vectors k_x and k_z are real.

The presence of the coupling prism in Figures 1 and 2 changes the dielectric structure to become multi-layered. When the air gap between prism and dielectric waveguide becomes sufficiently small, coupling occurs between the evanescent fields in waveguide and prism, which results in energy transfer between them. The leakage of energy away from the waveguide results in a decrease of the energy in the waveguide in direction of propagation z . Thus, the wave vector k_z must become complex;

$$k_z = \beta - j\alpha$$

The coupling mechanism between prism and waveguide can best be described using Figure A-22. The laser beam A_3 enters into the prism of refractive index n_3 and propagates downward with an incident angle θ_3 . Within the beam cross section, the A_3 wave is assumed to have constant amplitude and, therefore, the base of the prism is uniformly illuminated from $z = 0$ to $z = 1$. At the base of the prism a part of the incident wave is reflected as the B_3 wave and the remainder is coupled into the film as an A_1 wave. Because of the coupling the amplitude of the waves except that of the A_3 wave will vary in direction of z . Since the coupling occurs through the evanescent fields, the coupling will be very weak, that is,

$$\beta \gg \alpha \text{ and } \beta \approx \beta_{sw}$$

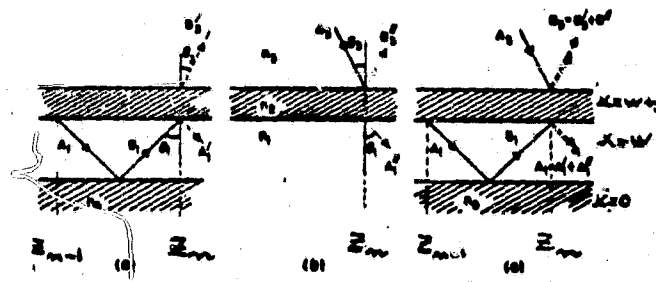


Figure A-22.
 (P.K. Tien and R. Ulrich
 J. Opt. Soc. America, Vol. 60,
 No. 10, Oct. 1970)

(A) Thin Film n_1 Coupled to a Semi-Infinite Medium n_3 through a gap S , (B) Two Semi-Infinite Media n_3 and n_1 , Coupled Through a Gap S , and (C) Waves in a Prism-Film Coupler.

Because the coupling between the waves in the prism and the dielectric waveguide is very weak, efficient energy transfer requires traveling wave interaction. For efficient energy transfer in the traveling wave mode, the wave vector in the direction of propagation in the prism, $kn_3 \sin \theta_3$, must be equal to the wave vector β_{sw} in the thin film guide,

$$kn_3 \sin \theta_3 = \beta_{sw} \quad (5)$$

Further, for complete energy transfer the length of the coupling region in direction of propagation, l , must meet the requirement that

$$Kl = \frac{\pi}{2} \quad (6)$$

where K is the coupling coefficient between the modes.

In the multilayer structure in Figure A-22 representing the prism coupler together with the thin film waveguide, the leakage of energy from the guide to the prism through the gap with the width s , is indicated by the ray B_3^1 in Figure A-22a. The ray A_3 , incident through the prism is totally reflected at the prism-gap interface. Though the angle θ_3 is slightly smaller than the angle θ_1 , total reflection still takes place because $n_3 > n_1$ (n_f). The totally reflected ray is the ray B_3^{11} ; while leakage of energy from the prism to the guide is indicated by the ray A_1^{11} , both shown in Figure A-22b.

The resultant A_1 wave in the guide is the sum of A_1^1 and A_1^{11} . Similarly, the resultant reflected wave B_3 is the sum of B_3^1 and B_3^{11} , both shown in Figure A22c. In the prism-film coupler the ray A_1 is being built up from the ray A_3 and, because of the phase matching

condition in Eq. 5, A_1^1 must always be in phase with A_1^{11} . The two waves add in phase and the amplitude of A_1 must increase over the coupling length l . From the analysis it follows that the rays B_3^1 and B_3^{11} are always 180° out of phase; thus, the resultant B_3 must decrease over the coupling length.

The build up and decrease of the waves (along the direction of propagation) which are coupled from the prism coupler into the dielectric waveguide, are shown in Figure A-23. The amplitude A_3 which represents the cross section of the incoming laser beam projected on the base of the prism coupler, is assumed to be constant over the coupling length from $z = 0$ to $z = l$. $A_1(z)$ is zero for $z = 0$, it increases over the coupling region and reaches its maximum value for $z = l$. For $z > l$ no energy is transferred from the laser beam to the waveguide any longer ($A_1^1 = 0$), but energy is leaking from the waveguide back into the prism ($B_3^1 > 0$) and $A_1(z)$ becomes smaller for $z > l$. The wave which is reflected at the prism base (B_3^{11}) is constant over the beam cross section from $z=0$ to l . The wave B_3^1 which is leaking from the waveguide back into the prism is set up by the wave B_1 which increases from $z=0$ to $z=l$, thus, B_1 and B_3^1 grow together from $z=0$ to l and become smaller for $z > l$. Since B_3^1 is always 180° out of phase in respect to B_3^{11} the sum of the reflected waves B_3 decreases with increasing z from $z=0$ to $z=l$ and finally becomes negative. In summary, the energy transfer from the prism coupler to the waveguide over the coupling region results a) from the constructive interference of the wave in the guide and of the leaky wave from the prism, and b) from the destructive interference of the

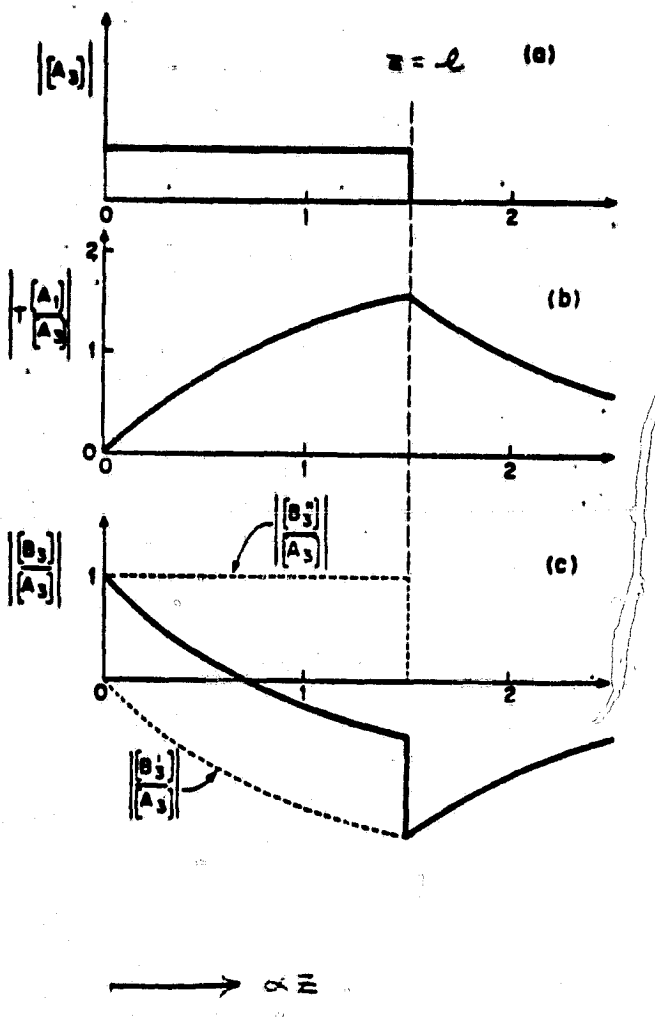


Figure A-23. Distributions of Wave Amplitudes in a Prism-Film Coupler for a) Incident Beam, b) A_1 or B_1 Wave in the Film, and c) Reflected Beam in the Prism

P.K. Tien and R. Ulrich
 J. Optic Soc. America, Vol. 60,
 No. 10, Oct. 1970

reflected incident wave at the prism base and of the leaky wave from the guide into the prism.

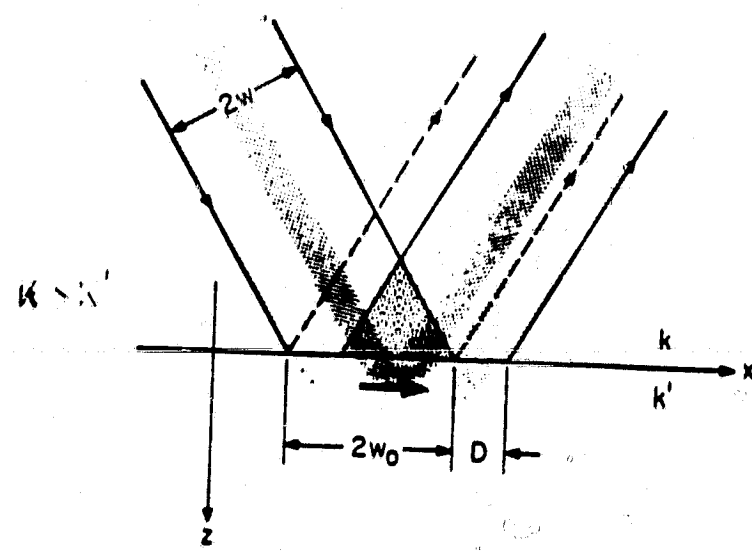
Using the simplified ray optics approach the alignment of the prism coupler requires the adjustment of the angle Θ_3 to meet the total-reflection condition and the phase matching condition in Eq. 5. Then the coupling coefficient must be adjusted to meet Eq. 6 for complete energy transfer from the incident wave in the prism to the guide mode in the dielectric waveguide, over the coupling length l . The coupling coefficient is Eq. 6, is proportional to e^{-2Pcs} where P_c is the decay of the surface wave in the air region in Eq. 4 and s is the gap width. The coupling length in Eq. 6 is given by, $l = 2W \sec \Theta_3$, where $2W$ is the beam width of the incident laser beam.

For an incident laser beam having a uniform amplitude distribution as shown in Figure A-22, it follows from the ray optics analysis that the beam must be incident as shown in Figure A-16, i.e., its right-hand boundary must intercept the prism corner. If the beam is shifted to the right of that corner, a portion of the beam falls outside the coupling region, this portion of beam energy will not be coupled into the waveguide. If, on the other hand, the right-hand boundary of the beam falls to the left of the prism corner, energy from the guided wave in the waveguide can be coupled back by the ray B'_3 into the prism.

A1.3.2.2 Modification of Alignment for Increased Coupling Efficiency

The alignment of the laser beam in respect to the prism corner, however, must be modified for increase in coupling efficiency. The modification is required because of a lateral displacement of a light beam reflected by a dielectric surface (Goos-Hänchen Effect). If a bounded beam is incident on the interface between a denser and a rarer medium under an angle which is larger than the angle θ_c for total reflection, not all the power is reflected at the interface, but a horizontal power flux also occurs within the rarer medium. This flux is mostly confined to a region that lies immediately below the illuminated portion of the interface. The horizontal flux is accounted for by radiant power from the incoming beam that penetrates through the interface. After traveling some distance within the rarer medium, this flux re-emerges into the denser medium and joins the bulk of energy flow to form the complete reflected beam. The lateral flux along z causes the reflected beam to be displaced in the z -direction from the position predicted by geometric optics, as shown in Figure A-24.

Leaky waves in a multi-layered structure (i.e., the prism coupler) experience an energy shifting mechanism along the dielectric boundaries that is analogous to that described for a single dielectric interface. Only the lateral energy shift is larger for leaky waves in a multi-layered structure than for the reflection on a single dielectric interface. In the previous section using ray optics the lateral energy shift had not been considered and the decrease of the



ORIGINAL PAGE IS
OF POOR QUALITY

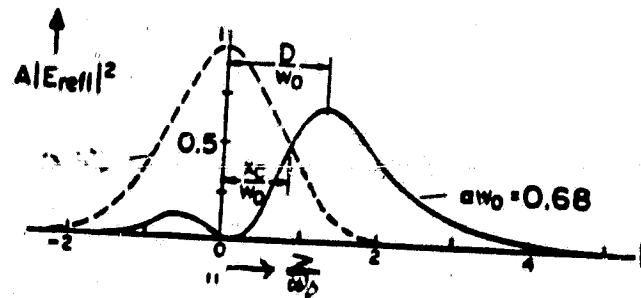
Figure A-24. Lateral Displacement D of a Bounded Beam at a Dielectric Interface. The Dashed Lines Show the Boundaries of the Reflected Beam as Predicted by Simple Geometrical-Optics Considerations; The Thick Arrow Indicates the Direction of Energy Flow in the Lower Medium

I. Tamir and H. L. Bertoni,
J. Opt. Soc. America, Vol. 61,
No. 10, Oct. 1971, p. 1397

reflected wave B_3 from $z=0$ to 1 was based on the destructive interference of the reflected beam B_3^{11} at the prism base and the leaky wave B_3^1 , which were assumed to be synchronous. The difference of the lateral energy displacement of the reflection at a single interface B_3^{11} and of the leaky wave B_3^1 , changes the decrease and later increase of the reflected wave B_3 as a function of z . This is shown in Figure A-25 for an incident beam with Gaussian amplitude distribution, where we observe that the region of destructive interference has become shorter and the reflected wave starts to increase before the amplitude of the incident laser beam has become very small.

To minimize a loss in coupling efficiency in the prism coupler introduced by the lateral energy displacement, the incident beam must be positioned as shown in Figure A-17, where its right-hand boundary overshoots the lower side of the prism. For the highest coupling efficiency, where the product of coupling coefficient times coupling length is $2\alpha w_0 = 1.36$, the offset of the beam with respect to the prism should be $\frac{z_r}{w_0} = 0.733$ where $w_0 = W \sec \theta_3$ and W is the half beam width of the Gaussian beam.

To explain the function of the off-set of the beam in the prism coupler, we must remember that over the coupling length $2w_0 - z_r$ the propagation constant in the waveguide is complex $k_z = \beta_{sw} + j\alpha$ where α represents the loss due to the leaky wave. The geometry is modified at $z > z_r$ to suppress the leaky mode, so that $k_z = \beta_{sw}$, thus supporting a guided mode. An incident beam as shown in Figure A-17, therefore, transfers a major portion of its energy into the thin film waveguide. The energy in the leaky wave region is shifted



$$w_0 = w \sec \theta$$

w Gaussian beam halfwidth

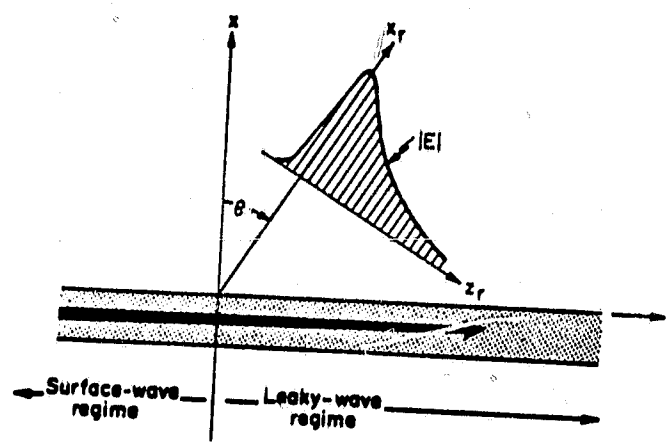
Figure A-25. Intensity of Normalized Reflected Field as a Function of z/w_0 . The Curves Shown are for Total-Reflection and for Phase-Matching ($B=k \sin \theta > 0$)

(T. Tamir and H. L. Bertoni, J. Opt. Soc. America, Vol. 61, No. 10, Oct. 1971, p. 1397)

horizontally along the positive z direction and would be reradiated back into the reflected beam if the leaky wave structure would extend beyond $z=z_c$. Because $\alpha = 0$ at $z > z_r$, the leakage back into the prism is avoided and the coupled energy is propagating in form of a guide mode in the z - direction.

A1.3.2.3 Beam Shape

The prism coupler in Figure A-16 and A-17 is shown as input coupler. By reciprocity, it also can function as output coupler. However, using the same configuration for input or output, their efficiencies are different. This is because the beam radiated by the leaky wave of a multi-layered dielectric structure has exponential amplitude distribution rather than Gaussian, shown in Figure A-26. The output coupler when the height of the coupling gap is adjusted to yield $2\alpha w_0 = 1.36$, can theoretically convert a surface wave into a radiating beam with an efficiency of close to 100 percent. For the input coupler, because of the disparity of the Gaussian shape of the incident laser beam and the exponential shape of the leaky wave, the coupling efficiency can only be 80 percent.



C-3

Figure A26. Amplitude Profile of a Beam Produced by the Leakage Field of a Leaky Wave

(T. Tamir, "Integrated Optics" Topics in Applied Physics, p. 102)

A1.3.3 Grating Coupler

When using a prism coupler, which protrudes from the integrated optics structure, many of the potential advantages of integrated optics would be lost. The grating coupler, is of special interest because its design can be compatible with the realization of these advantages. A typical grating output coupler is shown in Figure A-27. The grating is a phase grating, it is often in form of a photo resist film which has been exposed to a laser interferometer fringe pattern. Depending on the specific photo-resist and the developing procedure, the grating assumes a sinusoidal, triangular, or trapezoidal shape. The presence of the grating changes the propagation properties of the surface wave in the thin-film waveguide. At the interface of the thin film waveguide and the super-imposed grating the guided wave changes to a leaky wave. The leakage of energy is in direction of the discrete diffraction lobes of the grating. The objective of the design of an efficient grating coupler is to avoid all diffraction beams but one backward beam in the substrate, as shown in Figure A-27.

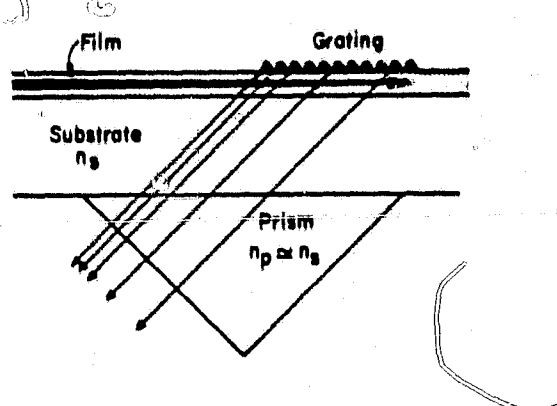


Figure A-27 Grating Coupler With Prism on the Substrate for Converting an Incident Surface Wave into a Single Leaky-Wave Beam. The Usual Parameters are such that Backward Leakage Occurs in Practice.

(T. Tamir "Integrated Optics" Topics in Applied Physics, p. 111)

Assuming a sinusoidal phase grating, where the periodic variation of the dielectric constant in direction of propagation z is;

$$\epsilon(z) = \epsilon_r(1 - M \cos \frac{2\pi}{d} z)$$

where ϵ_r is the average value of $\epsilon(z)$, M is the modulation index and d is the distance between striations, (which are parallel to the y direction). The solution of the wave equations for the field components of the characteristic waves in all of the uniform regions of the structure, (air, film and substrate) under the influence of the grating are,

$$E_j(x, z) = \sum_{-n}^{+\infty} F_n^{(j)} e^{j(k_{xn} x + k_{zn} z)} \quad (7)$$

where the index (j) refers to the j th medium with $(j) = a$ (air), f (fiber) or s (substrate), and $F_n^{(j)}$ are the amplitudes of then space harmonics. The propagation factors of the space harmonics k_{zn} are related to the fundamental longitudinal propagation factor k_{z0} by

$$k_{zn} = k_{z0} + \frac{2\pi n}{d} \quad (8)$$

Each of the space harmonics observes the dispersion relation,

$$k_{xn}^{(j)} = \pm (k_j^2 - k_{zn}^2)^{1/2} \quad (9)$$

where $k_j^2 = k_0^2 \epsilon_j$.

If the grating is sufficiently thin, the fundamental propagation factor k_{z0} is very closely given by the propagation factor of the guided wave β_{sw} on the uniform layered structure (with no grating). The propagation factor of the guided wave β_{sw} on the uniform layered structure (with no grating). The propagation factor of the guided wave β_{sw} was defined in Equation 3. It is bounded by the plane wave propagation factors k_{n_s} of the substrate and k_{n_f} of the film, as shown in Figure A-20. The fields of the dominant fundamental partial wave ($n=0$), can be approximated by the fields of the guided wave in Equation 4.

The characteristics of the grating coupler can best be derived from Equations 3, 4, 8 and 9. For the fundamental partial wave ($n=0$) which travels in direction of propagation z of the guided wave, the fields in air and substrate are evanescent with respect to x , because $k_{x0}^{(a)}$ and $k_{x0}^{(s)}$ are imaginary, as can be shown from Equation 9.

Because $\beta_{sw} > k_{n_s} > k$,

$$(k_{x0}^{(a)})^2 = (k^2 - \beta_{sw}^2) < 0$$

$$(k_{x0}^{(s)})^2 = (k^2 n_s^2 - \beta_{sw}^2) < 0$$

All higher order partial waves ($n \neq 0$) posses small amplitudes. As the surface wave enters and progresses along the grating, a very small amount of the field scattering occurs. Because this scattering is

very weak, the surface wave field in the grating region $z>0$ (on a local scale) is essentially quite similar to that in the region without grating $z<0$. However, if the grating is long, the energy leakage by scattering adds up to a large portion of the energy brought into the grating region by the incident surface wave. Because of the regular placement of the scatterers, the individually scattered fields interfere constructively only along certain preferred direction at angles which are given by

$$k \sin \theta_{an} = \beta_{sw} + \frac{2\pi n}{d} \quad n = \pm 1, \pm 2 \quad (10)$$

for radiation into air; and at angles

$$k n_s \sin \theta_{sn} = \beta_{sw} + \frac{2\pi n}{d} \quad (11)$$

for radiation into the substrate.

Leakage of energy of the n -th space harmonic into air can only occur when $k_{xn}^{(a)}$ in Equation 9 is real; leakage of energy into the substrate only when $k_{xn}^{(s)}$ is real. The leakage of energy causes a decay of the guided wave with z as it progresses along the grating region. Hence, the propagation factor k_{zn} along the grating region cannot remain purely real but, instead k_{zn} changes to a complex value.

$$k_{zn} = \beta_{sw} + \frac{2\pi n}{d} + j\alpha \quad (12)$$

For an efficient grating output coupler it is required that the surface wave incident on the grating of the coupler be transformed into a leaky wave having a single propagating space harmonic in the substrate and no propagating one in the air region. This can be accomplished by choosing the appropriate ration of $\frac{d}{\lambda}$,

to yield the following relations

$$\begin{aligned} (a) \quad (k_{xn})^2 &= (k^2 - (\beta_{sw} + \frac{2\pi n}{d})^2) < 0 \text{ for } n = -1 \\ (s) \quad (k_{xn})^2 &= (k^2 n_s^2 - (\beta_{sw} + \frac{2\pi n}{d})^2) > 0 \text{ for } n = -1 \\ (s) \quad (k_{xn})^2 &= (k^2 n_s^2 - (\beta_{sw} + \frac{2\pi n}{d})^2) < 0 \text{ for } n = -2 \end{aligned} \quad (13)$$

The Brillouin diagram for a spatially modulated layered structure is shown in Figure A-28. (Figure A-20 shows a similar relationship for the dielectric waveguide). The propagation factor β_0 of the modulated structure is very closely equal to the value β_{sw} for the surface wave along a uniform ($M=0$) layer. The propagation factor β_0 is bounded by the plane wave propagation constants of substrate (kn_s) and film (kn_f). These limits are the straight lines OB and OC in Figure A-28. For small values of $\frac{d}{\lambda}$ ($\frac{d}{\lambda} \leq 0.3$), that is inside the triangle OLG, the propagation along the grating regions is that of a guided surface wave, where all $k_{xn}^{(j)}$ for $j=a$ and s are imaginary. For $\beta_0 d = N \pi$ the grating manifests itself by causing a stopband. Outside the triangle OLG for $0.32 < \frac{d}{\lambda} < 0.38$ Equation 13 is met, where $k_{x,-1}^s$ is real. Outside the larger triangle ODG for $\frac{d}{\lambda} > 0.38$ $k_{x,-1}^s$ and $k_{x,-1}^a$ are both real.

Thus, for values of $\frac{d}{\lambda}$ for which the operation point is inside the smaller triangle OLG (e.g. point P), the surface wave remains bound even if the grating is present. As the ratio $\frac{d}{\lambda}$ increases and the operation point crosses the line FG (e.g. point Q), a single radiation beam appears in the substrate (Equation 13) and the surface wave is changed to a leaky wave. For larger values of $\frac{d}{\lambda}$ where the

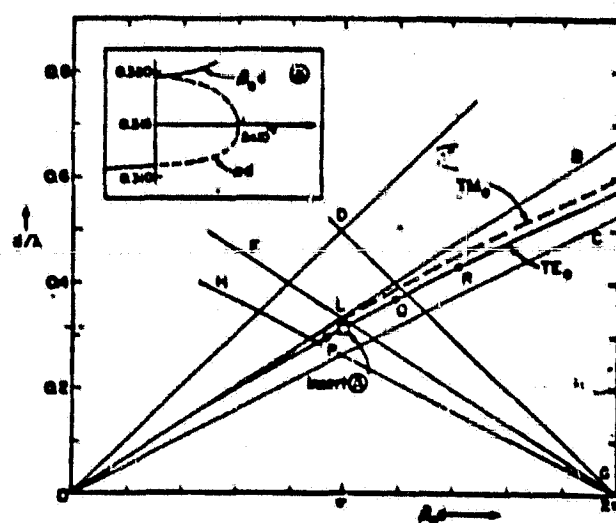


Figura A-28. Variation of $\beta_0 d$ for the Fundamental TE and TM Modes Along a Modulated Layer With $\epsilon_a = 1$, $\epsilon_s = 3.61$, $\epsilon_r = 2.25$, $M < 0.5$. The insert shows the first stopband for $M = 0.08$

(S. T. Peng, T. Tamir and H. L. Bertoni, IEEE Transactions
MTT vol. MTT-23, No. 1, Jan. 1975, p. 123)

operating point is above the DG line (i.e. point R) radiation beams appear in substrate and air regions.

In Figure A-29 the attenuation factor in Equation 12 is shown. In the surface wave region that is for values of $\frac{d}{\lambda}$ inside the triangle OLG (in Figure A-28), is practically zero. In the stopband around L, α peaks strongly. Outside the stopband above the line FG the attenuation factor α is due to energy leakage into the radiation beam in the substrate. Above the line DG, α is due to two radiation beams. As seen in Figure A-29 α varies slowly in the leaky wave region, except in the vicinity of points which correspond to the on-set of additional leaky wave beams in the air or substrate region.

From Figures A-28 and A-29 follows the design of an efficient grating coupler where the surface wave, incident on the grating, is transformed into a leaky wave having a single propagating space harmonic in the substrate. For instance, for $n_f = 1.9$ and $n_s = 1.5$, the ratio $\frac{d}{\lambda}$ which meets the requirements of Equation 13, must be between 0.32 and 0.38

The beam direction of the space harmonic ($n = -1$) from Equation 11 is given by

$$kn_s \sin \theta_{s,-1} = \beta_{sw} - \frac{2\pi}{d}.$$

For $n_s = 1.5$, and $\beta_{sw} \approx 1.7k$ and $\frac{d}{\lambda} = 0.35$, $\theta_{s,-1} = -50^\circ$.

The beam direction of the space harmonic ($n=1$) in the substrate is backward. However, the leakage angle $\theta_{s,-1}$ is larger than the critical angle for total reflection between substrate and air. To be able to couple from the substrate into air, therefore, it is necessary to

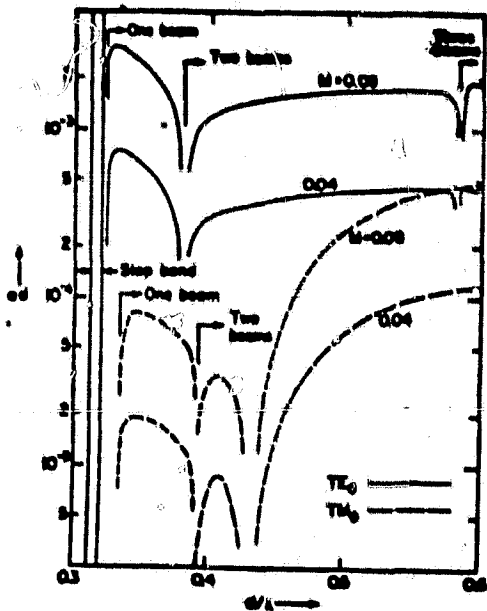


Figure A-29. Variation of the Attenuation Parameter α with Frequency for the same Grating as that in Figure 28. The Range Shown Allows for Either a Single Beam in the Substrate (e.g., Point Q in Figure 28) or for Two Beams, One Each in the Substrate and Air Regions (e.g., Point R in Figure 28). Inside the Stopband α Becomes Very Large and Reaches a Peak Which is Well Outside the Vertical Range Shown.

(S. T. Peng, et al., IEEE Transaction MTT,
Vol. MTT-23, No. 1, January 1975.)

deform the lower boundary of the substrate or to add a prism as shown in Figure A-27.

A comparison between the prism coupler and the grating coupler shows that in both couplers the surface wave is converted into a single output beam. Thus, the efficiency of the grating output coupler can also approach 100 percent. Also the beam shapes of the two output couplers are quite similar, as shown in Figures A-30 and A-26. When coupling a Gaussian beam by a grating input coupler, because of the disparity in beam shapes, a maximum efficiency of only 80 percent can be attained.

Similarly, the requirements of off-setting the beam in relation to the grating for maximum efficiency (shown in Figure A-31), also holds for the grating coupler.

A1.3.4 Thin-Fiber Tapered Waveguide Coupler

The principle of the tapered coupler is shown in Figure A-32. It consists of a section of dielectric waveguide, where the thin film region is tapered down. Using the geometric optics approach, the waves undergo zig-zag bounces whose angles of incidence on the film substrate interface decrease progressively as the taper narrows down. As a result, at point P, the angle of incidence becomes smaller than the critical angle of total reflection and therefore, the rays are refracted into the substrate. The energy transfer is augmented by that of subsequent rays, so that ultimately most of the energy in the guided wave is transformed into an outgoing beam. Because the beam formed by a tapered coupler is produced by rays that emerge at

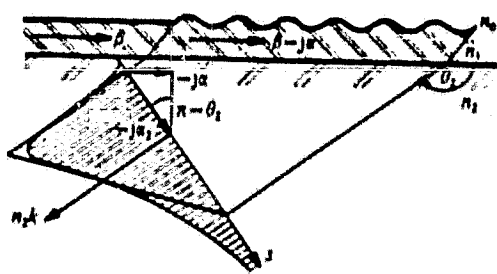


Figure A-30. Reverse Substrate Beam Excited By a Film Mode In a Sinusoidal Grating Coupler.

(H. G. Unger "Planar Optical Waveguides and Fibers" Clarendon Press, P. 142.)

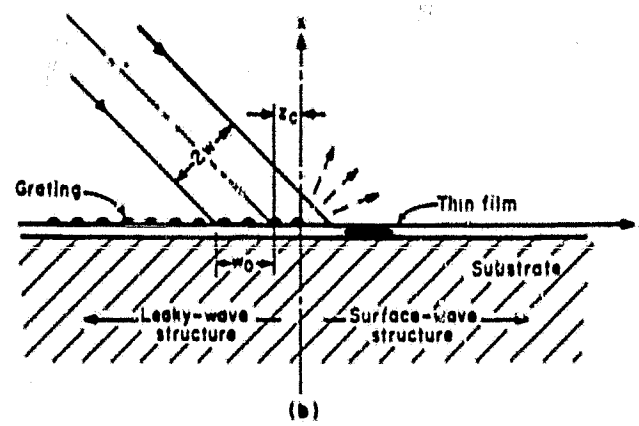


Figure A-31. Alignment of Incident Beam in Grating Input Couplers for Increasing Coupling Efficiency. Maximum Efficiency Achievable for Gaussian Beams is 80.1%, Which is Obtained if $\omega_0 = 0.68$ and $z_c/w_0 = 0.733$

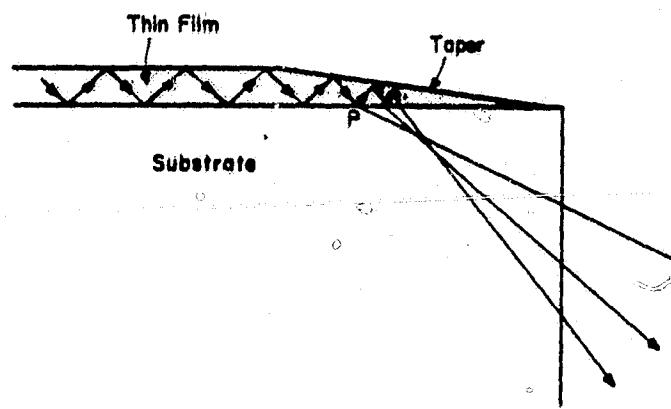


Figure A-32. The Tapered Thin-Film Waveguide Coupler

(T. Tamir "Integrated Optics" Topics in Applied Physics, p. 118).

slightly different angles, the outgoing beam is characterized by a relatively large divergence. Also, the surface wave is converted rapidly into the outgoing radiation once the surface wave reaches the cut-off width of the asymmetric dielectric waveguide. From these properties the assumptions can be made that the phase front of the outgoing radiation has close to circular shape

When the tapered thin-film coupler is used as an input coupler it seems possible to match the circular phase front of the radiation from the narrow side of the p-n junction of an injection laser, to the required phase front of the coupler. If this can be accomplished the coupling efficiency could be quite high between the radiation of an injection laser and a surface wave, using the tapered coupler. When evaluating the coupling efficiency consideration must be given that coupling in the tapered coupler is based on the excitation of the Eigenmode of the dielectric wave guide rather than in traveling wave interaction.

A1.3.5 Summary

Prism, grating and thin-fiber waveguide coupler schemes were analyzed for coupling light energy from a single mode injection laser into a single mode integrated optic switch. It was found that the prism coupler has disadvantages because of its bulk size, and further it requires special attention in optical alignment of the entrance beam to maintain high coupling efficiency.

The maximum coupling efficiency is less than 80 percent owing to the different beam shape of the incident light source and the allowed propagation mode.

The grating coupler, has the desired form factor for use with the integrated optic switch. This coupler uses a phase grating and its efficiency can approach 100 percent, but again the beam shape factor will limit efficiency to about 80 percent.

The tapered thin-fiber coupler appears to circumvent the beam shape coupling loss problem, but is still developmental.

However, the prism coupler, the grating coupler and the tapered thin-fiber coupler take up space on the switching matrix. Because of the limited size of the single crystal LiNbO_3 or LiTaO_3 it seems advisable to use endfire couplers rather than one of three couplers described in Section A1.3.

A1.4 AlGaAs LASER INTEGRATED WITH OPTICAL WAVEGUIDES

A1.4.1 Introduction

Two methods for integration of AlGaAs lasers with optical waveguides have been reported. One method attempts to couple the laser through a transition region to the optical waveguide. In the second method the laser is built directly on the substrate using distributed Bragg reflectors (DBR) instead of the cleaved mirrorfaces to form the Fabry-Perol cavity of the laser. The laser structure is that of an "large optical cavity" (LOC) laser.

A1.4.2 Transitions Between AlGaAs Lasers and Optical Waveguide

Several design concepts have been reported for coupling the oscillation from an AlGaAs laser to a single mode channel waveguide. The interconnecting path in all these designs is formed by a guide layer that has a slightly higher energy gap than the active layer, and thus has a small absorption loss coefficient of less than a few cm^{-1} . The transition to this layer in one design is formed by a tapered section of the active region. In another design the transition is made over the entire length of the lasing junction. The active layer is very thin and the optical field of the guided mode spreads both the active layer and the adjacent guide layer with a slightly higher energy gap.

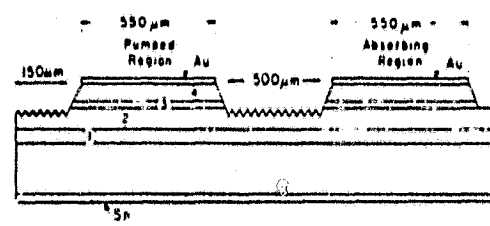
A1.4.3 LOC-DBR Injection Lasers with Integrated Passive Waveguide

The most promising laser configuration for integrated optical systems which includes the optical source, devices, and components in miniature waveguide form, is the thin-film DBR Fabry-Perot laser. It consists of an active medium between two periodic gratings etched on top of the thin film waveguide. The requirements for this type of device are high quantum efficiency and low threshold current. Oscillation in the fundamental transverse mode is also essential, for operation with low-loss, single-mode fibers. The "large-optical-

cavity $\text{Al}_x\text{Ga}_{1-x}\text{As}$ injection laser with low-loss Bragg reflectors" seems to meet all these requirements. The configuration of this type of laser is shown schematically in Figure A-33. The LOC structure accomplishes the coupling from the active region to the low loss waveguide. The DBR provides the feedback for the stimulated emission. The LOC structure is formed by the very narrow (about 0.1 micron) p-type GaAs layer and the larger (about 1 micron) n-type guiding $\text{Al}_x\text{Ga}_{1-x}\text{As}$ layer. The energy gap of the $\text{Al}_x\text{Ga}_{1-x}\text{As}$ layer is slightly higher than that of GaAs, for $x=0.1$. Thus, it has a low absorption coefficient for the GaAs emission also its refractive index is slightly smaller than that of GaAs. Because of the very thin active layer in which the inversion occurs, and the small difference in refractive indices, the optical field of the guided mode spreads over both the active layer and the AlGaAs guide layer, and a large part of the guided mode energy is in the low loss $\text{Al}_x\text{Ga}_{1-x}\text{As}$ layer.

The distributed Bragg reflectors, formed by periodic gratings, are made part of the $\text{Al}_x\text{Ga}_{1-x}\text{As}$ layer outside the active layer. The function of the distributed Bragg reflector is based on the parametric interaction of two colinear optical waves by a periodic structure.* These waves are a forward wave and a "forced" backward wave. Without the peridic grating only the forward wave can exist. The periodic grating couples the forward wave to a colinear backware wave, and the coupling is strongest when the periodic spacing Λ is one-half optical guide wavelength or a low multiples of it.

*The parametric interaction of the two colinear waves in the distributed Bragg deflector requires that $\Lambda = \frac{\lambda_0}{2n}$. It differs from the Bragg diffraction of the electro-optic Bragg diffraction switch, where $\Lambda > \frac{\lambda_0}{n}$.



Layer	Thickness (μm)	Composition	Doping
①	3.0	(Ga _{0.7} Al _{0.3})As	$n=2 \times 10^{17}$ (Sn)
②	1.0	(Ga _{0.7} Al _{0.3})As	$n=2 \times 10^{17}$ (Sn) (Guide layer)
③	~0.1	GaAs	$p=1 \times 10^{18}$ (Ge) (Active layer)
④	7.3	(Ga _{0.7} Al _{0.3})As	$p=1 \times 10^{19}$ (Ge)

Figure A-33. Schematic Diagram of the Large Optical, Cavity DBR Laser.

$$\Lambda = m \frac{\lambda_0}{2n_{\text{eff}}}$$

where, m is an integer. For typical value of $\lambda_0 = 8700\text{\AA}$ and $n_{\text{eff}} = 3.53$,

$$\Lambda = m 1233\text{\AA}$$

The distributed Bragg reflectors should be formed by third-order corrugations ($m=3$), where most of the energy is guided by the periodic gratings and the radiation loss is minimized.

The parametric interaction introduced by the periodic grating results in a monotonic decrease of the amplitude of the incident wave $A(0)$ as it progresses through the grating in the x direction. The decrease in amplitude is given by

$$A(x) \approx A(0) \frac{\cosh K(x-L)}{\cosh KL}$$

At the end of the grating where $x=L$ the amplitude $A(L)$ remains constant, corresponding to transmitted wave, as shown in Figure A-34. The amplitude of the forced backward wave $B(x)$ shows a monotonic increase from $B(L)=0$ at the end of the grating to a value $B(0)$ at the frontend of the grating. For $x<0$, $B(0)$ remains constant. The forced backward wave, which is given by

$$B(x) \approx -jA(0) \frac{\sinh K(x-L)}{\cosh KL}$$

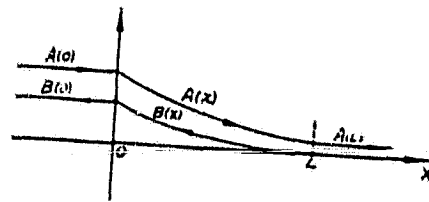


Figure A-34. Amplitude distributions of $A(x)$ and $B(x)$.

(C.F. Quate, et al. Proc. IEEE, Vol. 53, No. 10, Oct. 1965).

contributes to the feedback for sustaining the stimulated emission in the active layer of the laser.

The coupling coefficient K is determined by the geometry of the corrugations. For the simplest case of a sinusoidal modulation of the refractive index of the form

$$n(w) = n_0(w) + 1/2 [n_1 e^{jGx} + n_{-1} e^{-jGx}]$$

where,

$$G = \frac{2\pi}{\Lambda},$$

the coupling coefficient is

$$K = \frac{n_1}{n_0} \frac{\bar{k}}{2}$$

and $\bar{k} = n_0(w) \frac{\omega}{c}$.

The coupling coefficient K characterizes the strength of coupling between the colinear waves propagating in opposite directions. For the case of sinusoidal refractive index modulation K is directly proportional to the fractional index of modulation and the wave number.

A typical value for the coupling coefficient of the laser structure shown in Fig. A-33 is $K \approx 50 \text{ cm}^{-1}$. An experimental laser operating on 3rd with $\lambda = 3726\text{\AA}$ using a triangular shaped corrugation of depth 1500\AA has been demonstrated. The active region of the laser was 550 microns long. The two DBR regions were 150 microns (on the output reflector side) and 500 microns (on the mirror reflection side).

APPENDIX B

To complete the feasibility study of the high data rate optics switching center, using an integrated optics switching matrix, it seems important to compare different types of switching systems. Specifically, the integrated optics switching system was compared to an opto-electronic switching system and to an electronic switching system.

B1.1 OPTOELECTRONIC SWITCHING NETWORK (Hybrid Switching Network)

Switching networks will be analyzed which combine optical distribution from the input to the output terminals with electronic switching to form the appropriate connections. In the opto-electronic network light sources such as Light Emitting Diodes or AlGaAs lasers are modulated with the information from the n input channels. The light sources which are coupled to multimode optical fibers distribute, by means of lenses or optical fibers, the input channels to the photodiodes. The photodiodes convert the modulated optical waves to electric signals which then are directed to the m output terminals. The opto-electronic switching network requires at least $n \times m$ electronic switches; in addition, they either require n light sources and $n \times m$ photodetectors; or $n \times m$ light sources and m photodetectors.

B1.1.1 Opto-Electronic Network With N Light Sources and N X M Photodetectors

The design principle is shown in Figure B2-1. Each light source is modulated by one information channel. The light source modulated

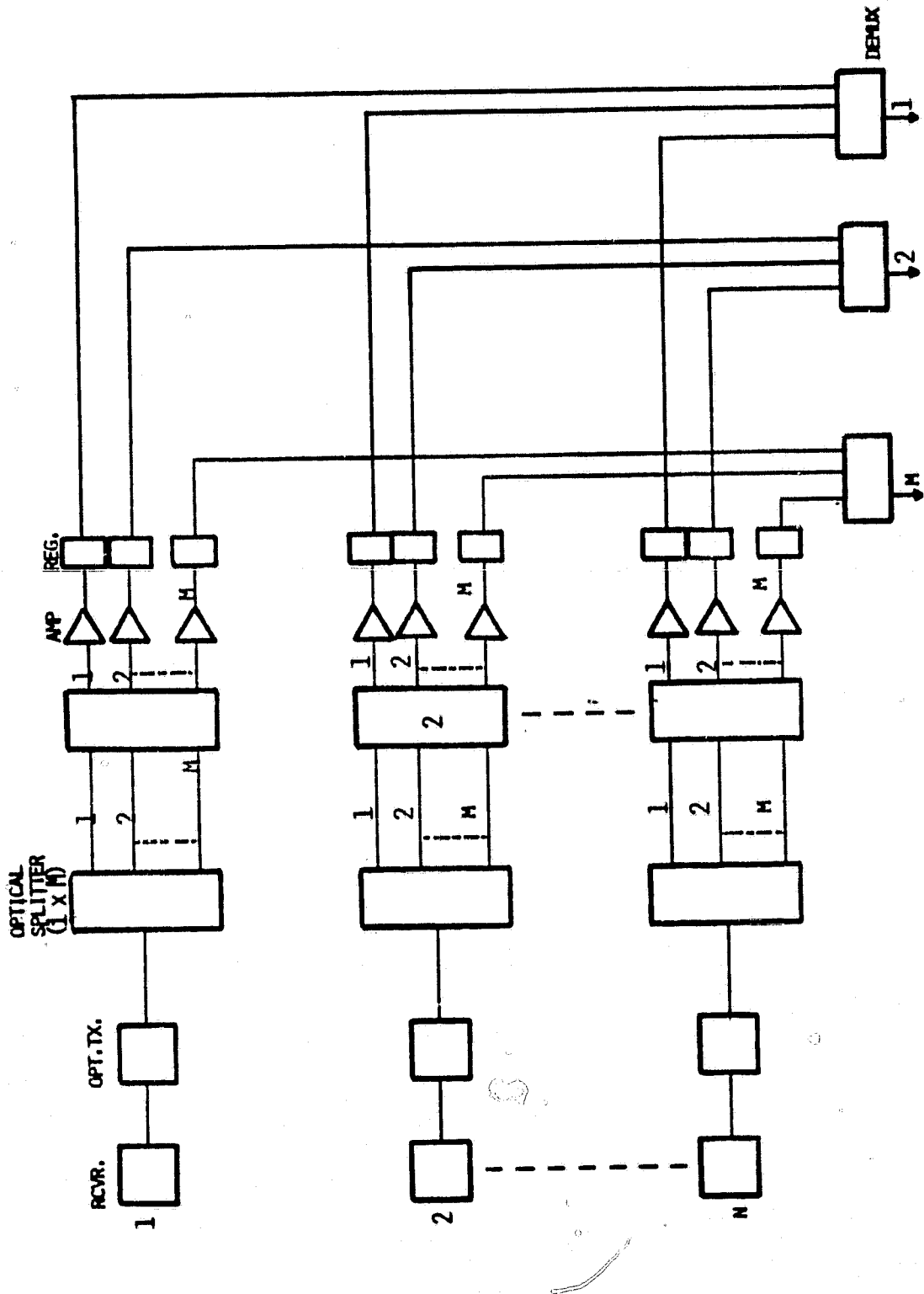


Figure B2-1. Hybrid Switching System

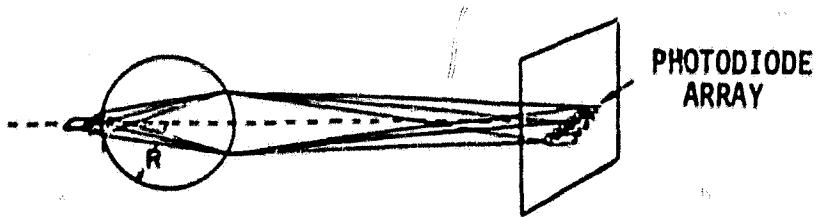
with information channel 1, illuminates m photodiodes, the m photodiodes are connected to the m output terminals. The second light source modulated with information channel 2, illuminates m different photodiodes. They are connected in parallel to the m output terminals. This is repeated for all n input channels.

④ B1.1.1.1 Optical Distribution

The requirements for the optical distribution from one optical fiber to the m cooperating photodetectors are: efficient energy transfer, equal energy division among the photodetectors and confinement of the light to the guiding structure. To distribute the light to the photodiodes advantage can be taken of the wide angle radiation of the multimode fibers, where $NA \approx 0.21$. For efficient power transfer from the optical fiber to the photodetectors the radiation need only be collimated in one meridian plane by a cylindrical lens. In the orthogonal plane the linear photodiode array should fill the light beam, as shown in Figure B2-2a. The distribution of the light to the photodetectors can also be performed by optical fibers, as shown in Figure B2-2b.

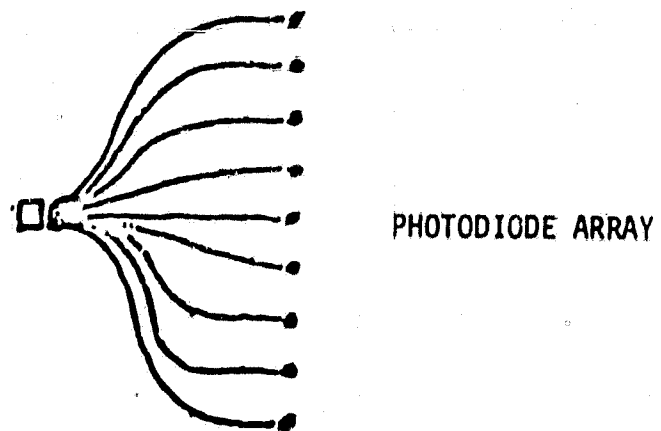
A novel design for the optical distribution from the input lines to the photodetectors is shown in Figure B2-3. In Figure B2-3 the input optical fiber is coupled to an optical multi-mode

OPTICAL FIBER



A) DISTRIBUTION USING CYLINDRICAL LENS

OPTICAL FIBER



B) DISTRIBUTION USING OPTICAL FIBERS

Figure B2-2. Distribution of Light to Photodiode Array

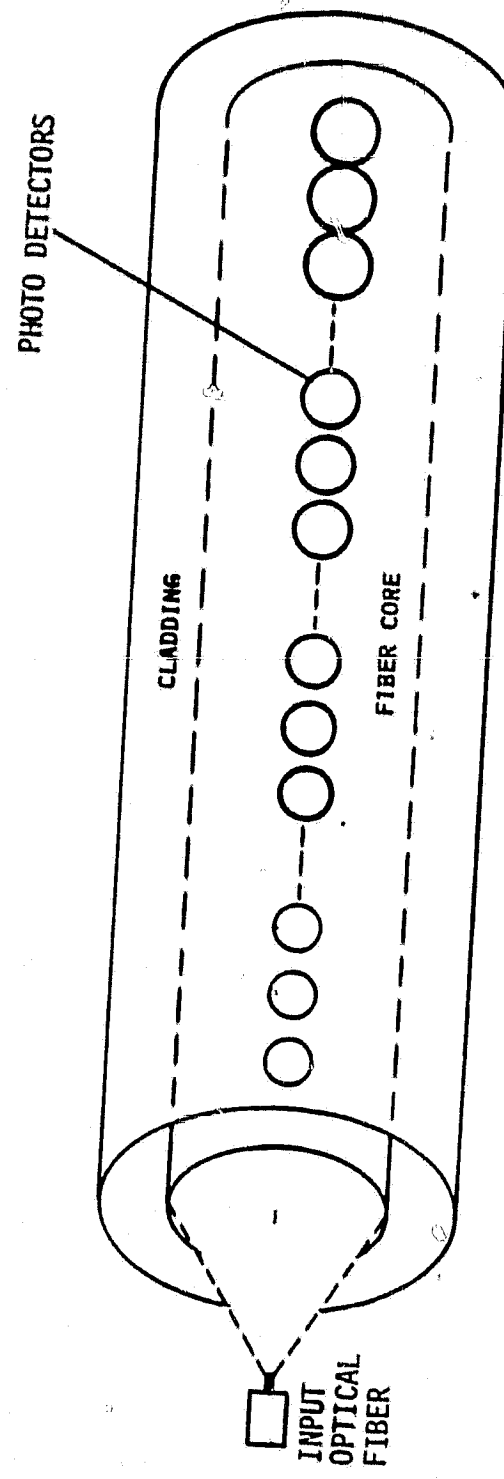


Figure B2-3. Optical Distribution Using Optical Fiber Photo Detector Array

fiber with large core diameter. A linear array of miniature photodetectors is placed along the axis of the fiber on the surface of the fiber core. To do so part of the fiber cladding has to be removed and the refractive index of the photosensitive surface of the photodetector must be index-matched to the refractive index of the fiber core.

The photodetectors in the array should be silicon diodes with a refractive index of $n = 3.42$. Because their refractive index is higher than that of the fiber core of $n \approx 1.6$, the waves inside the fiber core will not be totally reflected at the core surface. Instead they will be transferred to the photosensitive surface of the photodiode. To minimize reflections at the interface between fiber core and photodiode an index-matching layer with a refractive index of $n \approx 2.4$ should be placed between the two surfaces. To assure close coupling the index matching layer should be of pliable material.

To evaluate the power transfer from the fiber core to the photo-detectors, the propagation of optical energy within the fiber core has to be studied. The physical picture of guided light propagation inside the fiber core is that of superimposed uniform plane waves with wave-normals which follow the zig-zag path indicated in Figure B2-4 and which are totally reflected at the core boundaries. The plane waves travel with a wavevector $k n_f$ (where n_f is the refractive index of the fiber core) in the direction of the wavenormal. The fields of these waves vary as

$$\exp (-jkn_f(\pm x \cos \theta + z \sin \theta)) \quad (1)$$

In the multimode fiber the angle range Θ of the superimposed plane waves is limited by the requirement for total reflection at the core-cladding or core-air interface. The plane waves can take up the angles from $\theta \geq \arcsin \frac{n_s}{n_f}$ to $\theta \leq \arcsin 1$.

For the guided modes in the multimode fiber the zig-zag picture predicts a propagation constant β

$$\beta = kn_f \sin \theta \quad (2)$$

For the multimode fiber the assumption can be made that the energy is uniformly distributed over the core cross section, so that the power flux density is $S = \frac{P}{2\pi r^2}$, where P is the incident optical power and r is the core radius. Using the zig-zag picture then S is also the power flux density of the waves with the wave vector kn_f in Figure B2-4.

The optical power which is transferred from the fiber core to the photo detector (using an index matching layer) is proportional to the power flux density S incident under the angles Θ , multiplied with the absorption cross section of the photodetector, A , when projected on the wavenormal of the incident waves. Assuming a square detector aperture ($A = a^2$), then the intercepted power is

$$- P_{in} = S a^2 \sin \theta \quad (3)$$

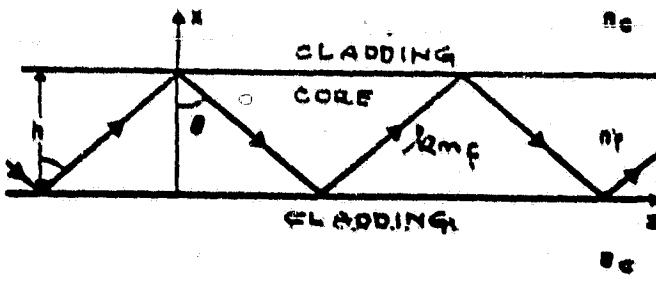


Figure B2-4. Side View of a Optical Fiber Showing Wave Normals of the Zig-Zag Waves Corresponding to a Guided Mode

Obviously, the largest contribution will come from the waves where

$$\Theta \approx \arcsin \frac{r_s}{n_f} \quad (4)$$

For typical value of $P = 10 \text{ mW}$, $r = 300 \text{ microns}$, $a = 150 \text{ microns}$
 $\sin \Theta = 0.16$, $P_{in} \approx 100 \mu \text{W}$.

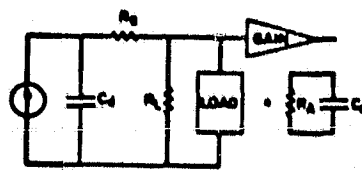
The light energy in the optical fiber becomes smaller as the waves travel along the fiber axis, this is partly because of the energy transfer to the photodetectors and partly because of attenuation in the optical fiber. To compensate for the decreasing light energy, the active areas of the photodetectors which are further removed from the light source, must be larger than those closer to the light source.

There are no optical limitations to the spacings of the photodiodes in the array. The spacings should be such that the post-detection amplifiers can be connected to the photodetectors.

1.1.1.2 Electronic Connections to the Output Lines

In the opto-electronic switching system the distribution of one input channel to the m output terminals is greatly facilitated by the use of a light source and a photodiode array. However, care must be taken that the parallel operation of the post-detection circuits does not seriously affect their transfer properties.

A typical photodetector circuit is shown in Figure B2-5. The photodiode is represented by a current generator in parallel with the photodiode's junction capacitance C_d (of a few pF) and a small series resistance R_s (a few ohms). The load circuit consists of the load resistor



C_d = DIODE JUNCTION CAPACITANCE
 R_d = DIODE SERIES RESISTANCE
 R_L = PHYSICAL LOAD RESISTOR
 R_A = AMPLIFIER INPUT RESISTANCE
 C_A = AMPLIFIER SHUNT CAPACITANCE
 $C_1 = C_2 = C_3$
 $R = V_d \left(\frac{1}{R_d} + \frac{1}{R_L} \right)$

Figure B2-5. Typical Photodetector Circuit

R_L (approximately 50 ohms) and an ac coupled amplifier in parallel. The equivalent amplifier circuit is formed by the resistor R_a in parallel with the capacitance C_a followed by an ideal, infinite impedance amplifier with the gain $A(f)$ (where f is the base band frequency). The output voltage is given by

$$V_{out}(f) = I(f) A(f) Z(f) \quad (5)$$

where $I(f)$ is the detector current and $Z(f)$ is the impedance at the frequency f .

$$Z(f) = \left(\frac{1}{R} + j\omega C \right)^{-1} \quad (6)$$

and

$$R = \left(\frac{1}{R_L} + \frac{1}{R_a} \right)^{-1}$$

$$C = C_a + C_d$$

When the photodetectors would be operated in parallel, the capacitance in Equation A2-6 would increase and the impedance $Z(f)$ would become smaller at higher frequencies.

A better, though more expensive design, would operate each photodiode with a separate post-detection amplifier in order to provide isolation among the parallel circuits (shown in Figure B2-6).

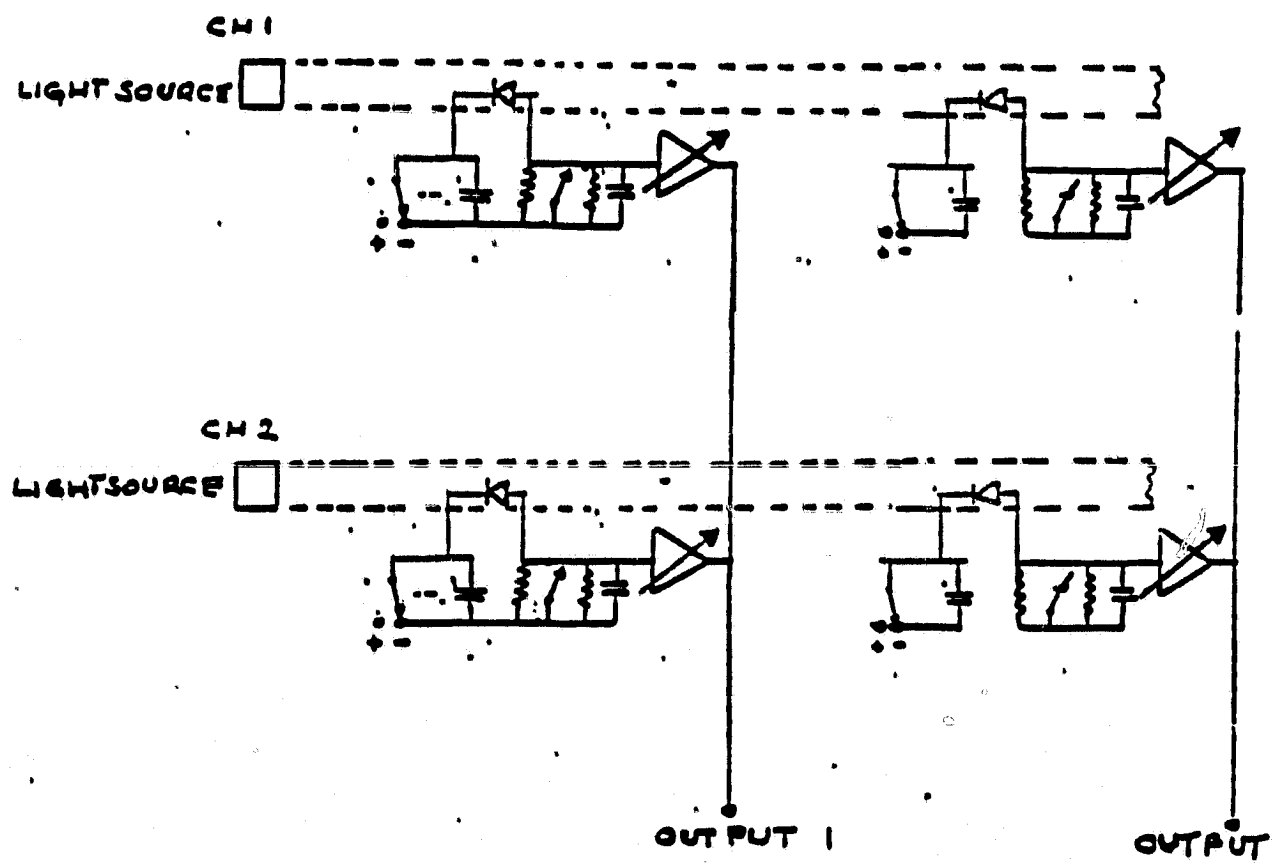


Figure B2-6. Schematic of Opto-Electric Switching Network for N Light Sources and $N \times M$ Photodetectors

In this design the switching function can be incorporated into the post-detection amplifier circuits of the photodetectors. Advantage can be taken that the amplifiers can be "gated" by changing the bias voltage so that the amplifier gain becomes greatly reduced and the internal impedance of the amplifier becomes very high. In the switching system only the post-detection amplifier in the one channel which must be connected to the corresponding output line is operated with optimum gain when terminated by the characteristic impedance of the output line. The n-1 post-detection amplifiers in the same column are "gated", so that their gain becomes very low, and their high impedance will not noticeably load down the output transmission line. The use of gated amplifiers should not only minimize the cross coupling between the inactivated and the activated input channels, but also reduce the noise contribution from the inactivated photodetection circuits.

If greater isolation between the inactivated and the activated input channels, is required, the load resistance in each of the inactivated photodetection circuits can be shorted, as shown in Figure B2-6. In addition, the photodiodes can be forward biased or avalanche photodiodes can be used where the negative bias voltage is reduced from its optimum value of approximately -300 volts to a few volts.

This switching concept has the advantage that the switches primarily change the operating conditions of amplifying devices by varying the negative bias voltages, where the current is extremely small. Also, no switches are in the main lines.

For the proper design of the opto electronic switching network an evaluation of the signal-to-noise ratio is of importance. The variables in the network are: the use of photodiodes versus avalanche photodiodes, and the choice of the load resistance R_L in Figure B2-6. The signal-to-noise ratio is

$$\text{SNR} = \frac{I^2}{(\delta I)^2 + \frac{I^2}{I_{th}}}$$

where $I = \frac{ne}{hv} P$, η is the quantum efficiency of the photodiode. $\frac{e}{hv} = 0.73 \frac{A}{W}$ and P is the optical power. The term $\overline{\delta_i}^2$ represents the shot noise that is the mean square fluctuation in the rate of arrival of the electrons, $\overline{\delta_i}^2 = 2 \frac{ne^2}{hv} PB$, where $e = 1.6 \times 10^{-19}$ A sec and B is the band-width of the baseband information. The term $\overline{\delta_i}^2$ represents the thermal noise (Johnson noise) primarily introduced by the photodiode's biasing resistance R_L , $\overline{\delta_i}^2 = 4kT \frac{B}{R_L}$, where $kT = 4.15 \times 10^{-21}$ W sec. Then

$$\frac{S}{N} = \frac{(\frac{ne}{hv} P)^2}{2 \frac{ne^2}{hv} PB + 4kT \frac{B}{R_L}}$$

For photodiodes with avalanche gain G the output current becomes $\frac{ne}{hv} GP$. The shot noise also increases due to the randomness of the multiplication mechanism. The shot noise term for an avalanche detector is $\overline{\delta_i}^2 = 2 \frac{ne^2}{hv} G^2 F(G)PB$, where $F(G)$ is a measure of the degradation due to the randomness of the multiplication. For the ratio of ionization probability $k = 0.025$, $F(G) \approx 4.5$.

For an avalanche photodiode the signal-to-noise ratio is

$$\frac{S}{N} = \frac{(\frac{ne}{hv} GP)^2}{2 \frac{ne^2}{hv} G^2 F(G)PB + 4kT \frac{B}{R_L}}$$

For $P = 100 \mu W$, $B = 300$ MHz and a bias resistance of 50Ω , the signal-to-noise ratio using a photodiode where η is typically 0.7, is

$$\frac{S}{N} = 1.4 \times 10^4$$

Using an avalanche photodiode with a typical gain of 100, the signal-to-noise ratio is

$$\frac{S}{N} = 0.7 \times 10^5$$

It follows that when the power coupled to the photodector is $100 \mu W$, the signal-to-noise ratio of the photodiode circuit is sufficiently high so that no avalanche photodiodes are required.

In a different approach to connect one of the n photodiodes in each column to the corresponding output line an integrated matrix switch of the type F100164 can be used, which can connect one of 16 terminals alternatively to 1 output terminal. However, for m output terminals m matrix switches are required. These m matrix switches would increase considerably the complexity and the power consumption of the switching system.

61.1.2 Opto-Electronic Switching Network with $N \times M$ Light Sources And M Photodetectors

The different design principle of the opto-electronic switching matrix is shown in Figure B-7. An array is formed of n light sources, each of them is modulated with one of the n information channels. The array is optically connected (by means of lenses or an optical fiber) to the photodetector 1 with its post-detection amplifier which leads to the output terminals 1. An identical array of n light sources is optically connected to the photodetector 2 with its post-detection amplifier with leads to the output terminal 2. This is repeated for all m detection circuits. The distribution of the n information channels to the $n \times m$ light sources presents a similar problems as outlined in Section A2-2. Therefore, this type of opto-electronic switching network does not seem to have any advantage over the electronic switching network, described in Section A2.2.

We conclude it is the opto-electronic switching network with the n light sources and the $n \times m$ photodetectors and post-detection amplifiers in Figure 12, which should greatly facilitate the distribution of the n input terminals to the switching network.

In summary, the opto-electronic switching system which requires for n input lines, m photodetectors, but $n \times m$ post detection amplifiers, is definitely more complex than the integrated switching system which requires only m photodetectors and m post detection amplifiers.

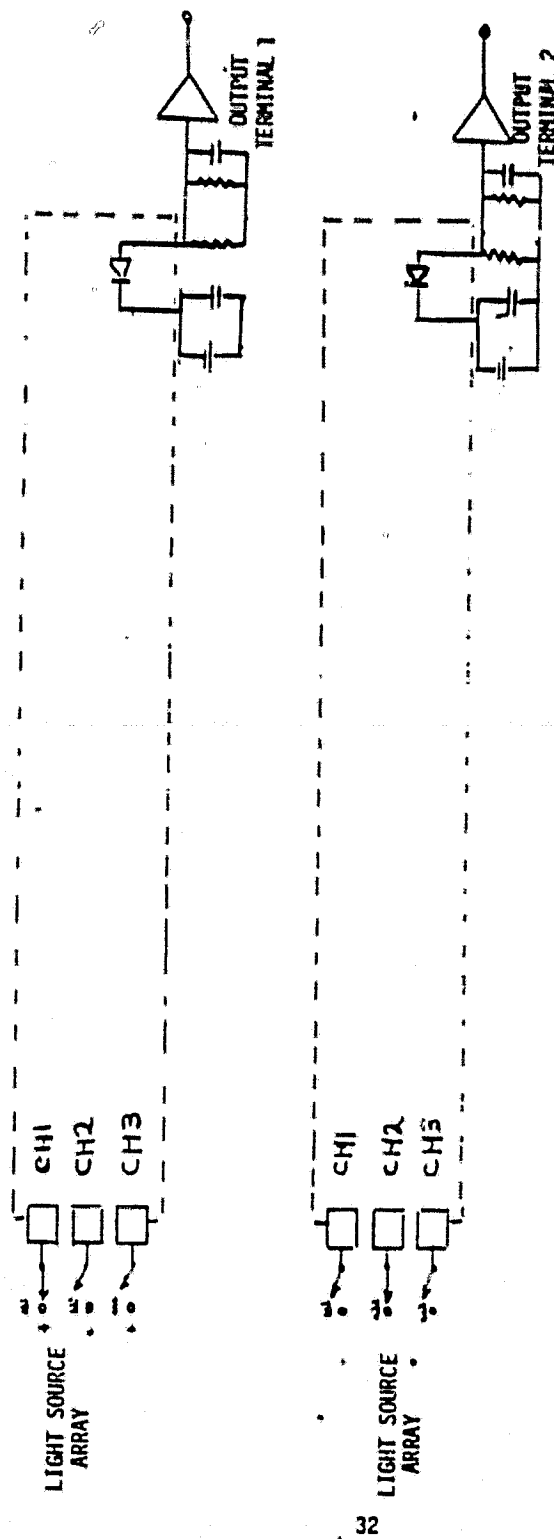
SECTION 2 ELECTRONIC SWITCHING

B1.2.1 Introduction

The electronic design approach to a 300 megabit digital matrix switch will require the most advanced state-of-the-art digital technology available: the 100K series Emitter Coupled Logic (ECL) produced by Fairchild which operates with rise and fall times of 0.7 nsec. and clock speeds up to 500 MHz. While 500 MHz operation can be obtained under ideal test conditions, practical considerations of component layout and stray input capacitance will reduce the overall system speed somewhat.

The new technology which permits the higher operating speeds of the 100 k series ECL devices is the Fairchild Isoplanar II transistor fabrication process. The new transistors have an area of only 1.2 mil² compared to the conventional Planar transistors which have an area of 4.8 mil². This allows for a corresponding reduction in parasitic junction capacitances which in turn gives a higher gain bandwidth product of over 5.0 GHz.

All devices in the 100 k ECL family are designed to be used with up to a 50 ohm transmission line. (Some devices can drive a 25 ohm line.) Due to the fast rise and fall times of these devices, any connection over 0.6" must be treated as a transmission line which will be shown later. Using standard multilayer PC board technology, a connection less than 0.6" seldom can be implemented; therefore, all lines in the system must be 50 ohm controlled impedance lines.



32

B-16a

Figure B-7. Schematic of Opto-Electronic Switching Network for $n \times m$ Light Sources and m Photodetectors

B 1.2.2 Circuit Configuration

The essential device for constructing the matrix switch will be the F100164 16 to 1 multiplexer. The device accepts up to 16 inputs and will select one of those inputs to be the output according to information presented to four control lines. Eight of these devices can be utilized to implement a 16 x 8 matrix switch which can be put on a 4 x 14 inch PC board. This is accomplished by driving the inputs of all the multiplexers in parallel. The select lines of each multiplexer are attached to a register which holds the proper switching information. In this way, any one of the 16 inputs may be switched into any of the 8 outputs. Figure B-8 shows a conceptual diagram of the switching arrangement.

Matrix switches with more than eight outputs can be easily built from the basic 16 x 8 building block by running the inputs to the boards in parallel. Figure B-9 shows how a 16 x 16 matrix switch can be built from two 16 x 8 switches.

The number of inputs to the switch can also be expanded by either a 2 to 1 multiplexer board or another 16 x 8 matrix switch. Figure B-10 shows how a 32 x 8 matrix switch can be built from three 16 x 8 building blocks. Half of the inputs are run to each switch which gives 16 outputs, but only half of the inputs are available on any given output. The 16 outputs are run into another 16 x 8 matrix switch which gives only 8 outputs, but now any of the 32 inputs can be switched to any of the 8 outputs. Another less complicated approach would be to utilize a 2 to 1 multiplexer card where each output needs only to choose between one output from either 16 x 8 switch board. This configuration is shown in Figure B-11

A 16 x 128 matrix switch can fit into a single tray approximately 20" x 18" x 6". The same tray can also hold a microprocessor for controlling the switch with memory, several I/O parts, a USART, and TTY or CRT interface circuitry. If there is need for a larger switch, more trays can easily be added.

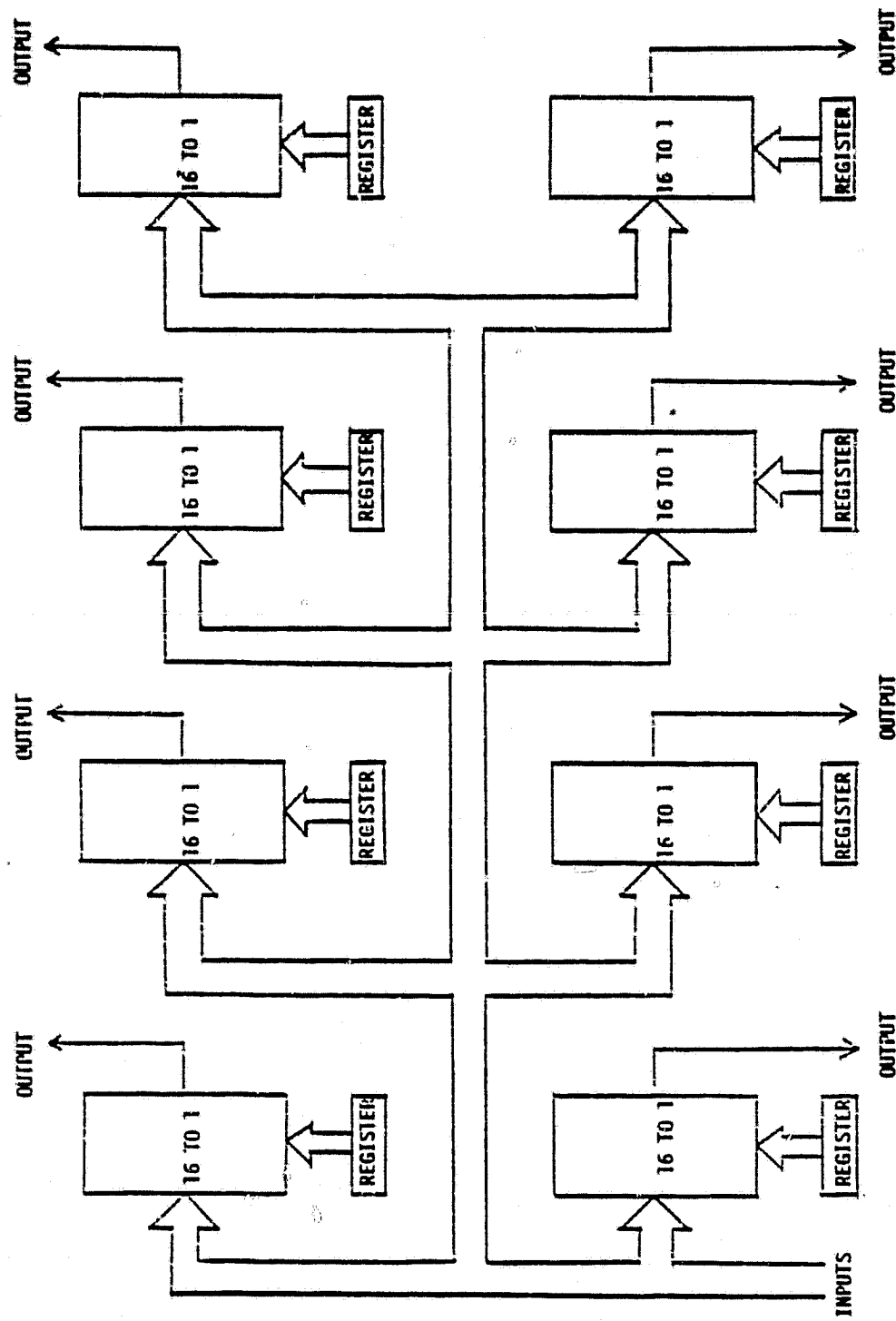


Figure B-8.. CONCEPTUAL DIAGRAM FOR 16×8 MATRIX SWITCH

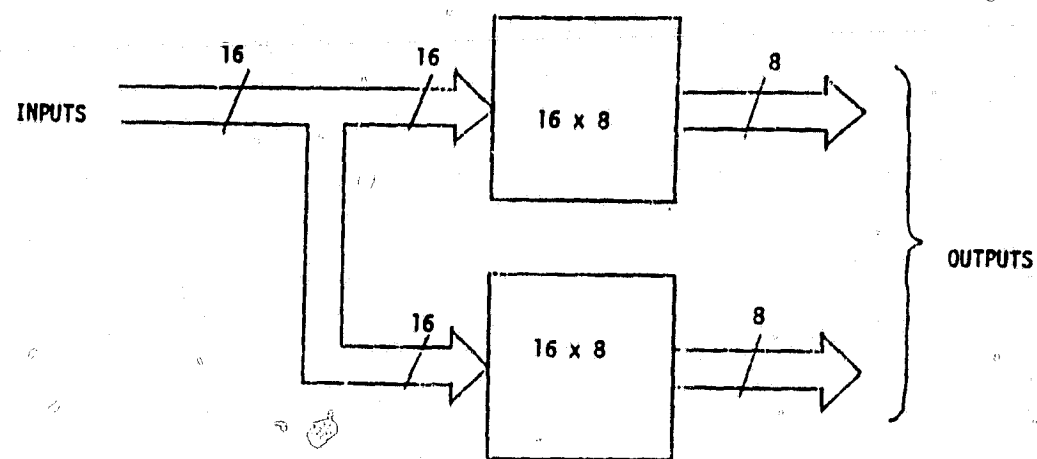


Figure B-9. 16 x 16 MATRIX SWITCH FROM TWO
16 x 8 MATRIX SWITCHES

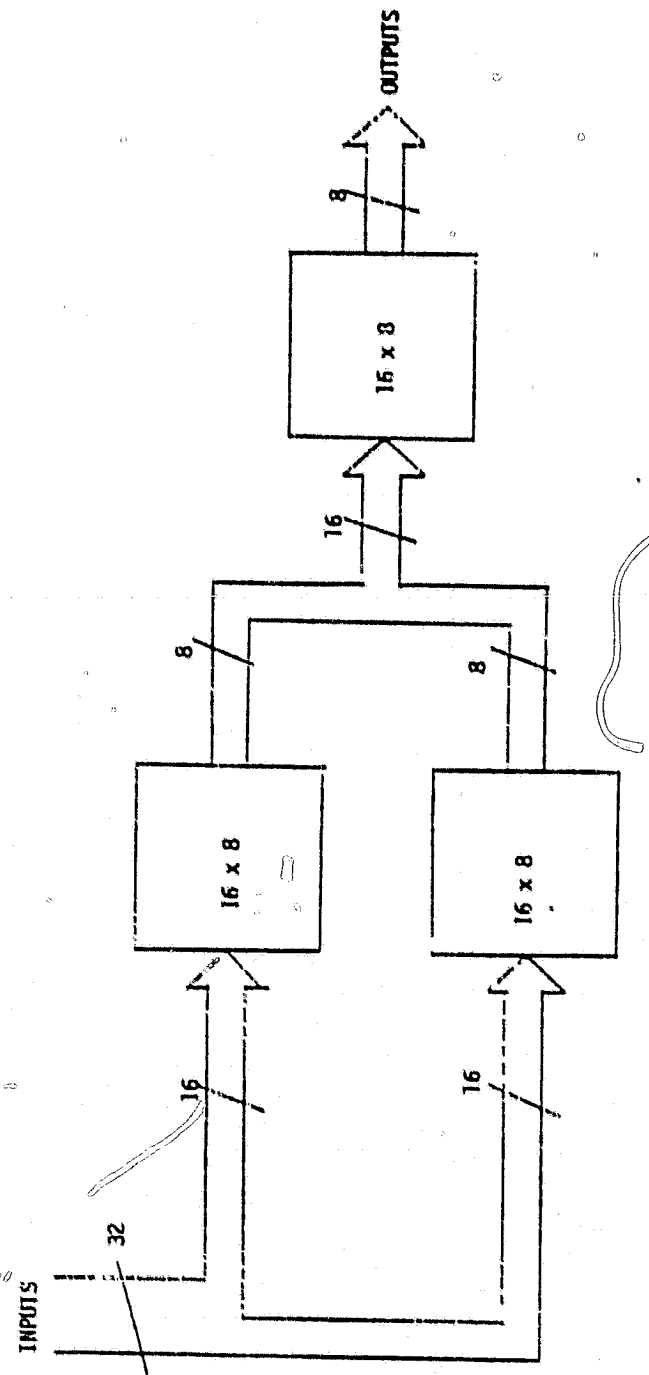


Figure B-10. 32 x 8 MATRIX SWITCH FROM THREE 16 x 8 MATRIX SWITCHES

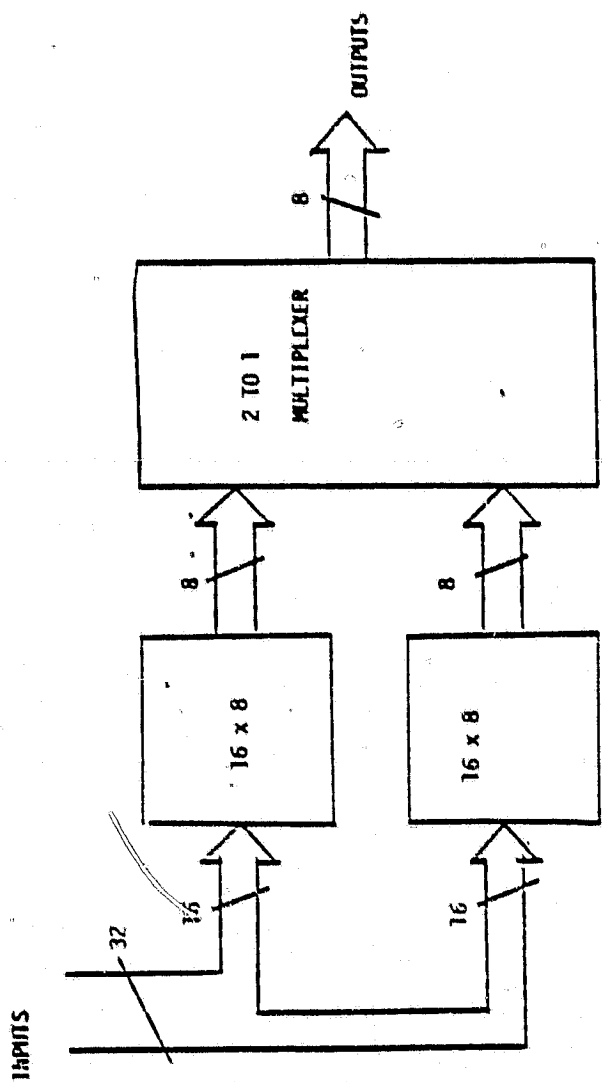


Figure B-11. 32 x 8 MATRIX SWITCH FROM TWO 16 x 8 MATRIX SWITCHES AND ONE 2 TO 1 MULTIPLEXER (EIGHT WIDE)

B1.2.3 Power Requirements

Each switch board requires:

-5.2 volts @ 2.74 Amps

-2.0 volts @ 4.6 Amps

A + 5 volt supply will probably be required for control circuitry. A 16 x 48 switch will require at least a 160 watt power supply for the switch PC boards alone. A 16 x 128 switch will require at least a 425 watt power supply.

B1.2.4 Transmission Line Considerations

The 300 M bit/sec. requirement presents some special problems in the transmission of data in the areas of device fanout, coupling of transmission lines, and reflections on transmission lines.

Since the devices used have 0.7 nsec. rise and fall times, all connections longer than 0.6" must be treated as transmission lines. A typical design parameter used in digital circuitry for determining whether a length of line need be treated as a transmission line is as follows: any connection with a length over $\frac{s_{r/f}}{4}$ electrical distance of rising and falling edge which ever is less) is a transmission line. For instance, on a 50Ω microstrip line, the speed of light is 3.2 times slower than in a vacuum due to the electric field partly being in a dielectric (fiberglass $\epsilon_r = 15$)

$$\frac{3 \times 10^8 \text{ m/sec.}}{3.2} = 9.375 \times 10^7 \text{ m/sec.} = \text{speed of light on micro-strip}$$

$$s_{r/f} = (.7 \times 10^{-9} \text{ sec.}) (9.375 \times 10^7 \text{ m/sec.}) = 6.6 \text{ cm}$$

$$\frac{s_{r/f}}{4} = 1.64 \text{ cm.} = .65"$$

Using strip transmission lines:

$$\text{Speed of light} = \frac{3 \times 10^8 \text{ m/sec.}}{\epsilon_r} = \frac{3 \times 10^8 \text{ m/sec.}}{15} = 7.75 \times 10^7 \text{ m/sec.}$$

$$s_{r/f} = (.7 \times 10^{-9} \text{ sec.}) (7.75 \times 10^7 \text{ m/sec.}) = 5.4 \text{ cm.}$$

$$\frac{s_{r/f}}{4} = 1.35 \text{ cm} = .5"$$

B.1.2.4.1 Reflections

All lines in the system will be 50Ω impedance lines. High speed communication between boards will be via 50Ω shielded, twisted pair. High speed data between two points on the same PC board will be via 50Ω shielded strip lines. Termination of these lines will be 50Ω (to -2.0 volts).

The nominal input impedance of the 100K devices is $50k \Omega$ with about 2 pf of parasitic capacitance (most of which is due to stray wiring capacitance). This is too large an impedance for an effective termination of the line. At the highest frequency of the signal, the capacitive reactance, which is by no means controllable, is approximately $-j160 \Omega$ (Calculation based on 500 MHz--highest frequency device can carry effectively). This input impedance can cause ringing along the transmission line because of the impedance of the devices which feed the transmission lines is less than 50Ω . A 50Ω terminating resistor is required to significantly reduce this ringing.

The 50Ω termination serves an additional purpose: the 100K series ECL requires a pull-down resistor on the output in similar manner to the more standard 10 k series ECL family. (The 50Ω resistor is tied to -2.0 volts instead of -5.2 volts as is standard practice to conserve power).

B.1.2.4.2 Fanout

The DC fanout capability of 100K series ECL is in the hundreds of gates due to low input power requirements. However, the stray capacitive reactance at high frequencies becomes very small using even a small number of gates. Using the 500 MHz frequency for calculation, three inputs represent only $-j150 \Omega$ impedance with 2 pf capacitance per gate. At this point, the $-j 50 \Omega$ input reactive impedance and the 50Ω terminating resistor in parallel can short out the higher frequencies of the Fourier spectrum of the pulse and slows the edge speed of the data slightly.

On each card it is necessary for 16 inputs to receive the same signal. Figure B-11 shows how this is accomplished without violating AC fanout rules. The signals are received on the board (one ECL load) and immediately drive two multiplexer chips. The signal continues and drives a buffer chip (F100122). This buffer chip can in turn drive two other multiplexers and another buffer and so forth down the board. Connections from the transmission line to the devices are very small compared to the wavelength of the signals to be used. So far, interconnections on a single board has been discussed.

The next consideration is how to drive many boards in a larger switch configuration such as 16 x 48. The problem is solved by an ECL gate with multiple outputs. The signals are received by a special receiver device (F100114) and sent to a device with four outputs. One output is used to drive the first two multiplexers and a buffer. Two other outputs are used to send the signal differentially to the next board. Thus, the signals are "daisy-chained" from board to board to allow simple and effective expandability of the switch. A schematic depicting one input line is provided in Figure B-12.

B.1.2.4.3 Coupling of Transmission Lines

Lower speed digital systems in the past have used microstrip transmission lines which are PC tracks of a specified width and height above a ground plane. Microstrip lines are rather susceptible to coupling since $50\ \Omega$ lines must be comparatively wide. However, spacing between lines must be small for dense circuitry.

Strip transmission lines would be an improvement over microstrip transmission lines in terms of decreased coupling. The difference between microstrip lines and strip lines is that strip lines have a ground plane above the PC track as well as below it. Microstrip lines have only one ground plane associated with them. Also, $50\ \Omega$ strip lines are not as wide as microstrip lines for the same distance from ground plane to signal line. This allows greater flexibility in PC layout.

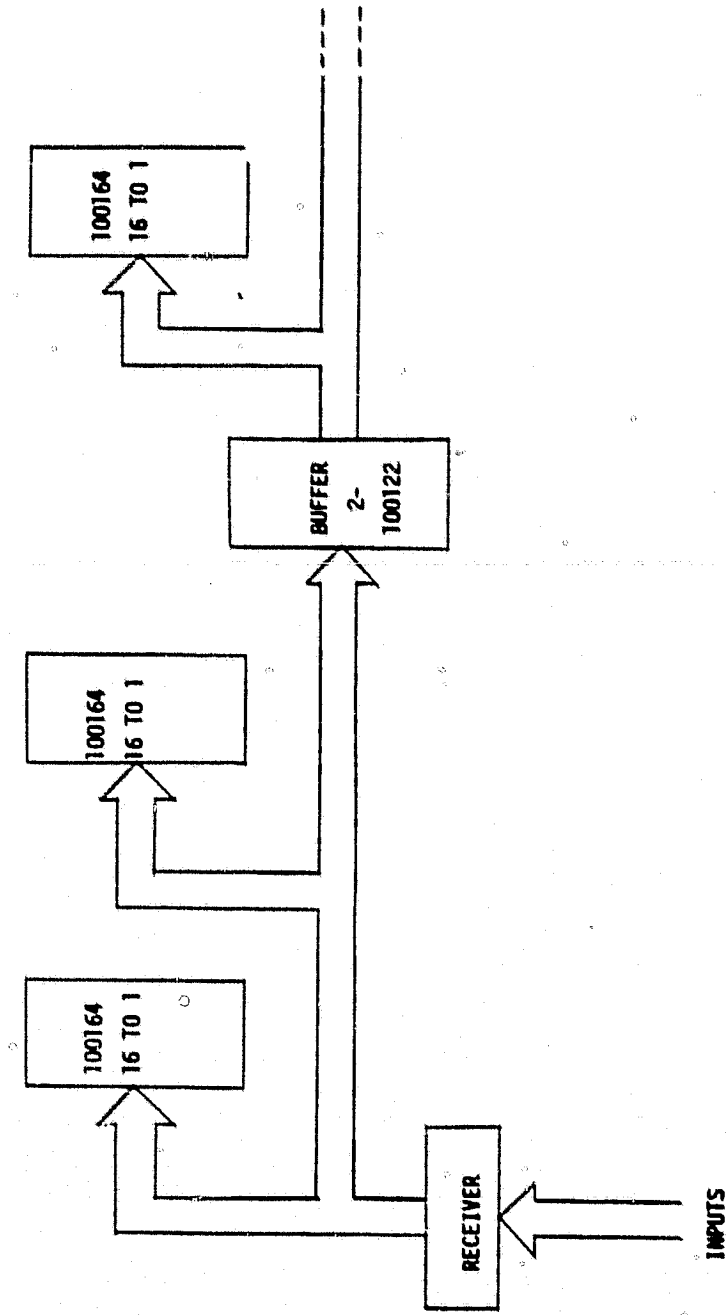


Figure B-11. SOLUTION TO AC FANOUT
PROBLEM ON BOARD

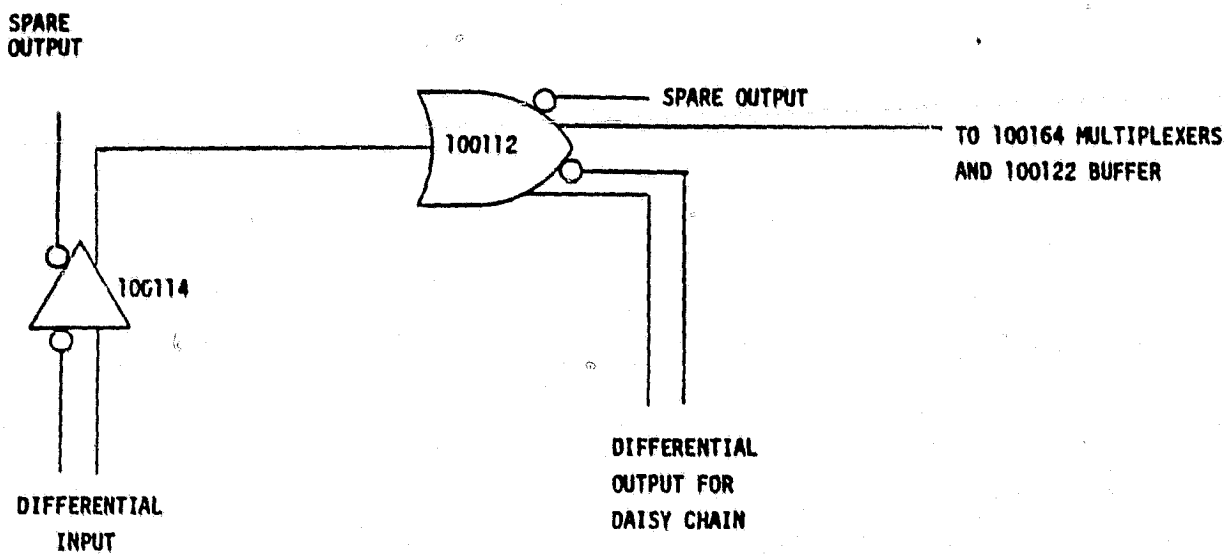


Figure B-12. SOLUTION TO AC FANOUT PROBLEM
FOR MANY BOARD INPUTS

In Figure B-13 a tentative layout of the multiplier F100164 together with the 16 transmission lines for the electric switching network is shown. The multiplier is placed on top of the 16 transmission lines. To ascertain that the connections from the input terminals of the multiplier to the transmission lines, are equal length, the center spacings between transmission lines must be made equal to the half-center spacings between input terminals (This requirement concurs with the position of the input terminals on both sides of the device).

The transmission lines are microstrip lines where the dielectric spacing b is equal of the thickness of the PC board, ($b = 10 \text{ mil} = 0.025 \text{ cm}$) and the dielectric constant is that of a standard fiber glass board, $\epsilon_r = 4.4$.

The characteristic impedance of the microstrip is

$$Z_0 = 10^4 \left(3\sqrt{\epsilon_r} \left\{ 7 + 8.83 \frac{w}{b} \right\} \right)^{-1}$$

For a pin spacing of 0.1 in. of the multiplier, the center spacing between transmission lines must be 0.05 in. = 0.127 cm. Then the spacing between the edges of the microstrips is $S = 0.057 \text{ cm}$.

Of major concern is the coupling between adjacent transmission lines. It is important to realize that the boundary conditions of parallel microstrips are such that coupling can occur through even and

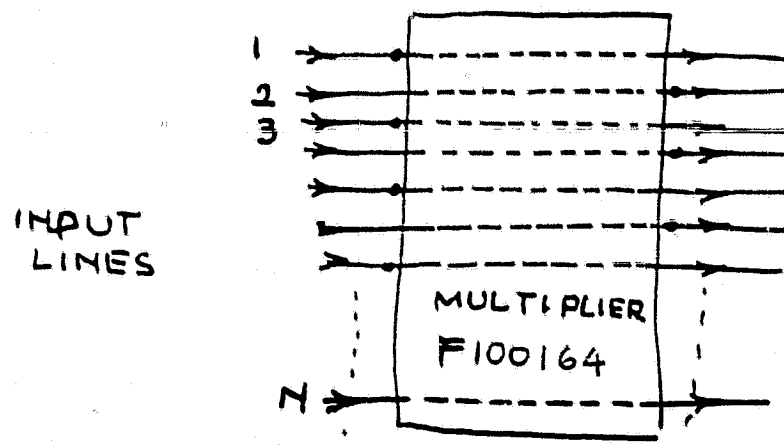


Figure B-13. Connections of Input Lines to Multiplier

odd modes. Because of the excitation of both modes coupling is contradirectional, as shown schematically in Figure B-14. The wave traveling from terminal 1 to terminal 4 will couple into terminal 2 but not into terminal 3. Coupling between the parallel microstrips is dependent on the interaction length l . The ratio of the voltages at terminals 2 and 1 is

$$\frac{v_2}{v_1} = \frac{jk \sin \theta}{\sqrt{1-k^2} \cos \theta + j \sin \theta} \quad (4-1)$$

where $\theta = \frac{2\pi}{\lambda \epsilon} l$ &

λ is the wavelength in the microstrip

$$k = \frac{Z_{oe} - Z_{oo}}{Z_{oe} + Z_{oo}} \quad (4-2)$$

and Z_{oe} and Z_{oo} are the characteristic impedances of the coupled microstrip lines for the even and the odd excitation, where

$$Z_0 = \sqrt{Z_{oe} Z_{oo}} \quad (4-3)$$

For $\epsilon_r = 4.4$, $\frac{w}{b} = 2.8$ and $\frac{s}{w} = 2.3$, $Z_{oe} = 53.5\Omega$ and $Z_{oo} = 46.5\Omega$.

Then,

$$k = 0.07.$$

The voltage ratio in Eq. 4-1 becomes largest for $l = (2n+1)\frac{\lambda \epsilon}{4}$, $n = 0, 1, 2, \dots$
Then the coupling between microstrip lines is

$$C = 20 \log \frac{1}{k} = 23 \text{ db.}$$

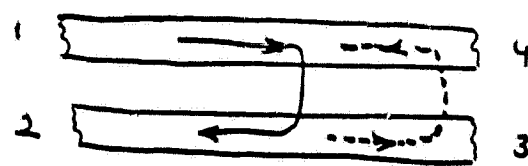


Figure B-14. Contradirectional Coupling

The coupling changes periodically from $C = 0$ for interaction lengths of $n\frac{\lambda_e}{2}$, to $C = 26$ db for $(2n+1)\frac{\lambda_e}{4}$ to the closest coupling of $C=23$ db for $(2n+1)\frac{\lambda_e}{4}$, where $n = 0, 1, 2$.

The wavelength λ_e of the microstrip with a dielectric where $\epsilon_r = 4.4$, is approximately $\lambda_e = \frac{\lambda_0}{1.9}$. At a frequency of 300 MHz $\frac{\lambda_e}{4} = 13$ cm and for the third harmonic in the Fourier spectrum of the pulses $\frac{\lambda_e}{4} = 4.33$ cm. These values should be taken into consideration in the layout of the switching network. Coupling between the microstrip transmission lines can be decreased when an upper ground plane is added. The upper ground plane reduces primarily the characteristic impedance of the even mode Z_{oe} and thus reduces the coupling factor in Eq. 4-2. It also follows from Eq: 4-3 that the upper ground plane reduces the characteristic impedance of the transmission lines Z_o . For the upper ground plane to significantly reduce the coupling, its spacing from the microstrip should be no more than 0.025 cm.

If this design approach can be implemented the characteristic impedance of the shielded microstrip lines could be further reduced by making the lines wider without exceeding the specifications for coupling between adjacent transmission lines.

B 1.2.5 Other Electronic Technologies

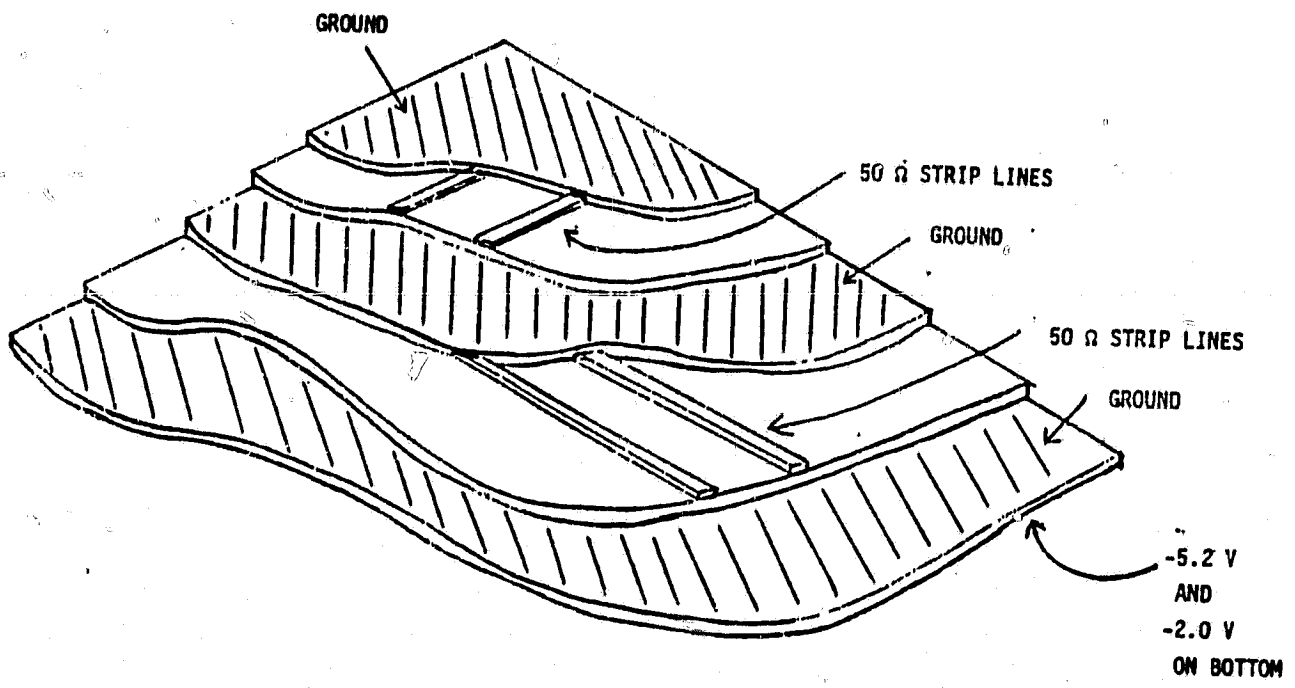
A possibility for construction of a matrix switch is using ceramic substrates. The silicon chips can be bonded directly to a ceramic board which has many layers of metalization. This helps to alleviate stray input capacitance of the devices, but it becomes more difficult to get $50\ \Omega$ lines close to the devices because the chips are small and require many connections to the relatively wide $50\ \Omega$ lines.

A combination of PC technology and ceramic technology would be the hybrid approach. A hybrid is a small piece of ceramic with two or three silicone chips bonded to it. The circuit is then mounted into a case similar to the packages used with standard IC products. The number of pins required for each hybrid makes this approach impractical. Each multiplexer requires 16 inputs, 1 output, 4 control lines, power and ground.

Small quantities of the two above mentioned technologies are very expensive compared to standard PC boards. Therefore, it is recommended that a six layer fiberglass PC board be used in the construction of the switch. There should be two layers of signals which will necessitate three layers of ground plane for strip transmission lines and one layer for voltage. Figure B-15 shows a typical cut away section for the PC board.

B 1.2.6 Summary

The matrix switch can be totally electronically implemented using the Fairchild 100 k series ECL family of digital logic. This logic family has a theoretical frequency limit of 500 MHz. Using a single 4" x 14" six layer PC board, a 16 x 8 matrix switch building block can be built with $50\ \Omega$ differential inputs and outputs. The number of inputs is easily expandable by simply adding more switch boards and "daisy-chaining" the inputs from one board to the next.



ORIGINAL PAGE IS
OF POOR QUALITY

Figure B-15 CUT AWAY OF PC BOARD

The number of inputs is also expandable, but a 2 to 1 multiplexer card is required to allow any input to be switched to any output. The number of 2 to 1 multiplexer cards required depends on the amount of input expansion desired. The cards will be mounted in a tray which is approximately 20" x 18" x 6". Each tray will hold enough cards to implement a 16 x 128 switch with room for control and interface circuitry.

2.7 LIST OF FEATURES

- Switch made from Fairchild 100K ultra high speed ECL
- 16 x 8 Matrix switch on one 14" x 4" PC board
- Outputs easily expandable in increments of 8
- Inputs expandable in increments of 16 by using either extra 16 x 8 Matrix switches or 2 to 1 multiplexer cards.
- Inputs are differential 100K ECL 50 Ω lines
- Interface to optical lines or other level electrical signals possible with added custom interface boards which can be mounted in same tray with switch boards.
- Microprocessor controllable ◦ Microprocessor with limited support hardware can be mounted in tray with switch. (Support includes USART, ROM, RAM, and I/O Ports. Others available on request)
- 16 x 128 switch will fit in one tray (18" x 20" x 6")
- Switch uses standard voltages: -5.2v, -2.0v, +5.0v (+5v is used only for microprocessor and/ or interface circuitry.)
- Outputs are differential 100K ECL which are designed to drive up to 1000 ft. of high quality twinax 50 Ω cable.
- Inputs represent only one 100K ECL load plus 50 Ω termination regardless of switch size.
- More than one tray of switches may be used for applications requiring very large switches.
- Forced air cooled trays for heat dissipation

The concept of an electronic switching network is described using multiplexers of the type 100164. Though the performance characteristics of the multiplexers would lend themself well for switching a 300 Mbit/sec data stream their reactive input impedance will limit their use in a large switching network. The reactive input impedance of parallel devices can reduce the rise and fall times of the data pulses considerably. However, buffer stages can be used in the switching network to mitigate the effect of the reactive input impedances.

The multiplexers together with the buffer stages form a rather complex switching system with large power consumption. The simplicity of the integrated switching matrix is outstanding in comparison to the electronic switching system.